HAW HAMBURG

Master‘s Thesis

Felix Ahlers

Investigation of Microchannel Cooling for Silicon Detectors for HEP and PS Applications

Fakultät Nachhaltige Ingenieurwissenschaften *Faculty of Sustainable Engineering*

Felix Ahlers

Investigation of Microchannel Cooling for Silicon Detectors for HEP and PS Applications

Masterarbeit eingereicht im Rahmen der Masterprüfung

im Studiengang Nachhaltige Energiesysteme im Maschinenbau
der Fakultät Nachhaltige Ingenieurwissenschaften
der Hochschule für Angewandte Wissenschaften Hamburg

in Zusammenarbeit mit:
Deutsches Elektronen-Synchrotron DESY
Abteilung ATLAS
Notkestraße 85
22607 Hamburg

Erstprüfer: Prof. Dr. Jan Piatek
Zweitprüfer: Dr. Sergio Díez Cornell

Abgabedatum: 02.04.2026

Zusammenfassung

Felix Ahlers

Thema der Masterthesis

Investigation of Microchannel Cooling for Silicon Detectors for HEP and PS Applications

Stichworte

Mikrokanalkühlung, Kühlung von Siliziumdetektoren, Wärmeübertragung, Strömungsmechanik, Mikrofluidik, CFD-Simulation, experimentelle Untersuchung

Kurzzusammenfassung

Ziel dieser Arbeit war es, die experimentelle Infrastruktur zur Untersuchung des strömungsmechanischen und thermischen Verhaltens von Mikrokanal-Kühlsystemen wieder in Betrieb zu nehmen sowie auszubauen. Auf dieser Grundlage wurde ein neuartiges Mikrokanaldesign charakterisiert.

Zusätzlich wurde ein kombinierter theoretischer und numerischer Ansatz entwickelt, um das beobachtete Strömungs- und Wärmeübertragungsverhalten zu interpretieren.

Die Ergebnisse zeigen, dass das Systemverhalten durch eine ungleichmäßige Verteilung der Kühlflüssigkeit geprägt ist, was sich wesentlich auf das thermische Verhalten auswirkt. Zudem konnte die Geometrie des Einlassverteilers als entscheidender Einflussfaktor auf Strömung und Wärmeübertragung identifiziert werden.

Insgesamt wurde ein kombinierter analytischer, numerischer und experimenteller Ansatz etabliert, der eine systematische Analyse sowie eine gezielte Optimierung von Mikrokanal-Kühlsystemen ermöglicht.

Felix Ahlers

Title of the paper

Investigation of Microchannel Cooling for Silicon Detectors for HEP and PS Applications

Keywords

microchannel cooling, silicon detector cooling, heat transfer, fluid dynamics, microfluidics, CFD simulation, experimental investigation

Abstract

The aim of this work was to recommission and expand the experimental infrastructure for investigating the fluid-dynamic and thermal behaviour of microchannel cooling systems. This infrastructure was subsequently used to characterise a novel microchannel design.

In addition, a combined theoretical and numerical approach was developed to interpret the observed fluid-dynamic and heat transfer behaviour.

The results show that the system behaviour is characterised by a non-uniform distribution of the coolant, which has a significant impact on the thermal characteristics. Furthermore, the geometry of the inlet manifold was identified as a key factor in flow and heat transfer.

Overall, a combined analytical, numerical and experimental approach has been established, enabling systematic analysis and targeted optimisation of microchannel cooling systems.

Contents

Symbols IV

Abbreviations VI

List of Figures VII

List of Tables X

1 Introduction 1

2 State of the Art 3

2.1 Design and Fabrication of the Microchannel Samples 3

2.1.1 Microchannel Layout 3

2.1.2 Fabrication Techniques 4

2.2 Experimental Setup 6

2.2.1 Test Equipment and Instrumentation 6

2.3 Experiments and Results of the Previous Study 7

2.3.1 Flow: Pressure Drop Measurements 8

2.3.2 Flow: Fluorescence Measurements 8

2.3.3 Thermal: Pt100 Temperature Measurements 10

2.3.4 Thermal: Infrared Temperature Measurements 11

2.3.5 Design Modifications 11

3 Fundamentals 14

3.1 Fundamentals of Fluid Dynamics 14

3.1.1 Continuity Equation (Conservation of Mass) 14

3.1.2 Flow Regimes, Vortex Formation and Reynolds Number 15

3.1.3 Boundary Layer in Internal Flow 16

3.1.4 Pressure Losses in Internal Flow 17

3.2 Fundamentals of Heat Transfer 19

3.2.1 First Law of Thermodynamics (Conservation of Energy) 19

3.2.2 Heat Conduction 20

3.2.3 Convective Heat Transfer 20

3.2.4 Heat Transfer in Internal Flow 21

4 Analytical Modelling of Flow and Heat Transfer **23**
4.1 Flow Model . . . 23
4.1.1 Model Assumptions and System Boundaries . . . 23
4.1.2 Flow Characteristics . . . 24
4.1.3 Pressure . . . 27
4.2 Thermal Model . . . 31
4.2.1 Model Assumptions and System Boundaries . . . 31
4.2.2 Analysis of Temperature Rise in a Microchannel . . . 32
4.2.3 Effect of Non-Uniform Inlet Temperature on Temperature Distribution . . . 35

5 CFD Simulation **37**
5.1 Flow Simulation . . . 37
5.1.1 Geometry . . . 37
5.1.2 Mesh Generation . . . 38
5.1.3 Numerical Setup . . . 41
5.1.4 Convergence and Solution Stability . . . 42
5.1.5 Simulation Results . . . 44
5.2 Thermal Simulation . . . 48
5.2.1 Extension of the Flow Model to Thermal Simulation . . . 48
5.2.2 Convergence and Solution Stability . . . 49
5.2.3 Simulation Results . . . 51

6 Experimentation **55**
6.1 Recommissioning of the Experimental Setup . . . 55
6.1.1 Measurement System Architecture . . . 55
6.1.2 NanoPort Bonding . . . 57
6.2 Flow: Pressure Drop Measurements . . . 59
6.3 Flow: Fluorescence Measurements . . . 61
6.3.1 Experimental Setup . . . 61
6.3.2 Results . . . 62
6.4 Thermal: Infrared Temperature Measurements . . . 67
6.4.1 Experimental Setup . . . 67
6.4.2 Results . . . 68
6.5 Thermal: Pt100 Temperature Measurements . . . 71
6.5.1 Experimental Setup . . . 71
6.5.2 Results . . . 72
6.6 Evaluation of Thermal Measurement Accuracy . . . 75
6.6.1 Reference Experiment for Temperature Measurement Accuracy . . . 76
6.6.2 Influence of Inlet Temperature Definition . . . 77

7 Conclusion **80**

Bibliography **82**

Appendix **87**

A Measurement System Scripts **88**

A.1 Arduino Script for Pressure Transducer Readout 88

A.2 Python Script for Flowmeter Readout 89

A.3 Python Script for Pt100 Sensor Readout 91

Symbols

Symbol	Description	Unit
α	convective heat transfer coefficient	$\mathrm{W/(m^2\,K)}$
ε	emissivity	-
λ	friction factor	-
μ	dynamic viscosity	$\mathrm{Pa\,s}$
ν	kinematic viscosity	$\mathrm{m^2/s}$
ρ	density	$\mathrm{kg/m^3}$
σ	Stefan-Boltzmann constant	$\mathrm{W/(m^2\,K^4)}$
τ_w	wall shear stress	$\mathrm{N/m^2}$
ζ	local pressure loss coefficient	-
A	cross-sectional area	$\mathrm{m^2}$
c_p	specific heat capacity	$\mathrm{J/(kg\,K)}$
D_h	hydraulic diameter	m
E	energy	J
h	specific enthalpy	J/kg
k	thermal conductivity	$\mathrm{W/(m\,K)}$
L	axial length	m
L_c	characteristic length	m
$L_\mathrm{e,h}$	hydrodynamic entrance length	m
$L_\mathrm{e,t}$	thermal entrance length	m
$\dot{m}$	total mass flow rate	kg/s
$\dot{m}_\mathrm{c}$	mass flow rate through an individual microchannel	kg/s
N	total number of microchannels	-
n	microchannel index	-
Nu	Nusselt number	-
P_w	wetted perimeter	m
Pr	Prandtl number	-
Δp	pressure drop	Pa
$\dot{q}''$	heat flux	$\mathrm{W/m^2}$
$\dot{Q}$	heat rate	W
Re	Reynolds number	-

Symbol	Description	Unit
R_{hyd}	hydraulic resistance	$\mathrm{Pa\,s/m^3}$
R_{th}	thermal resistance	K/W
T_{in}	fluid inlet temperature (measured at flowmeter and used as CFD boundary condition)	K
T_{m}	mass-weighted mean fluid temperature	K
$T_{\mathrm{m,i}}$	mass-weighted mean fluid temperature at the inlet of an individual microchannel	K
T_{s}	surface temperature (microchannel wall or wafer surface, depending on context)	K
u	mean flow velocity	m/s
u_τ	friction velocity	m/s
$\dot{V}$	total volumetric flow rate	$\mathrm{m^3/s}$
$\dot{V}_{\mathrm{mc}}$	volumetric flow rate through an individual microchannel	$\mathrm{m^3/s}$
x	axial coordinate along an individual microchannel	m
y^+	dimensionless wall distance	-

Abbreviations

Abbreviation	Definition
ADC	Analog-Digital-Converter
CFD	Computational Fluid Dynamics
DESY	Deutsches Elektronen-Synchrotron
DRIE	Deep-Reactive-Ion-Etching
FCC	Future Circular Collider
HEP	High Energy Physics
IMB-CNM	Institute of Microelectronics of Barcelona – Centro Nacional de Microelectrónica
IR	Infrared
LHC	Large Hadron Collider
PCB	Printed circuit board
PEEK	Polyether ether ketone
PS	Photon Science

List of Figures

Figure 1 Initial microchannel layout including outer dimensions (in mm) and labeled regions 4
Figure 2 Steps in the production process of silicon wafers with embedded microchannels 5
Figure 3 Schematic representation of the experimental setup 6
Figure 4 NanoPort Assembly including coned NanoPort, gasket and fitting . . . 7
Figure 5 Pressure drop measurements for four different microchannel samples . 8
Figure 6 Fluorescence measurements compared to CFD simulation for $\dot{V} = 2\,\mathrm{mL/min}$ and $\dot{V} = 3\,\mathrm{mL/min}$ 9
Figure 7 Fluorescence measurements compared to CFD simulation for $\dot{V} = 20\,\mathrm{mL/min}$ 9
Figure 8 Arrangement of the Pt100 sensors on the wafer surface 10
Figure 9 Measurements using Pt100 sensors on the wafer surface for different volumetric flow rates 10
Figure 10 CFD simulations compared to infrared temperature measurements . . 11
Figure 11 Application scheme of an interposer with microchannels. 12
Figure 12 Calculated manifold width as a function of the microchannel index n . 12
Figure 13 Current microchannel layout with outer dimensions and geometric constraints for the application as interposer 13

Figure 14 Streamtube representation illustrating the continuity equation for steady flow 15
Figure 15 Schematic of boundary layer separation with associated pressure profile 16
Figure 16 Development of the hydrodynamic boundary layer in a duct 17
Figure 17 Hydraulic resistances for straight channels with different cross-sectional shapes 18
Figure 18 Fluid domain for a side-branching junction 18
Figure 19 Schematic representation of the energy balance for an open system . . 19
Figure 20 One-dimensional heat conduction through a plane wall 21
Figure 21 Thermal boundary layer development in a duct 22

Figure 22 Control volume of manifold segment 2 with mass balance 24
Figure 23 Calculated flow velocity along the inlet manifold 26
Figure 24 Hydraulic resistance network of the first five microchannels 28

Figure 25 Pressure drop as a function of volumetric flow rate for water and Novec7100, calculated using the hydraulic resistance model 29
Figure 26 Calculation scheme for the determination of local pressure losses at a side-branch junction 29
Figure 27 Local pressure drop at each microchannel entry induced by the branch 30
Figure 28 Schematic of the simplified system for analytical modelling 32
Figure 29 Colour map of the wall temperature T_s along the microchannels and its fluid inlet temperature $T_{\mathrm{m,i}}$ for theoretical conditions 36

Figure 30 Subdivided CFD fluid domain at the inlet manifold showing the first five microchannels 38
Figure 31 Generated mesh of the microchannels and the microchannel entries . . 40
Figure 32 Generated mesh at the inlet and along the inlet manifold 40
Figure 33 Convergence history of residuals for water 43
Figure 34 Convergence of the pressure drop for water 43
Figure 35 CFD results of the pressure drop as a function of volumetric flow rate for different meshes (water) 45
Figure 36 Pressure drop as a function of the volumetric flow rate for water and Novec7100, comparing analytical calculations and CFD results 45
Figure 37 Influence of the mesh resolution on the streamlines at selected microchannel entries 46
Figure 38 Distribution of volumetric flow through single microchannels 47
Figure 39 Exploded view of the domains used for the thermal simulation 48
Figure 40 Convergence history of residuals for the thermal simulation 50
Figure 41 Convergence of the fluid outlet temperature for the thermal simulation 50
Figure 42 Comparison of inlet conditions for Novec7100 52
Figure 43 Comparison of the wall temperature T_{s} predicted by the analytical model and obtained from the CFD simulation at $\dot{V} = 10\,\mathrm{mL/min}$ . . . 53
Figure 44 Comparison of the wall temperature T_{s} predicted by the analytical model and obtained from the CFD simulation at $\dot{V} = 30\,\mathrm{mL/min}$ . . . 53
Figure 45 Contour plots for fluid velocity and temperature in the manifold, local flow effects in the manifold marked in red 54

Figure 46 Experimental measurement system architecture 56
Figure 47 Bonding tool shown as CAD design and actual assembly 58
Figure 48 Detached NanoPort with *Loctite Glas Glue* at the wafer surface 58
Figure 49 Detached NanoPort with 2-component epoxy adhesive at the NanoPort 59
Figure 50 Comparison of experimentally measured and simulated pressure drop . 60
Figure 51 Test setup for the fluorescence measurements in the nanofluidics laboratory 61
Figure 52 Comparison of fluorescence measurements and CFD results at selected microchannel entries for $\dot{V} = 2\,\mathrm{mL/min}$ 63

Figure 53 Comparison of fluorescence measurements and CFD results at selected microchannel entries for $\dot{V} = 3\,\mathrm{mL/min}$ 63
Figure 54 Comparison of fluorescence measurements and CFD results at selected microchannel entries for $\dot{V} = 5\,\mathrm{mL/min}$ 64
Figure 55 Comparison of fluorescence measurements and CFD results at selected microchannel entries for $\dot{V} = 6\,\mathrm{mL/min}$ 64
Figure 56 Comparison of fluorescence measurements and CFD results at selected microchannel entries for $\dot{V} = 10\,\mathrm{mL/min}$ 65
Figure 57 Comparison of fluorescence measurements and CFD results at selected microchannel entries for $\dot{V} = 15\,\mathrm{mL/min}$ 65
Figure 58 Comparison of fluorescence measurements and CFD results at selected microchannel entries for $\dot{V} = 20\,\mathrm{mL/min}$ 66
Figure 59 Comparison of fluorescence measurements and CFD results at other significant regions 67
Figure 60 Experimental setup for IR measurements with the camera positioned above the wafer 68
Figure 61 Comparison of temperature contours from CFD simulation and IR measurements at $\dot{V} = 10\,\mathrm{mL/min}$ 69
Figure 62 Comparison of temperature contours from CFD simulation and IR measurements at $\dot{V} = 20\,\mathrm{mL/min}$ 70
Figure 63 Comparison of temperature contours from CFD simulation and IR measurements at $\dot{V} = 30\,\mathrm{mL/min}$ 70
Figure 64 Positioning of the Pt100 sensors on the wafer surface 71
Figure 65 Measured temperature as a function of time, used to determine the thermal steady-state. 72
Figure 66 Comparison of measured and simulated temperature at sensor locations for $\dot{V} = 10\,\mathrm{mL/min}$ 73
Figure 67 Comparison of measured and simulated temperature at sensor locations for $\dot{V} = 20\,\mathrm{mL/min}$ 74
Figure 68 Comparison of measured and simulated temperature at sensor locations for $\dot{V} = 30\,\mathrm{mL/min}$ 74
Figure 69 Measured temperature at sensor locations for different volumetric flow rates 75
Figure 70 Schematic representation of the factors influencing the undisturbed surface temperature and the surface temperature disturbed by a contact temperature probe or a permanently mounted, flat temperature sensor 76
Figure 71 Reference measurement comparing Pt100 sensor, contact thermometer and IR camera during warm-up of a cooled aluminium plate 77

Figure 72 Overview of the methodology, key findings and future work 81

List of Tables

Table 1 Reynolds numbers in the microchannels for water and Novec7100 at different volumetric flow rates 26

Table 2 Mesh quality metrics 39
Table 3 y^+ in the microchannels for water and Novec7100 at different volumetric flow rates 41
Table 4 Overview of the investigated meshes 44
Table 5 Thermal boundary conditions used in the simulations 49
Table 6 Thermophysical properties of the solid materials used in the simulations 49

1 Introduction

Silicon detectors are widely used in physics experiments to measure the trajectories and properties of particles. The associated readout electronics required for signal processing dissipate heat, which can negatively affect detector performance and signal quality. Efficient thermal management is therefore essential to ensure stable and reliable operation. Microchannel cooling has emerged as a promising approach, as it enables highly efficient heat removal while maintaining a low material budget, which is a key requirement in High Energy Physics (HEP) applications. Its high cooling efficiency further allows for effective control of radiation-induced leakage currents, which increase with temperature and degrade detector performance. For Photon Science (PS) detectors, the direct integration of microchannels in the silicon substrate is of particular interest, as it enables localized cooling without introducing additional material interfaces [23]. Moreover, microchannel cooling concepts are also investigated in other fields such as the cooling of AI chips or fuel cells [14, 51]. In all applications, efficient thermal management is not only essential for reliable operation but is also important in improving energy efficiency and reducing the overall environmental impact of high-performance electronic systems [47].

The increasing performance requirements of modern particle physics experiments further intensify these thermal challenges. Upgrades such as the High-Luminosity Large Hadron Collider (LHC) at CERN, as well as future accelerator concepts like the Future Circular Collider (FCC), aim for significantly higher collision rates and energies [15, 16]. These projects highlight the need for further development of detector technologies and supporting infrastructure, including efficient cooling concepts.

These challenges have led to specialized research efforts focusing on the development of advanced cooling concepts for future detector systems. The DRD8 collaboration, an international research initiative within the CERN framework involving multiple institutes, focuses on the research and development of innovative mechanical structures and cooling strategies for future detectors. Within this collaboration, Work Package 3.2 specifically investigates microchannel cooling concepts [24]. The work presented here is conducted within this research framework at Deutsches Elektronen-Synchrotron (DESY) and contributes to their ongoing development.

Against this background, the aim of this work is to restore the capability to experimentally characterise the fluid-dynamic and thermal behaviour of microchannel prototypes by recommissioning and extending an existing test setup. In parallel, theoretical models

and numerical simulations are employed to analyse fluid-dynamic and heat transfer mechanisms and provide guidance for the design, procedure and evaluation of experimental investigations. In this way, the work aims to establish a combined theoretical, numerical and experimental framework to characterise a previously uncharacterised microchannel layout and to analyse the coupling between fluid dynamics and heat transfer. The resulting insights and infrastructure provide a foundation for future design adaptation and optimisation of microchannel cooling concepts for detector applications.

The structure of this thesis is as follows. Chapter 2 reviews previous work on microchannel cooling conducted at DESY, which forms the foundation of the present study. In chapter 3 the relevant fluid dynamics and heat transfer concepts are introduced which are subsequently applied in chapter 4 to develop analytical models for the description of the flow and heat transfer behaviour. Chapter 5 presents the Computational Fluid Dynamics (CFD) simulation approach implemented in Ansys Fluent, including the model setup. Chapter 6 describes the recommissioning of the experimental setup, the obtained results, and an evaluation of the measurement accuracy. Finally, chapter 7 summarises the main findings and provides an outlook on future work.

2 State of the Art

This chapter presents the current status of silicon microchannel cooling development at DESY and thereby defines the technical and experimental foundation from which this work proceeds. It summarises the established design principles, fabrication processes, experimental infrastructure, and key findings of the preceding investigations. These elements form the basis for the analytical, numerical, and experimental studies carried out in this thesis.

2.1 Design and Fabrication of the Microchannel Samples

A first microchannel cooling sample, including its design concept, was presented in the work of Flaschel [23]. For the development of microchannel cooling, DESY is collaborating with the Institute of Microelectronics of Barcelona – Centro Nacional de Microelectrónica (IMB-CNM). IMB-CNM possesses the facilities required to etch microchannels into silicon wafers and seal them with another wafer. Moreover, IMB-CNM is able to verify the quality of the fabrication process. Consequently, the tested samples in this work were produced by IMB-CNM. The following subsections provide more detailed information about the tested microchannel samples, their design and the fabrication process.

2.1.1 Microchannel Layout

The design of the layout of the microchannels is governed by the requirement to keep the temperature gradient as small as possible. Therefore, an equal distribution of the coolant is important, which can be achieved by holding constant pressure in the manifolds. The volumetric flow in the inlet manifold decreases in the direction of the flow due to the coolant flowing into the microchannels. To prevent the resulting influence on the pressure, the manifold tapers. The equation

$$w_m(n) = \frac{h\sqrt[4]{\frac{w_c^4 h^4 (N-n+1)}{(w_c+h)^4 N}}}{-h+\sqrt[4]{\frac{w_c^4 h^4 (N-n+1)}{(w_c+h)^4 N}}}, \tag{1}$$

determines the width of the manifold w_m at microchannel n with the constant height h, the initial manifold width $w_c = 1000\,\mu m$ and the total number of microchannels N, so that the pressure is constant. The first design layout was designed to fit on a 4 inch silicon wafer. It has 60 microchannels with a length of 51.6 mm. The channel width and height were chosen to be 100 µm to maintain the mechanical stability of the sample. The layout is tilted by 15° and the entries and exits of the channels are widened to increase the entry angle of the fluid to prevent flow separation [23]. The resulting layout on the wafer is shown in figure 1. The shown terminology is used consistently throughout this work.

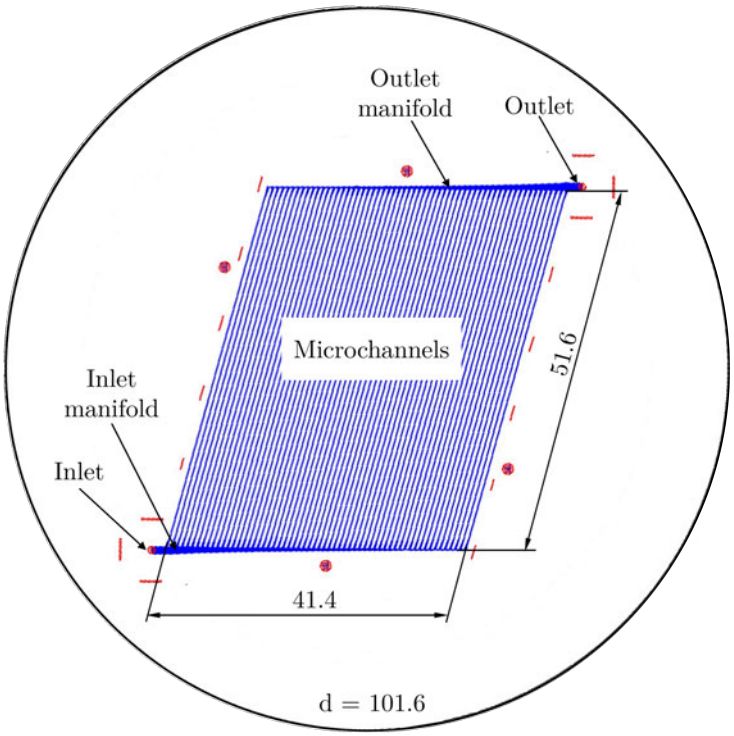


Figure 1: Initial microchannel layout including outer dimensions (in mm) and labeled regions (based on [23]).

2.1.2 Fabrication Techniques

The microchannel samples used in this work were fabricated by etching microchannels into a silicon wafer using a manufacturing process called Deep-Reactive-Ion-Etching (DRIE). The manufacturing steps are shown in figure 2 and will be further explained. Microchannels are etched into silicon wafers which are 300 µm or 500 µm thick (a). In a photolithographic process a photoresistant layer is applied to the surface of the wafer (b) and developed by light to define where the silicon needs to be etched to achieve the predefined layout of microchannels (c). Now, DRIE is used to etch the microchannels into the silicon wafer (d). The microchannels in this work have a depth and width of 100 µm. With DRIE it is possible to etch the silicon very anisotropically in the vertical direction to obtain precise rectangular microchannels. After the DRIE process, the

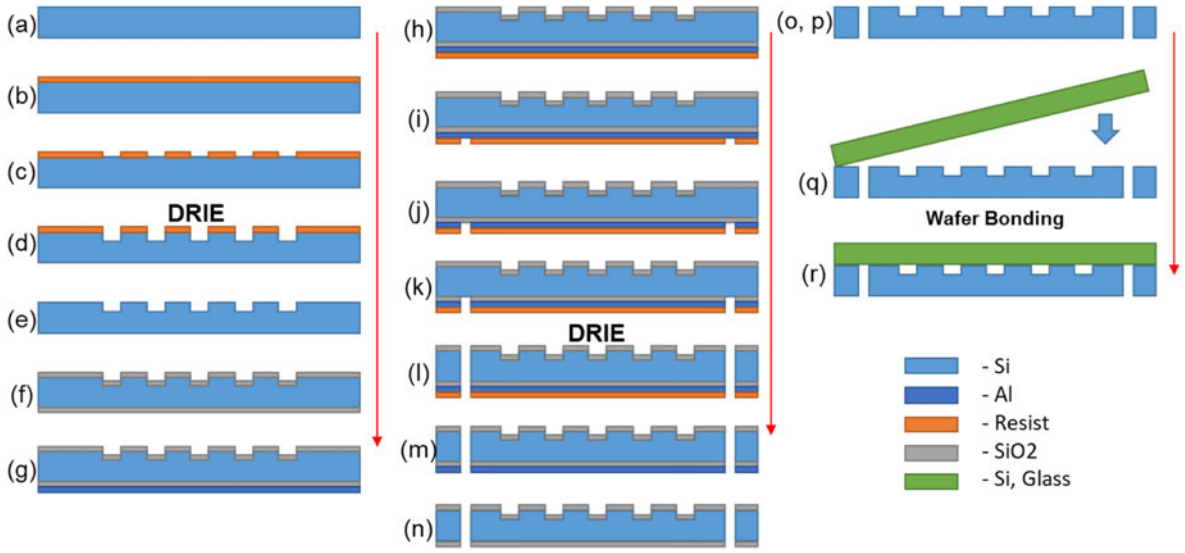


Figure 2: Steps in the production process of silicon wafers with embedded microchannels [46].

photoresistant layer can be removed (e). Next, the inlet and outlet are manufactured. Therefore, both sides of the wafer are coated with a layer of silicon dioxide (SiO_2) for protection (f). On the backside (opposite side of the microchannels) of the wafer an aluminium layer is sputtered on top of the SiO_2 layer (g). This layer is used to protect the silicon of the wafer during the longer DRIE process for manufacturing the inlet and outlet. Again, a photoresistant is applied (h) and processed to achieve a layout for the areas that need to be etched (i). In the next step, first the aluminium layer is wet etched (j), followed by dry etching the SiO_2 layer (k). Finally, the through holes can be manufactured by using DRIE (l). In the following steps the before applied layers are removed by different processes (m, n, o). Eventually, a RCA-cleaning removes any remaining residues and particles (p). The manufacturing of the microchannels is at this point completed.

Next, to seal the microchannels, a second wafer of glass or silicon is bonded to the wafer containing embedded structures. Therefore, different bonding techniques can be used depending on the material combination. Anodic Bonding is used for Silicon and Glass. Eutectic Bonding is used for Silicon and Silicon with an intermediate Silicon/Gold Layer. Fusion or Direct Bonding is used for a direct connection between Silicon and Silicon. For the bonding process, the two wafers are placed into a bonding chamber, where the required conditions such as vacuum and a high temperature are established. Depending on the bonding technique, additional conditions like an applied voltage (anodic bonding) or the presence of an intermediate metal layer (eutectic bonding) may be used. Under these conditions, atomic interactions (electrostatic attraction, alloy formation or diffusion) at the wafer interfaces occur, leading to a permanent fusion of the materials. The final bonded assembly with embedded microchannels is the result (r) [46].

2.2 Experimental Setup

The experimental setup used in this work was introduced in the dissertation "Microchannel Cooling for Silicon Detectors" [23]. The setup enables the integration of microchannel cooling samples into a closed coolant circuit. The pump, which is also integrated into the cooling circuit, allows the volumetric flow rate to be adjusted to different values. Using various measurement devices, such as pressure transducers, a flowmeter and Pt100 sensors, it is possible to determine the fluid-dynamic and thermal characteristics of samples with embedded microchannels. The schematic representation of the experimental setup is shown in figure 3.

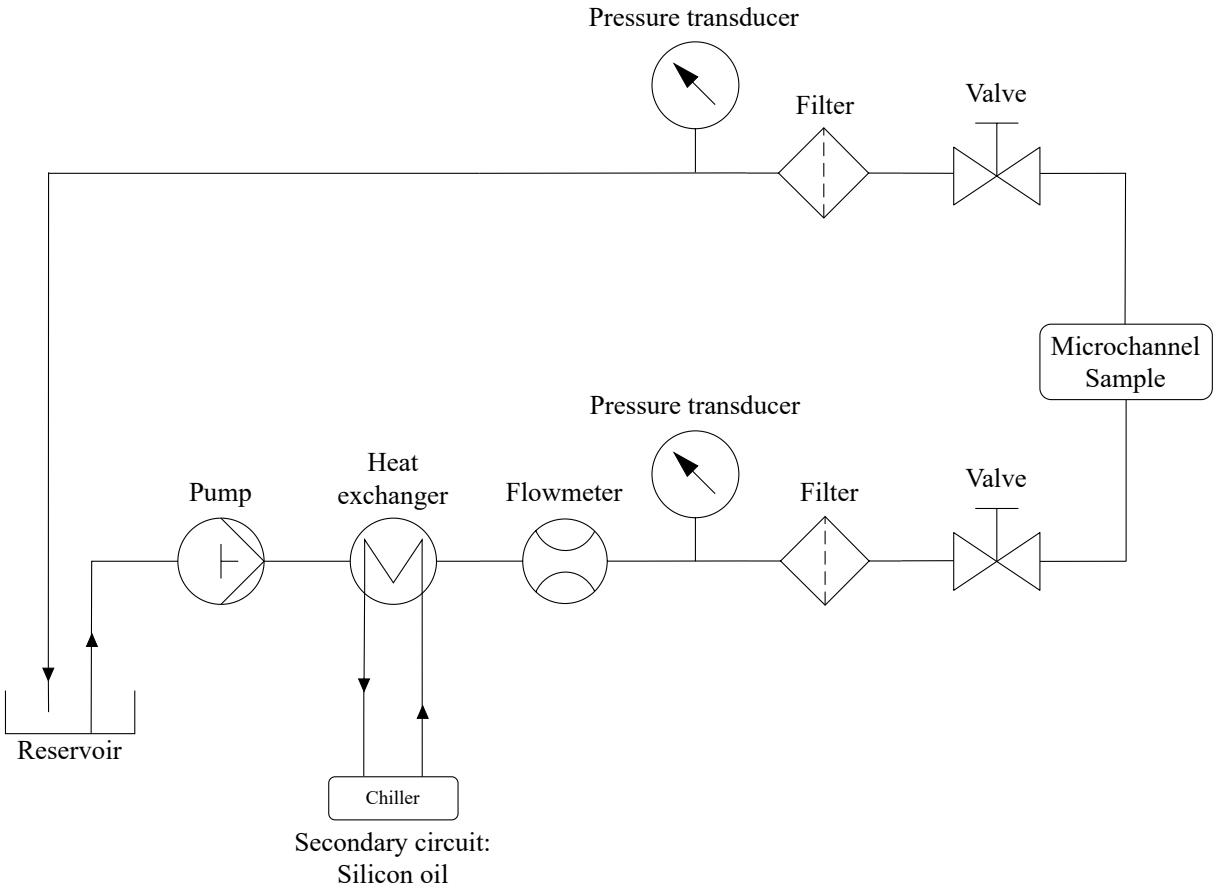


Figure 3: Schematic representation of the experimental setup.

2.2.1 Test Equipment and Instrumentation

The used pump model is ECOM IOTA 300 [19]. It has a volumetric flow rate range from 1 mL/min to 300 mL/min which can be set in 1 mL steps. The pressure adjusts itself automatically to achieve the prescribed volumetric flow rate. Moreover, the pump is equipped with a pressure sensor, which allows to monitor the pressure at the pump in operation. From the pump the coolant is pumped through a heat exchanger. The model is EWT-BE4-10 that is a stainless steel heat exchanger with 10 plates [20]. A

chiller (Huber CC-505) circulates cooled silicon oil through the heat exchanger, thereby reducing the temperature of the coolant passing through the sample. The temperature range of the chiller goes from −50 °C to 200 °C. The next device integrated in the coolant circuit is the Bronkhorst mini Cori Flow M14. The flowmeter is capable of tracking the temperature, density and volumetric flow rate of the coolant [11]. To monitor the pressure drop through the microchannel cooling sample two Swagelok S-Model pressure transducers (PTI-S-AG100-22A0) are installed in the setup. One transducer is positioned upstream and the other downstream of the sample [39]. Furthermore, two Swagelok TF filters with a nominal pore size of 15 µm are integrated into the coolant circuit to avoid contamination of the microchannels by small particles [38]. In addition, two Swagelok SS-1VS6MM valves are incorporated to isolate the coolant during the integration of the microchannel sample to prevent any coolant leakage [40]. The connection between the aforementioned devices is made using stainless steel pipes with a diameter of 1/8 inch and all required tube fittings and adapters by Swagelok. To monitor the surface temperature of the samples at different points several Pt100 sensors are used [23].

For the connection between the samples and the coolant circuit NanoPort Assemblies (figure 4) are used. These are designed for the chip-based analysis and also for the usage in combination with silicon. The assemblies consist out of a fitting, which is connected to the coolant circuit and can be screwed into the coned NanoPort, which is bonded to the wafer surface. The connection between tube and fitting is sealed with a ferrule. The gasket is used to avoid a contamination of the fluid path with glue. NanoPorts are made out of Polyether ether ketone (PEEK) [27].

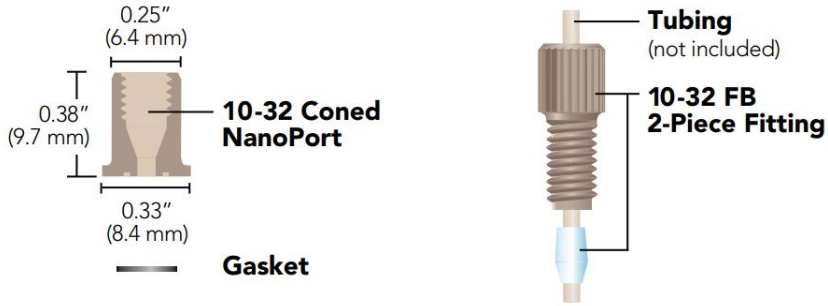


Figure 4: NanoPort Assembly including coned NanoPort, gasket and fitting [27].

2.3 Experiments and Results of the Previous Study

This section summarises the experimental methods and results of the preceding dissertation. It provides an overview of the used measurement techniques and presents the corresponding results, which define the experimental reference state for comparison with the investigations carried out in this thesis.

2.3.1 Flow: Pressure Drop Measurements

For the determination of the pressure drop the pressure was measured upstream and downstream of four samples with the same layout but fabricated using different bonding procedures. The results are shown in figure 5. The volumetric flow rate was varied from 6 mL/min to 40 mL/min. Three prototypes (A, B and C) exhibit nearly identical behaviour up to a flow rate of $\dot{V} = 30\,\mathrm{mL/min}$. At higher flow rates, slight variations become visible. Prototype D shows a more significant deviation over the investigated flow range. This behaviour was attributed to issues in the fabrication procedure [23].

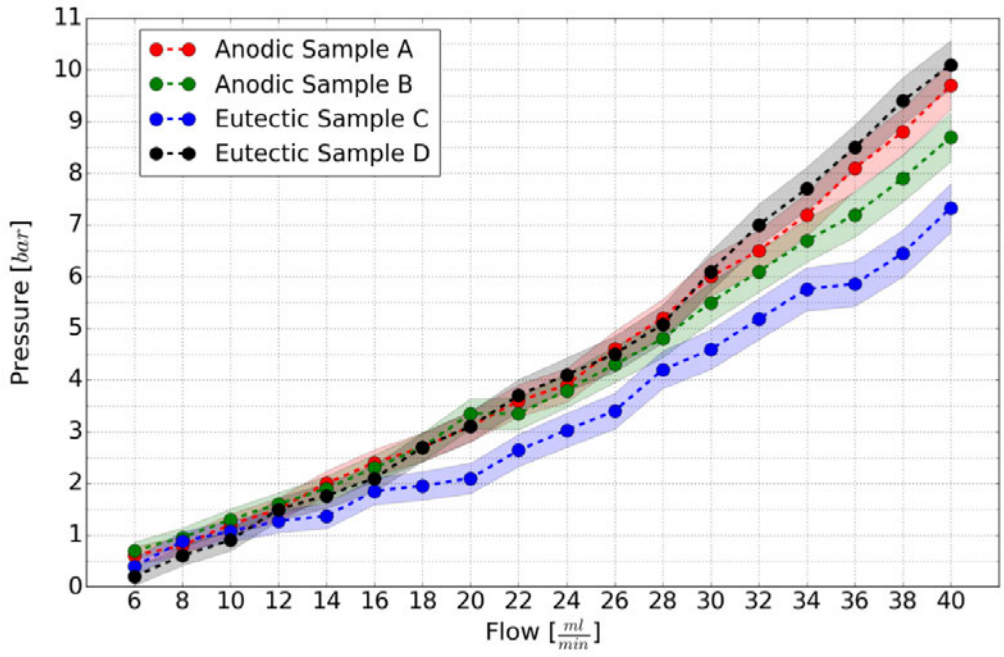
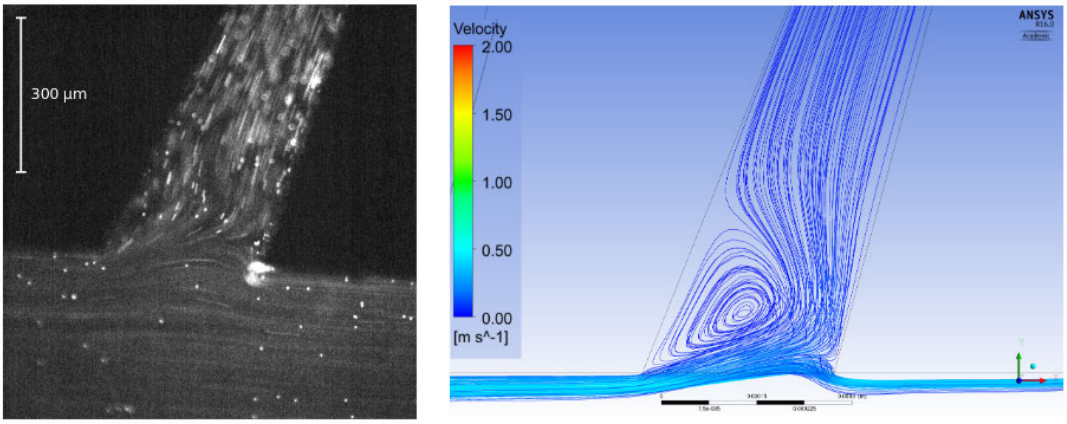


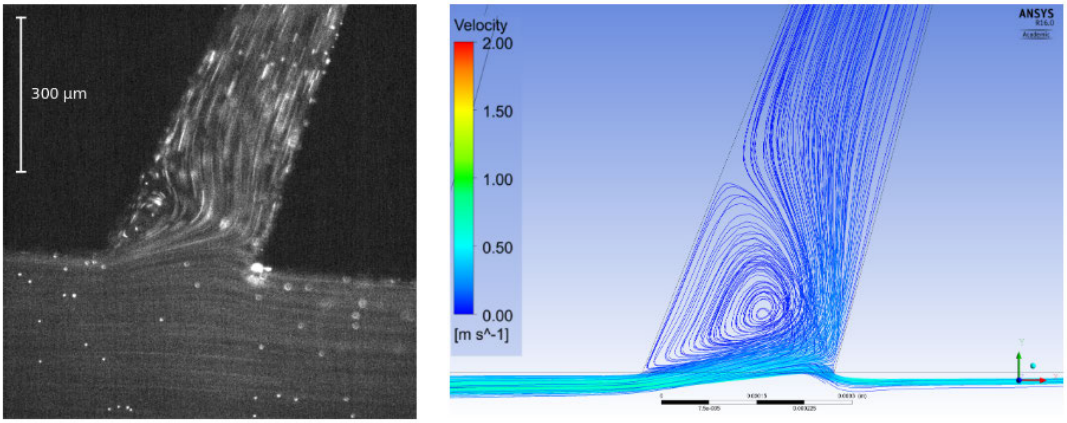
Figure 5: Pressure drop measurements for four different microchannel samples [23].

2.3.2 Flow: Fluorescence Measurements

To investigate the internal flow behaviour and to identify potential weak points in the design, flow visualisation measurements using fluorescence particles and a fluorescence microscope were conducted. Therefore, the particles were diluted in water and filled in the reservoir. The volumetric flow rate was gradually increased to examine potential changes in flow behaviour at higher flow rates. In figure 6 the results for $\dot{V} = 2\,\mathrm{mL/min}$ and $\dot{V} = 3\,\mathrm{mL/min}$ are shown and compared to the corresponding streamlines obtained from CFD simulations. At $\dot{V} = 3\,\mathrm{mL/min}$, the formation of a vortex structure in the entry region of a microchannel was observed. The simulation results tend to overpredict the formation of vortices. The exact position of the investigated microchannel entry region at the manifold is not specified. In figure 7 the results for $\dot{V} = 20\,\mathrm{mL/min}$ are shown. It was observed that with increasing the volumetric flow rate, the size of the vortex structure also grows [23].

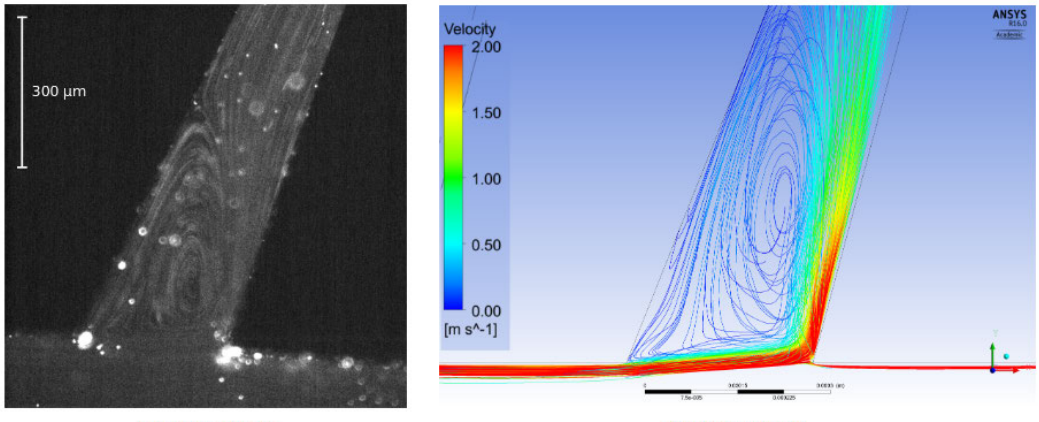


(c) 2 ml/min (d) 2 ml/min



(e) 3 ml/min (f) 3 ml/min

Figure 6: Fluorescence measurements (left) compared to CFD simulations (right) for $\dot{V} = 2\,\mathrm{mL/min}$ and $\dot{V} = 3\,\mathrm{mL/min}$ [23].



(c) 20 ml/min (d) 20 ml/min

Figure 7: Fluorescence measurements (left) compared to CFD simulation (right) for $\dot{V} = 20\,\mathrm{mL/min}$ [23].

2.3.3 Thermal: Pt100 Temperature Measurements

For the investigations of the thermal characteristics a heating mat was bonded to the underside of the sample. The heat dissipation power was set to 2.5 W, which is derived from the heat dissipation of a future micro-strip module for the ATLAS detector. For accurate measurements of the temperature at certain positions at the wafer surface, Pt100 sensors were used. The positions of the sensors are shown in figure 8. Specifications about the set temperature of the chiller and the actual inlet temperature measured with the flowmeter in the coolant circuit are not given. The measured temperatures on the wafer surface on line 1 are shown in figure 9.

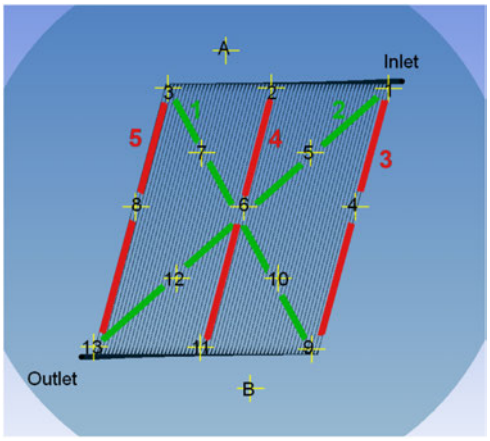
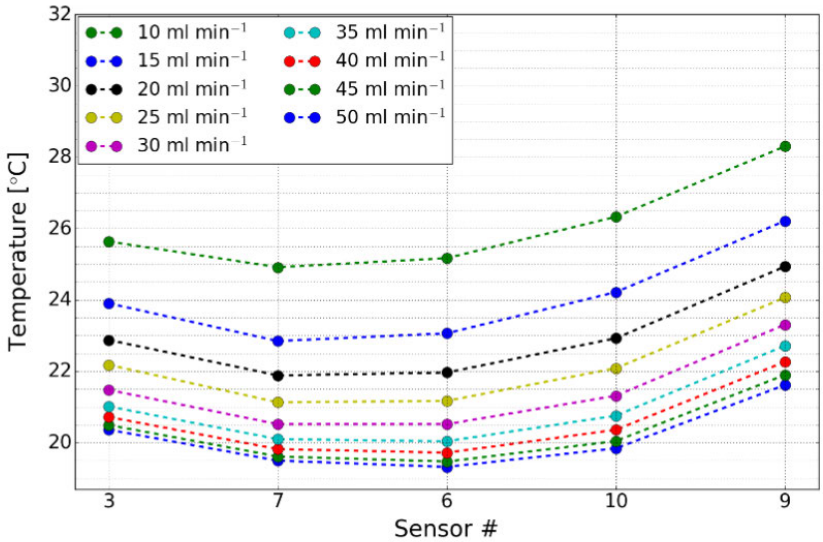


Figure 8: Arrangement of the Pt100 sensors on the wafer surface [23].

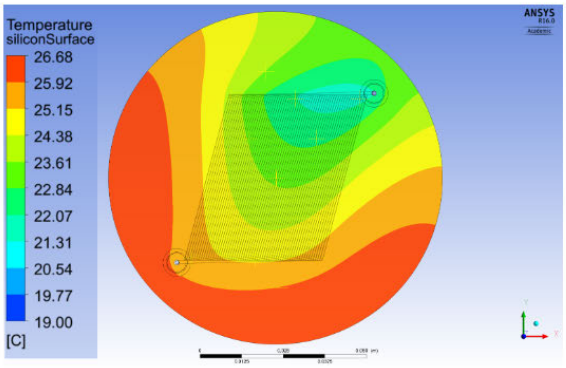


(a) Line 1 on the anodic bonded sample.

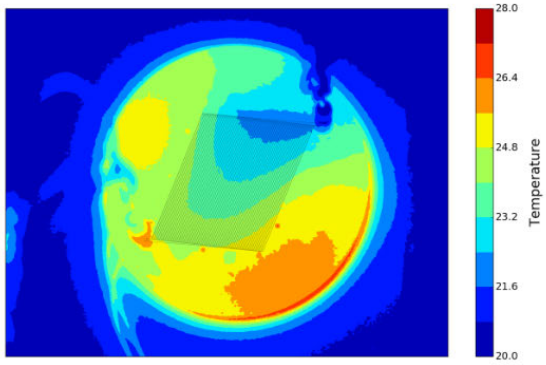
Figure 9: Measurements using Pt100 sensors on the wafer surface for different volumetric flow rates [23].

2.3.4 Thermal: Infrared Temperature Measurements

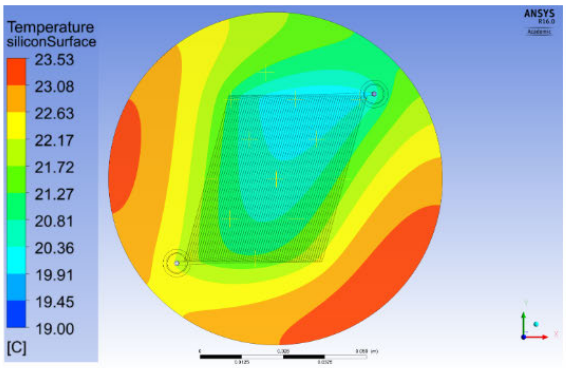
In figure 10 temperature measurements on the wafer surface with an infrared camera are compared with the results from CFD simulations. Here, also a heater mat with a set power of 2.5 W was used as a heat source. These measurements are used to investigate the temperature distribution on the whole surface of the wafer and allow a qualitative comparison with the results from CFD simulation. Similar to the Pt100 measurements, the thermal boundary conditions such as the coolant inlet temperature or the chiller setpoint are not specified.



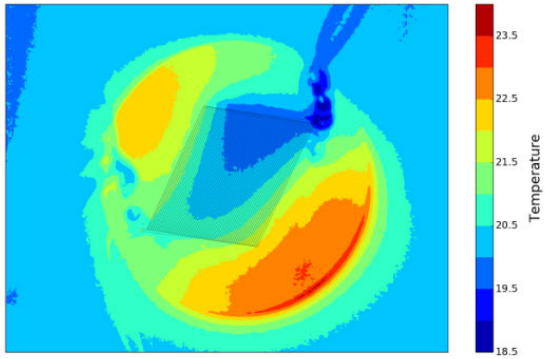
(a) Simulation with the anodic bonded sample with a flow rate of 10 ml min^{-1}.



(b) Experiment with the anodic bonded sample with a flow rate of 10 ml min^{-1}.



(c) Simulation with the anodic bonded sample with a flow rate of 30 ml min^{-1}.



(d) Experiment with the anodic bonded sample with a flow rate of 30 ml min^{-1}.

Figure 10: CFD simulations (left) compared to infrared temperature measurements (right) [23].

2.3.5 Design Modifications

After the dissertation, the size of the layout was adapted to meet the geometric requirements for an application as an interposer between a TimePix4 sensor and a Printed circuit board (PCB). The conceptual integration of the interposer into the system is illustrated in figure 11. In this application scenario, the microchannel layout has to fit on an area of 34 mm × 55 mm. To fulfil the geometrical requirements, the number of microchannels was reduced to 49 and the length of the microchannels was decreased to

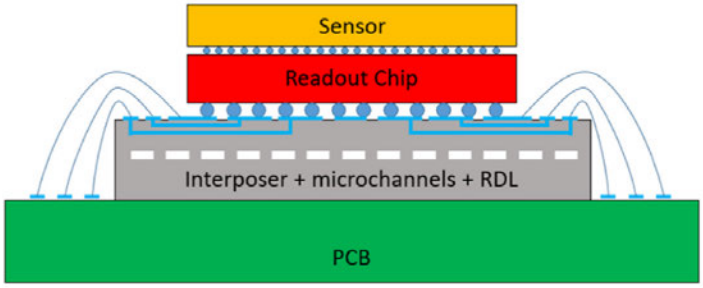


Figure 11: Application scheme of an interposer with microchannels [46].

approximately 30 mm. The tapering channel width of the manifold for 49 microchannels can be seen in figure 12, calculated with equation (1).

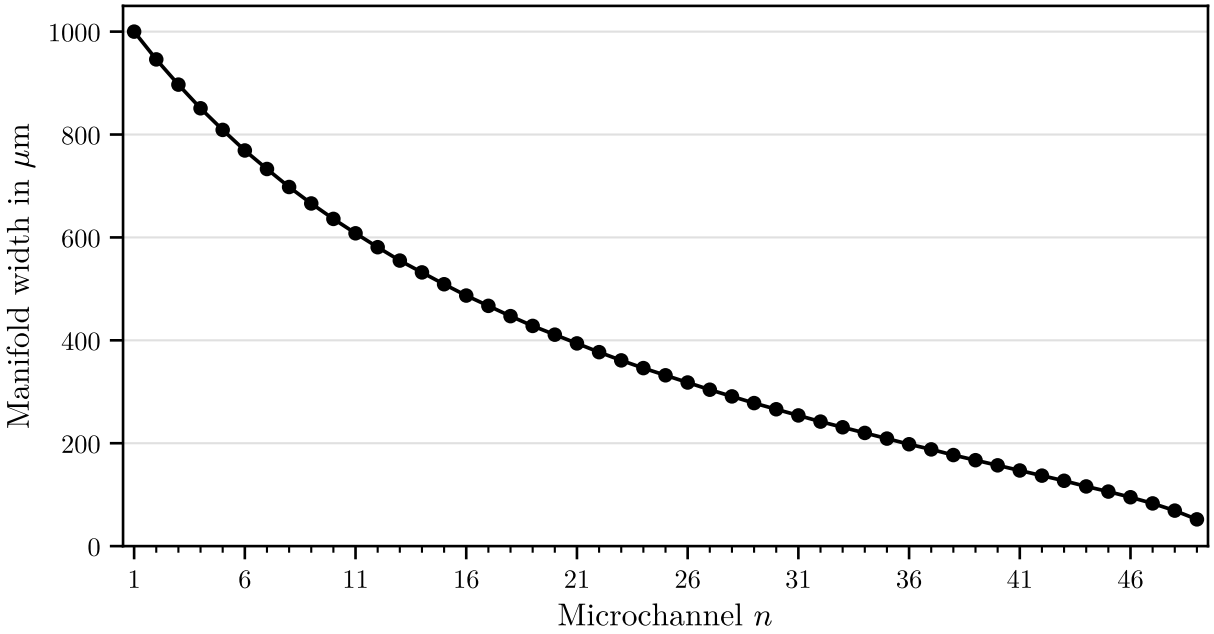


Figure 12: Calculated manifold width as a function of the microchannel index n according to equation (1).

Furthermore, the inlet and outlet regions of the microchannels were redesigned. The experimental observations in the fluorescence measurements, summarised in section 2.3.2, from the previous prototype showed vortex formation and local recirculation zones at the manifold to microchannel junctions. The modified interface geometry was therefore introduced to minimise these effects and reduce the total pressure drop.

The resulting layout of the current prototype design investigated in this work is shown in figure 13. This revised geometry represents the starting point for the analytical, numerical, and experimental investigations presented in the following chapters.

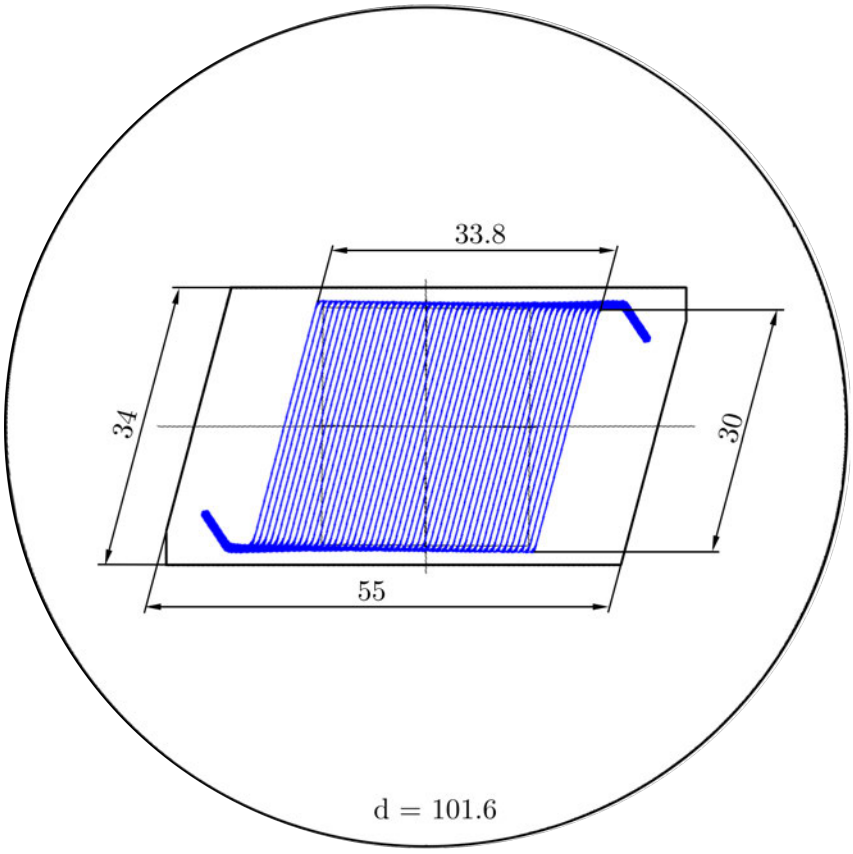


Figure 13: Current microchannel layout with outer dimensions (in mm) and geometric constraints for the application as interposer.

3 Fundamentals

In order to analyse the flow and heat transfer behaviour within the investigated microchannel system, a definition of the underlying physical principles is required. The following chapter introduces the fundamental governing equations and characteristic parameters, which provide the theoretical framework for the investigations presented in this work. The chapter is divided into the fundamentals of fluid dynamics and the fundamentals of heat transfer.

3.1 Fundamentals of Fluid Dynamics

This section summarises the fundamental equations governing incompressible internal flow in microchannels. Beginning with the conservation of mass, key flow characteristics such as flow regimes, Reynolds number and boundary layer development are introduced. These concepts form the foundation for the subsequent analysis of pressure losses and flow behaviour.

3.1.1 Continuity Equation (Conservation of Mass)

To describe the flow of a fluid streamlines are commonly used. A streamline is defined as a curve whose tangent at any point is aligned with the local velocity vector of the fluid and therefore represents the trajectory of a fluid particle. A streamtube is formed by a bundle of streamlines going through a closed curve. By definition, no fluid crosses the lateral surface of a streamtube. Furthermore, mass is neither created nor destroyed within the streamtube. Consequently, the conservation of mass requires that the mass flow rate remains constant along the streamtube. This leads to the continuity equation:

$$A_1 u_1 \rho_1 = A_2 u_2 \rho_2 = \dot{m} = \text{const.} \tag{2}$$

A describes the cross-sectional area of the streamtube, u the flow velocity, ρ the density of the fluid and $\dot{m}$ the mass flow rate. This relationship is schematically displayed in figure 14. For incompressible fluids, which is typically the case for liquid flow in microchannels, the density can be assumed as constant, resulting in a simplified form of the continuity equation with $\dot{V}$ as volumetric flow rate [7]:

$$Au = \dot{V} = \text{const.} \tag{3}$$

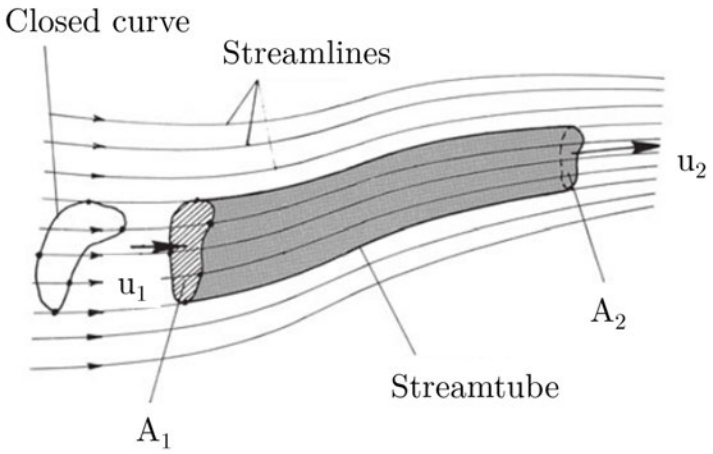


Figure 14: Streamtube representation illustrating the continuity equation for steady flow based on [7].

The theory of continuum is applicable for microchannel applications. It is not expected that significant differences between macrofluidic applications are observable [31].

3.1.2 Flow Regimes, Vortex Formation and Reynolds Number

Fluid flow can be classified into two distinct regimes, laminar and turbulent flow. Laminar flow is characterised by the smooth and orderly motion of fluid particles along clearly defined streamlines. In contrast, turbulent flow involves irregular and fluctuating velocity. The change from laminar to turbulent flow is referred to as transition [49].

The onset of transition is induced by a local change in pressure. In figure 15 the process of boundary layer separation is shown. The highest velocity prevails at the lowest pressure at point M. With an increasing pressure, the velocity is decreasing. If the delay is large enough, the flow detaches from the wall and a recirculation zone occurs. The separation of the flow is defined by the wall shear stress τ_w becoming zero:

$$\tau_w = \mu \cdot \left.\frac{\partial u}{\partial y}\right|_w = 0 \tag{4}$$

with the dynamic viscosity μ. In figure 15 the flow separation takes place at point A. Behind the flow separation point local negative velocity values are observable, which induces the formation of vortices. Besides the transition in a straight pipe from laminar to turbulent flow, flow separation is often induced by a pressure drop due to changes in the geometry of the flow domain [35].

The Reynolds number Re describes the ratio of inertial forces to viscous forces, defined by the following equation:

$$Re = \frac{\rho u L_\mathrm{c}}{\mu} = \frac{u L_\mathrm{c}}{\nu} \tag{5}$$

where ν denotes the kinematic viscosity and L_c the characteristic length. For circular pipes, the characteristic length is the diameter. For non-circular pipes, the hydraulic

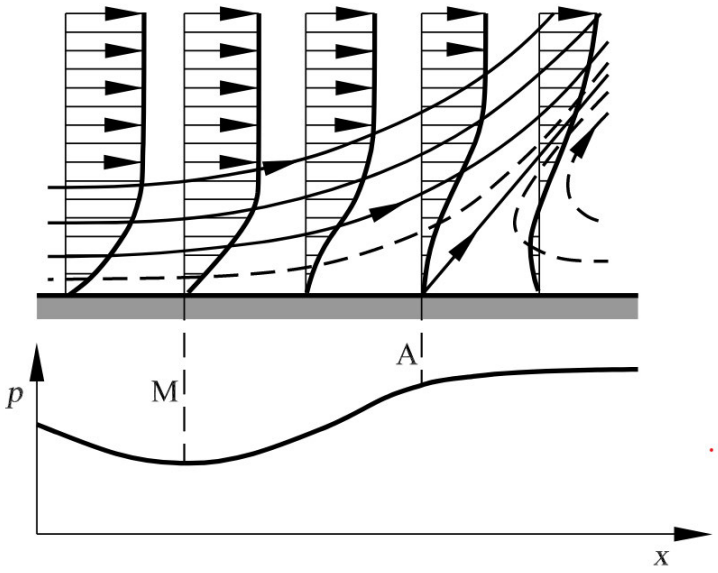


Figure 15: Schematic of boundary layer separation with associated pressure profile [35].

diameter D_h is used and defined as:

$$D_\mathrm{h} = 4 \cdot \frac{A}{P_\mathrm{w}} \tag{6}$$

where A denotes the cross-sectional area and P_w the wetted perimeter. Low Reynolds numbers indicate flows that are dominated by viscous effects and are usually associated with laminar flow. As the Reynolds number increases, flow instabilities develop and the transition to turbulence may occur. In microchannel cooling systems, Reynolds numbers are typically well below the critical value for this transition. Different studies show that the critical Reynolds number in different microchannel geometries is between 2000 and 2300, observing that the roughness of the channel surface is influencing the transition from laminar to turbulent [31]. Nevertheless, flow separation and recirculation zones may still occur. In particular, geometric discontinuities such as sharp corners, sudden expansions, and side-branch junctions may induce localized vortical structures even under laminar flow conditions.

From an engineering perspective, the formation of vortical structures and recirculation zones is not only relevant for the qualitative flow behaviour but also has an impact on the hydraulic performance of the system. Flow separation and recirculation lead to additional energy dissipation, which are local pressure losses. These losses contribute to an increase in the total pressure drop of the microchannel cooling system [26, 49].

3.1.3 Boundary Layer in Internal Flow

In internal flow viscous effects induced by the constraints of the bounding walls have an effect on the velocity profile of a fluid. This profile develops when a fluid enters a channel with an initially nearly uniform velocity profile. In the boundary layer the flow at the wall

is delayed and thereby accelerating the flow in the middle of the duct. At some point the boundary layer is fully developed and does not change any more in downstream direction. The length until this point is called entrance length ($L_{\mathrm{e,h}}$). During the development of the velocity profile, the pressure distribution along the channel is nonlinear. After the flow becomes fully developed, the pressure decreases linearly with the length [49]. The development of the boundary layer until the fully developed flow region is reached is shown in figure 16. The hydrodynamic entrance length can be calculated for laminar flow with the following equation [31]:

$$L_{\mathrm{e,h}} = 0.05\, Re\, D_{\mathrm{h}} \tag{7}$$

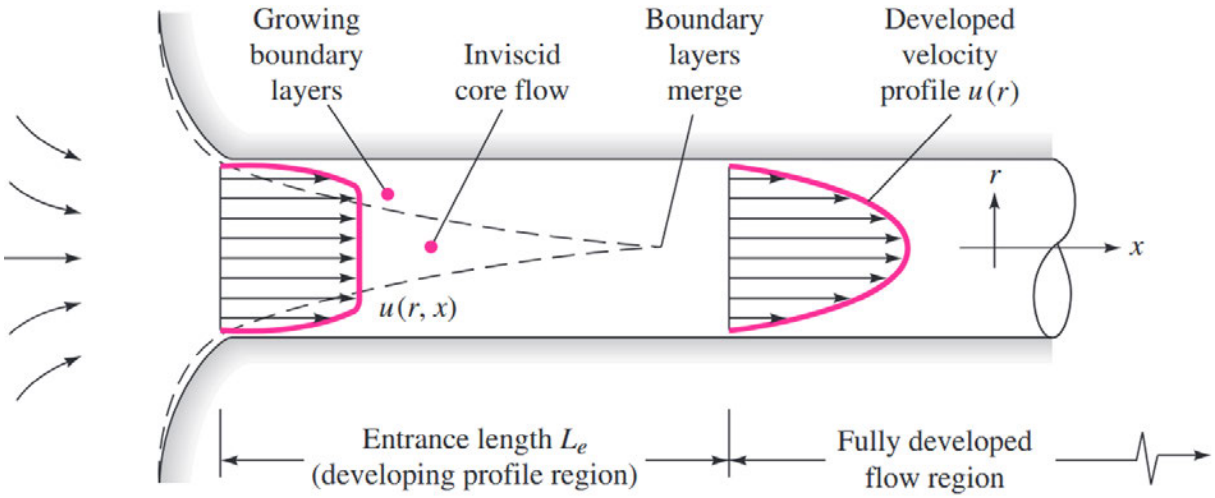


Figure 16: Development of the hydrodynamic boundary layer in a duct [49].

3.1.4 Pressure Losses in Internal Flow

Pressure losses in fluidic systems consist of contributions from friction in straight pipe sections as well as additional losses caused by components or geometric changes. For micro fluidic systems it is common to use the proportionality factor R_{hyd}, known as hydraulic resistance for the calculation of the pressure drop (Δp) through the system. The fundamental equation to determine the pressure drop is:

$$\Delta p = R_{\mathrm{hyd}}\, \dot{V} \tag{8}$$

This equation is only valid for laminar flow. In figure 17, equations to calculate R_{hyd} for straight channels with different cross-sectional shapes are shown. The equation presented exhibits an analogy to Ohm's law, $U = R \cdot I$. Therefore, a combination of hydraulic resistances can be considered as either parallel or in-series connected electrical resistances to calculate the total pressure loss through a system [12].

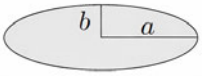
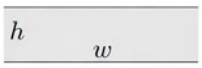
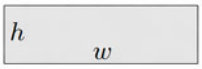
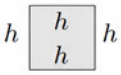
shape		R_{hyd} expression
circle		$\frac{8}{\pi}\mu L\frac{1}{a^4}$
ellipse		$\frac{4}{\pi}\mu L\frac{1+(b/a)^2}{(b/a)^3}\frac{1}{a^4}$
triangle		$\frac{320}{\sqrt{3}}\mu L\frac{1}{a^4}$
two plates		$12\,\mu L\frac{1}{h^3 w}$
rectangle		$\frac{12\,\mu L}{1-0.63(h/w)}\frac{1}{h^3 w}$
square		$\frac{12\,\mu L}{1-0.917\times 0.63}\frac{1}{h^4}$

Figure 17: Hydraulic resistances for straight channels with different cross-sectional shapes based on [12].

Local pressure losses are described using empirical loss coefficients. The general equation to calculate the local pressure drop is:

$$\Delta p = \zeta \cdot \rho \cdot \frac{u^2}{2} \tag{9}$$

The pressure loss coefficient ζ characterises pressure losses caused by junctions or other local disturbances in the flow. For a wide range of installations and boundary conditions, experimentally determined values of ζ are available in the literature [50]. An example, a side-branching junction is shown in figure 18, for which the corresponding pressure loss can be calculated using this approach.

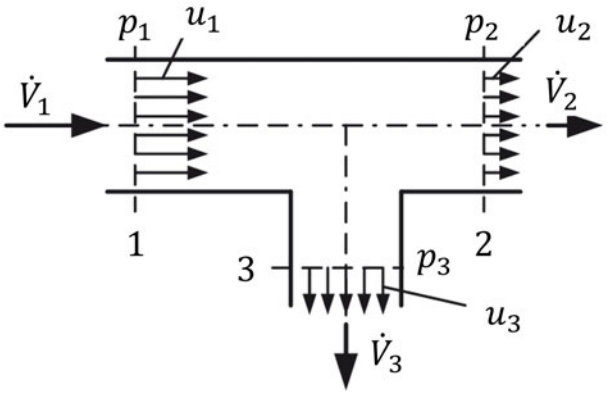


Figure 18: Fluid domain for a side-branching junction based on [50].

3.2 Fundamentals of Heat Transfer

This section describes the theoretical foundations of heat transfer, which are applied later in this work to analyse and model the given system. First, the fundamental quantities which are present in most heat transfer equations are explained. $\dot{Q}$ is the heat rate and describes the amount of heat transferred per unit of time. The rate of heat transfer per unit area is described as heat flux $\dot{q}''$. The connection between these quantities can be expressed by the following equation with A as the considered surface area [5]:

$$\dot{q}'' = \frac{\dot{Q}}{A} \tag{10}$$

3.2.1 First Law of Thermodynamics (Conservation of Energy)

A usual starting point for solving heat transfer problems is the first law of thermodynamics. Therefore, in the following the fundamentals of the first law will be described.

The first law of thermodynamics defines that the total energy of a system is conserved. It can be applied to closed systems (a region of fixed mass) or to open systems (a control volume, a region of space bounded by a control surface through which mass may flow). To describe the heat transfer by a coolant through a body, as it is present in this work, the equations for an open system are needed. In an open system the energy can cross boundaries by heat transfer through the boundaries, work done on or by the system and mass entering and leaving the control system carrying energy with it. Energy conservation leads to the mechanism that the rate of increase of energy stored in a control volume ($\dot{E}_{\mathrm{st}}$) must equal the rate at which energy enters the control volume ($\dot{E}_{\mathrm{in}}$), minus the rate at which energy leaves the system ($\dot{E}_{\mathrm{out}}$), plus the rate at which thermal and mechanical energy is generated within the control volume ($\dot{E}_{\mathrm{g}}$). This leads to the following equation:

$$\dot{E}_{\mathrm{st}} = \frac{dE_{\mathrm{st}}}{dt} = \dot{E}_{\mathrm{in}} - \dot{E}_{\mathrm{out}} + \dot{E}_{\mathrm{g}} \tag{11}$$

which is visualized in figure 19.

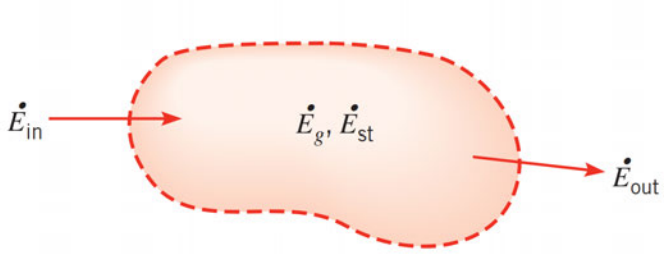


Figure 19: Schematic representation of the energy balance for an open system [5].

Using applied engineering quantities the energy balance of the control volume can be written as:

$$\frac{dE_{\mathrm{st}}}{dt} = \dot{Q} + P + \dot{m}\left((h_{\mathrm{in}} - h_{\mathrm{out}}) + g\,(z_{\mathrm{in}} - z_{\mathrm{out}}) + \frac{1}{2}\,(u_{\mathrm{in}}^2 - u_{\mathrm{out}}^2)\right) \tag{12}$$

Here, h describes the specific enthalpy. For the scenario considered in this thesis, mechanical work does not contribute to the energy balance. Accordingly, the mechanical power term P can be set to zero. Furthermore, changes in potential and kinetic energy are negligible, therefore the terms $g\,(z_{\mathrm{in}} - z_{\mathrm{out}})$ and $\frac{1}{2}\,(u_{\mathrm{in}}^2 - u_{\mathrm{out}}^2)$ vanish. Under the assumption of steady-state conditions, $\frac{dE_{\mathrm{st}}}{dt} = 0$, the equation can be simplified and rearranged for the calculation of the thermal power:

$$\dot{Q} = \dot{m}\,(h_{\mathrm{out}} - h_{\mathrm{in}}) \tag{13}$$

The right side of the equation represents the difference in enthalpy between outlet and inlet multiplied with the mass flow rate, which can also be expressed for incompressible fluids as:

$$\dot{Q} = \dot{m}\,c_{\mathrm{p}}\,(T_{\mathrm{out}} - T_{\mathrm{in}}) \tag{14}$$

Here, c_{p} denotes the specific heat capacity of the fluid [5].

3.2.2 Heat Conduction

Conduction describes heat transfer processes that are driven by temperature differences between or within solids, fluids or gases. The mechanism behind conduction is diffusion of molecules in fluids and lattice vibrations in solids.

For the wall shown in figure 20 heat transfer in x-direction can be described with the following equation for the heat flux:

$$\dot{q}'' = k\,\frac{T_1 - T_2}{L} \tag{15}$$

The corresponding heat transfer rate is given by:

$$\dot{Q} = k\,A\,\frac{T_1 - T_2}{L} \tag{16}$$

k denotes the thermal conductivity, which is a material property of the wall material. Heat is always transferred in the direction of decreasing temperature, which is expressed by the term $T_1 - T_2$ [5].

3.2.3 Convective Heat Transfer

Convection describes the combination of heat transfer due to diffusion and heat transfer by motion of the fluid. In this work the focus is on fluid flow through channels, which is

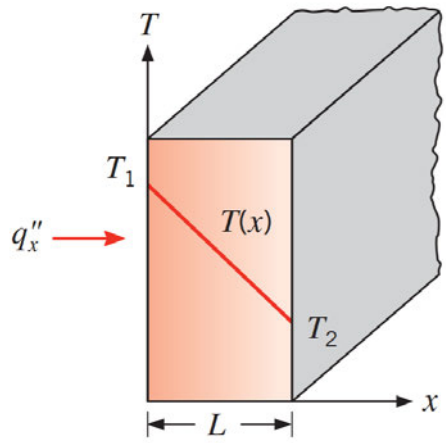


Figure 20: One-dimensional heat conduction through a plane wall [5].

so called forced convection, because the flow is caused by a pump. The convective heat flux due to forced convection at the surface of a channel is given by:

$$\dot{q}''_{\mathrm{s}} = \alpha(T_{\mathrm{s}} - T_{\mathrm{m}}) \tag{17}$$

α is the convective heat transfer coefficient, which depends on an assortment of fluid, thermodynamic and transport properties. T_{s} is the surface temperature at the wall of a channel and T_{m} is the mass-weighted mean temperature of the fluid. If $T_{\mathrm{s}} > T_{\mathrm{m}}$ heat is transferred from the wall into the fluid and if $T_{\mathrm{s}} < T_{\mathrm{m}}$ heat is transferred from the fluid to the wall [5].

3.2.4 Heat Transfer in Internal Flow

The flow velocity profile in the cross section of a duct, shown in section 3.1.3, is related to the thermal behaviour of a fluid in a duct. Similar to the hydrodynamic boundary layer, a thermal boundary layer is developing in the entrance region of a duct. The process of thermal boundary layer development is shown in figure 21. The fluid with a uniform temperature, which is less than the surface temperature of the pipe, enters a pipe. Due to the temperature difference convective heat transfer occurs and the thermal boundary layer starts to develop. For either a constant surface temperature T_{s} or a uniform heat flux across the walls of a duct, a fully thermal developed boundary layer is eventually established. The thermal entrance length ($L_{\mathrm{e,t}}$) until the thermal boundary for laminar flow is fully developed may be expressed as:

$$L_{\mathrm{e,t}} = 0.05\, Re\, Pr\, D_{\mathrm{h}} \tag{18}$$

Re denotes the Reynolds number, D_h the hydraulic diameter and Pr the Prandtl number.

The Prandtl number expresses the ratio between momentum and thermal diffusivities and is defined as:

$$Pr = \frac{c_\mathrm{p}\mu}{k} = \frac{\nu}{\alpha} \tag{19}$$

If $Pr < 1$, the hydrodynamic boundary layer is developing faster than the thermal boundary layer. Consequently, $L_{\mathrm{e,h}} < L_{\mathrm{e,t}}$. For large Prandtl numbers, the thermal boundary layer is developing faster, resulting in $L_{\mathrm{e,t}} < L_{\mathrm{e,h}}$ [5].

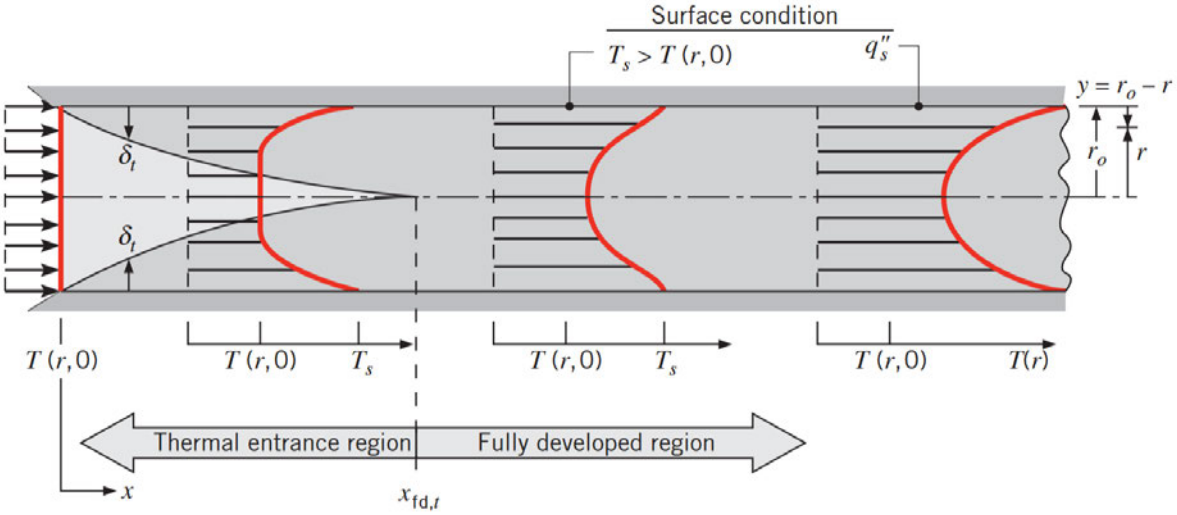


Figure 21: Thermal boundary layer development in a duct [5].

The Nusselt number Nu is a dimensionless parameter that characterises convective heat transfer between a wall and a fluid. It represents a dimensionless temperature gradient defined as the ratio of convective to purely conductive heat transfer and thus enables the description of the wall temperature T_s and the mass-weighted mean fluid temperature T_m. The Nusselt number is given by:

$$Nu = \frac{\alpha \cdot D_\mathrm{h}}{k} \tag{20}$$

where α denotes the convective heat transfer coefficient, D_h the hydraulic diameter of the channel, and k the thermal conductivity of the fluid. If the fluid in the pipe is not flowing and heat transfer happens fully conductive, $Nu = 1$. The Nusselt number depends on the flow regime and the channel geometry and is typically expressed as a function of the Reynolds and Prandtl numbers. Furthermore, it is influenced by the applied thermal boundary condition, such as constant wall temperature or constant wall heat flux [5, 48].

4 Analytical Modelling of Flow and Heat Transfer

In the following chapter the given microchannel geometry is analysed with the fundamental principles that are presented in chapter 3. The objective is to derive simplified relations and determine the parameters with the biggest impact on the fluid-dynamic and thermal behaviour for further design optimisation.

The analysis is structured in two parts. First, the fluid-dynamic behaviour is examined, focusing on the determination of relevant flow parameters and pressure losses. Subsequently, an analytical approach for modelling the thermal behaviour is developed, linking heat transfer mechanisms with the flow characteristics.

For all theoretical considerations, steady-state flow conditions are assumed. This assumption is justified because the experimental investigations are conducted under stable operating conditions after an initial transient phase. Consequently, time-dependent effects are neglected, allowing a simplified and consistent description of the fluid-dynamic and thermal behaviour.

4.1 Flow Model

The fluid-dynamic behaviour of the microchannel design is first examined using the analytical relations introduced in section 3.1. The purpose of this analysis is to identify flow-relevant regions and potential sources of pressure losses that should be investigated in greater detail within the subsequent CFD simulations and experimental studies.

4.1.1 Model Assumptions and System Boundaries

In order to describe the system, the layout was divided in sections to outline the area between the junction of each microchannel and the manifold, resulting in 49 sections for each manifold. Each microchannel is also considered as a section. The regions upstream the first section leading to the inlet of the microchannel sample and the regions downstream the last section in the outlet manifold are neglected in this consideration. The system boundaries for a section in the inlet manifold are displayed in figure 22. Each section begins and ends immediately downstream of a microchannel entrance. At this position, it is assumed that the entire fluid portion diverted from the manifold into

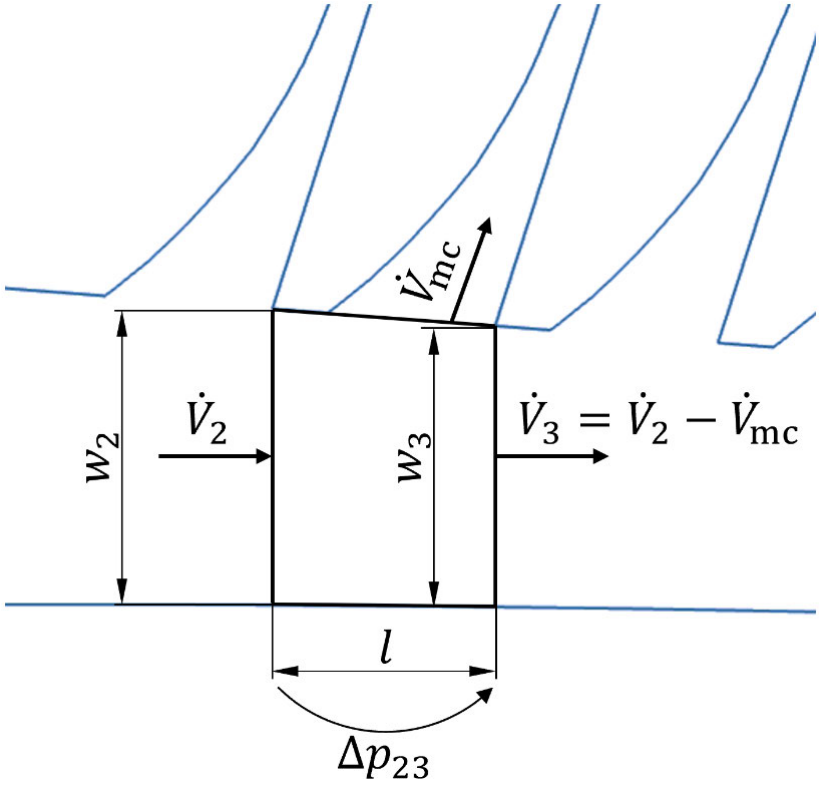


Figure 22: Control volume of manifold segment 2 with mass balance.

the microchannel has left the control volume, thereby establishing the inlet condition for the following section. The length of the section is measured in the CAD model. All sections have the same length of 0.6992 mm. In the case of the first section, this distance is defined in the upstream direction, measured from the end of the first microchannel entrance. The values for the width at the begin and end of a section are determined by using the measurement tool in the CAD model of the wafer.

4.1.2 Flow Characteristics

Based on the model described above, the flow behaviour within each section is evaluated in terms of flow velocity and Reynolds number. For further calculations, an averaged width is used, determined from the widths at the beginning and the end of the sections, as given by:

$$\bar{w}_n = \frac{w_n + w_{n+1}}{2} \tag{21}$$

The use of mean geometric quantities avoids unnecessary model complexity. With the mean width and the constant channel height $h = 0.1\,\text{mm}$ the cross-sectional area of a section can be calculated as:

$$\bar{A}_n = \bar{w}_n \cdot h \tag{22}$$

The same approach applies to the wetted perimeter:

$$\bar{P}_{\mathrm{w},n} = 2 \cdot (\bar{w}_n + h) \tag{23}$$

Using the mean cross-sectional area and the wetted perimeter, the hydraulic diameter is obtained from:

$$\bar{D}_{\mathrm{h},n} = 4 \cdot \frac{\bar{A}_n}{\bar{P}_{\mathrm{w},n}} \tag{24}$$

Based on the statement from the previous thesis, that there is homogeneous flow through all microchannels and applying the principle of conservation of mass (section 3.1.1), the volumetric flow rate per channel ($\dot{V}_{\mathrm{mc}}$) can be calculated by dividing the total volume flow $\left(\dot{V}\right)$ by the number of channels (N):

$$\dot{V}_{\mathrm{mc}} = \frac{\dot{V}}{N} \tag{25}$$

The volumetric flow rate along the manifold is decreasing at each junction by $\dot{V}_{\mathrm{mc}}$. At the beginning of any section n the volumetric flow rate is:

$$\dot{V}_n = \dot{V} - \dot{V}_{\mathrm{mc}} \cdot (n-1) \tag{26}$$

The volumetric flow rate can be set in the continuity equation. Together with the mean cross-sectional area, the flow velocity in the manifold for each section can be calculated with:

$$u_n = \frac{\dot{V}_n}{\bar{A}_n} \tag{27}$$

The calculated flow velocity is shown in figure 23. The results display, that the velocity increases downstream from the inlet. It reaches its maximum in the sections 27 and 28. From there the velocity decreases until it reaches its minimum in section 49. The difference between the maximum and the minimum value is around 2 m/s, which highlights significant differences in the flow speed along the manifold. This result motivates the investigation of changes in the flow behaviour based on the position in the manifold and the local flow velocity.

In addition to the flow velocity in the manifold, the Reynolds number in the microchannels is determined based on equation (5), to characterize the flow regime. The results for water and Novec7100 for several volumetric flow rates investigated in this work are presented in table 1. Novec7100 has consistently higher Reynolds numbers than water, which can be attributed to the smaller kinematic viscosity of Novec7100 ($\nu = 0.38 \times 10^{-6}\,\mathrm{m^2/s}$) in comparison to water ($\nu = 0.89 \times 10^{-6}\,\mathrm{m^2/s}$). All results indicate due to low numbers compared to common critical Reynolds number values, that laminar flow is the expected predominant flow regime.

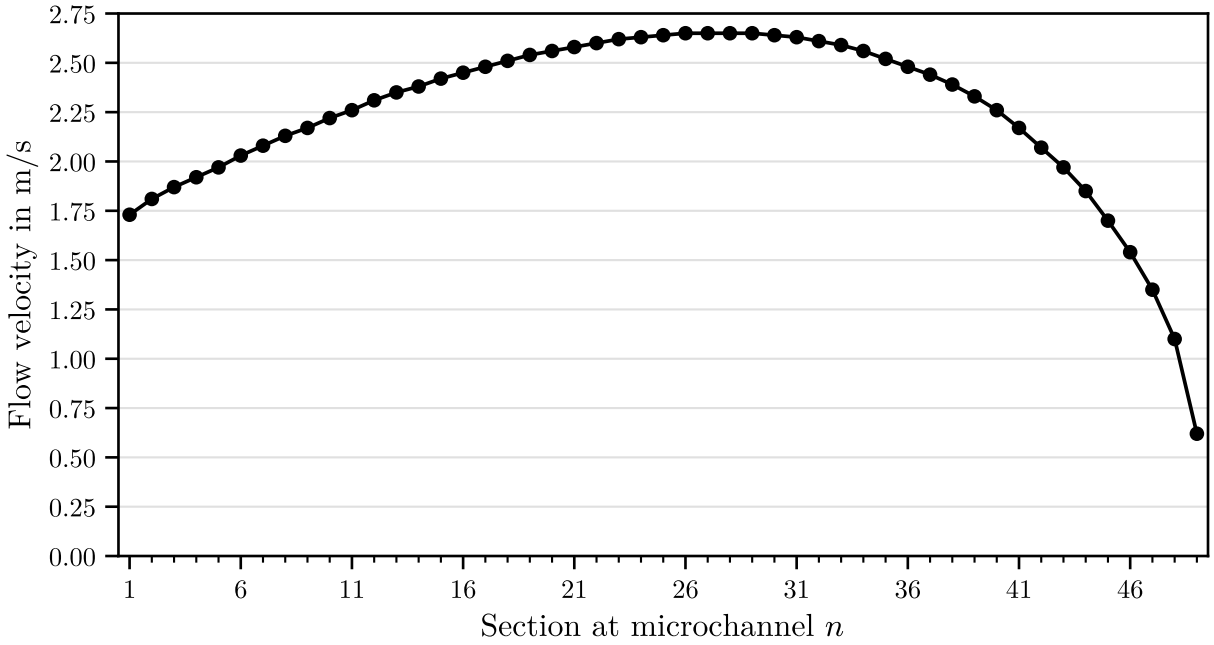


Figure 23: Calculated flow velocity along the inlet manifold for $\dot{V} = 10\,\mathrm{mL/min}$.

Table 1: Reynolds numbers in the microchannels for water and Novec7100 at different volumetric flow rates.

Volumetric flow rate [mL/min]	Re_{water}	$Re_{\mathrm{Novec7100}}$
10	38	90
20	76	179
30	114	269

4.1.3 Pressure

Following the analysis of the velocity and Reynolds number, the pressure within the system is considered. There are two mechanisms of pressure loss that need to be determined. The first is frictional loss through the channels, and the second is local loss induced by junctions in the system.

To determine the frictional pressure loss through the system, the hydraulic resistance for each section in the manifold and each microchannel is calculated. For the sections in the manifold the equation for rectangle cross-sectional shape in figure 17 is used and for the hydraulic resistance of a microchannel the equation for squared cross-sectional shapes is used. The calculation of the hydraulic resistance for section two in the inlet manifold and for a microchannel is illustrated as an example to clarify the approach. The hydraulic resistance for each microchannel is equal, due to the same geometry. Since the operating temperature is not defined at this point, the dynamic viscosity of Novec7100 at 25 °C is used. This value is obtained directly from the density and kinematic viscosity provided in the data sheet, without the need for interpolation [1]. The width is the mean value calculated with the width at the begin and the end of a section. The resulting hydraulic resistances are given by:

$$R_{2,\,\mathrm{in}} = \frac{12\mu L_{\mathrm{sec}}}{1 - 0.63(h/w)} \cdot \frac{1}{h^3 w} = 5.77 \times 10^9\,\mathrm{Pas/m^3} \tag{28}$$

$$R_{i,\,\mathrm{mc}} = \frac{12\mu L_{\mathrm{mc}}}{1 - 0.917 \cdot 0.63} \cdot \frac{1}{h^4} = 4.9 \times 10^{12}\,\mathrm{Pas/m^3} \tag{29}$$

where $\mu = 5.78 \times 10^{-4}\,\mathrm{kg/(m\,s)}$, $L_{\mathrm{sec}} = 0.70 \times 10^{-3}\,\mathrm{m}$, $L_{\mathrm{mc}} = 0.03\,\mathrm{m}$, $h = 0.10 \times 10^{-3}\,\mathrm{m}$, $w = 0.90 \times 10^{-3}\,\mathrm{m}$. L denotes the length of a section or the microchannel length and h the height. The calculation of the hydraulic resistance for the other sections is based on the same approach.

In figure 24, a part of the hydraulic resistance network derived from the layout of the microchannel sample is shown. Knowing the individual values of each resistance allows the determination of the total hydraulic resistance. The analogy to electrical resistances, which is mentioned in section 3.1.4, is used to take into account the interaction between the resistances. In the network are several connected Y-circuits. The network contains multiple interconnected Y-junctions, which can be transformed into equivalent Δ-circuits for analytical evaluation. However, due to the large number of resistances involved (149 in total), this approach would be time-consuming and prone to errors. Therefore, the total hydraulic resistance is obtained by simulating the equivalent circuit as an electrical circuit in LTSpice, with the result:

$$R_{\mathrm{hyd,\,Novec7100,\,total}} = 4.94 \times 10^{11}\,\mathrm{Pa\,s/m^3} \tag{30}$$

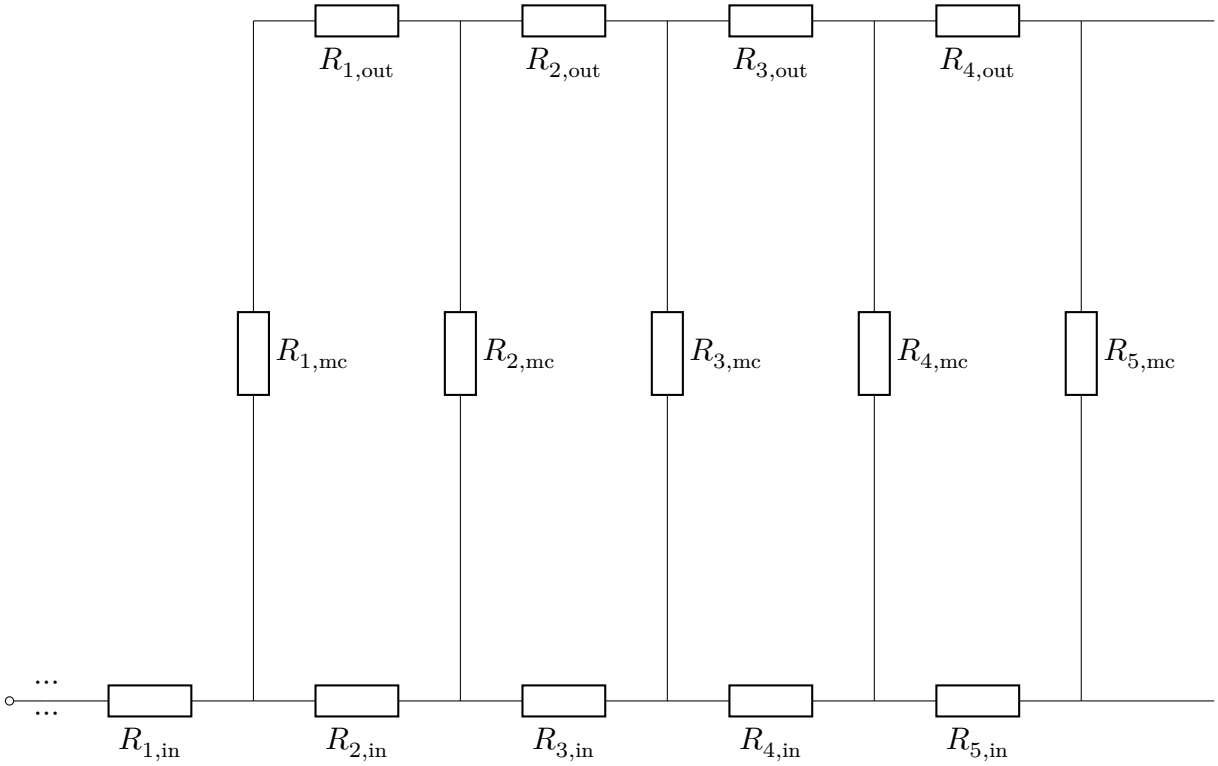


Figure 24: Hydraulic resistance network of the first five microchannels.

To have a reference the same procedure is repeated with the fluid properties for water at 25 °C ($\mu = 8.90 \times 10^{-4}\,\text{kg/(m s)}$ [48]). The obtained total hydraulic resistance for water is given by:

$$R_{\text{hyd, Water, total}} = 7.56 \times 10^{11}\,\text{Pa s/m}^3 \tag{31}$$

The calculation of the total pressure drop is performed using equation (8). The resulting pressure drops for different volumetric flow rates are presented in figure 25. For all investigated volumetric flow rates, the pressure drop obtained for water is significantly higher than for Novec7100. In addition, the pressure drop of water increases more steeply with increasing volumetric flow rate. Both observed trends can be attributed to the higher dynamic viscosity of water, which results in a higher hydraulic resistance compared to Novec7100.

Until now, only frictional losses have been considered, since under laminar flow conditions they scale linearly with the volumetric flow rate and can therefore be represented by constant hydraulic resistances. In contrast, local losses exhibit a quadratic dependence on the flow velocity, see equation (9). Consequently, they cannot be captured by the same linear hydraulic-resistance network. To investigate the occurring local losses, the junctions from the inlet manifold to the microchannel are considered. Therefore, the approach from the "Handbook of Hydraulic Resistance", shown in figure 26, is used. The symbols F and w used in the figure correspond to the cross-sectional area A and the flow velocity u used in this thesis. The geometric condition $F_\text{s} + F_\text{st} = F_\text{c}$ is not exactly satisfied. But the scheme represents the closest available model for the present

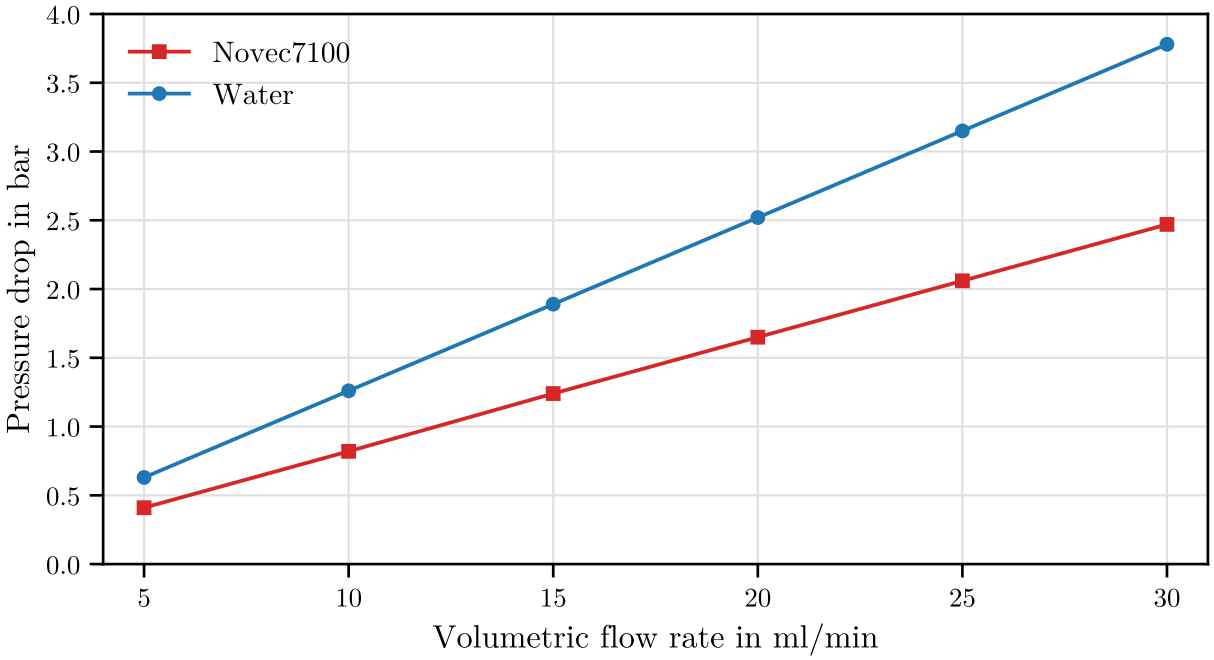


Figure 25: Pressure drop as a function of volumetric flow rate for water and Novec7100, calculated using the hydraulic resistance model.

configuration and is used to obtain an order-of-magnitude estimate of the local pressure losses and understand underlying parameters. First, the local pressure loss coefficient is calculated with the following equation:

$$\zeta_{c,s} = 1 + \left(\frac{w_s}{w_c}\right)^2 - 2 \cdot \frac{w_s}{w_c} \cdot \cos\alpha - K'_s \left(\frac{w_s}{w_c}\right)^2 \tag{32}$$

with $\alpha = 60°$ and K_s for $\alpha = 60°$, because it is the closest to the real angle ($\alpha = 75°$). w_s describes the flow velocity in a microchannel, which is under the assumption of homogeneous flow equal for each microchannel. w_c is the value of the flow velocity in the inlet manifold upstream of the microchannel entry.

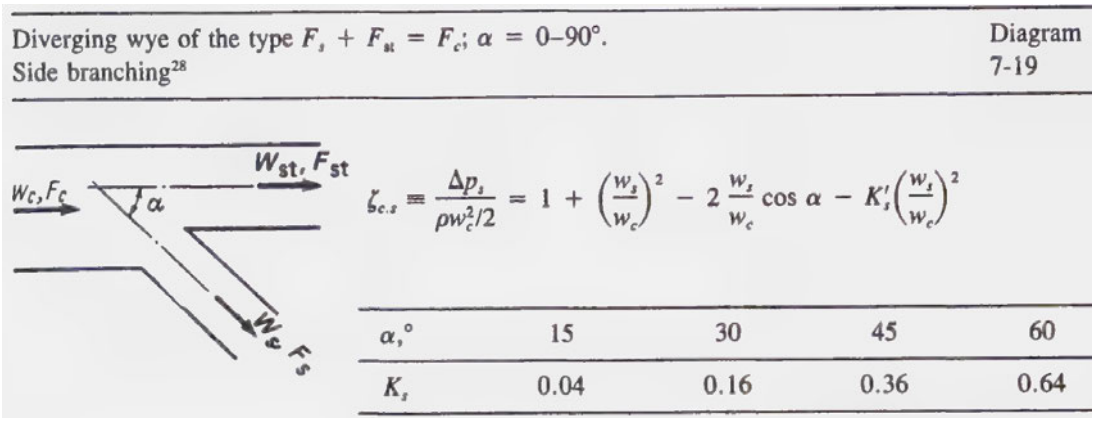


Figure 26: Calculation scheme for the determination of local pressure losses at a side-branch junction [26].

The local pressure drop (from manifold to microchannel) induced by the branch can be obtained from the following equation:

$$\Delta p_{\mathrm{s}} = \zeta_{\mathrm{c,s}} \cdot \rho \cdot \frac{w_{\mathrm{c}}^2}{2} \,. \tag{33}$$

The calculation is performed for every section once with the density of Novec7100 ($\rho = 1520\,\mathrm{kg/m^3}$) and once with the density of water ($\rho = 997.05\,\mathrm{kg/m^3}$) at 25 °C.

The results are shown in figure 27. The highest local pressure drops are observable in the middle of the manifold. This behaviour correlates with the velocity in the manifold and is also explainable with the influence of the velocity in the manifold to the local pressure drop (see equation (33)). Furthermore, the local pressure drops are significantly higher for Novec7100 than for water, which is attributable to the higher density of Novec7100. In addition, the observed trend can be discussed in terms of the Reynolds number (see section 3.1.2). For comparable flow conditions and geometry, the lower kinematic viscosity of Novec 7100 results in higher Reynolds numbers compared to water, which may promote increased flow separation and vortex formation at the junctions and therefore higher pressure losses. Furthermore, it has to be considered, that it raises quadratically with the flow velocity and plays therefore a further dominant role at higher flow rates.

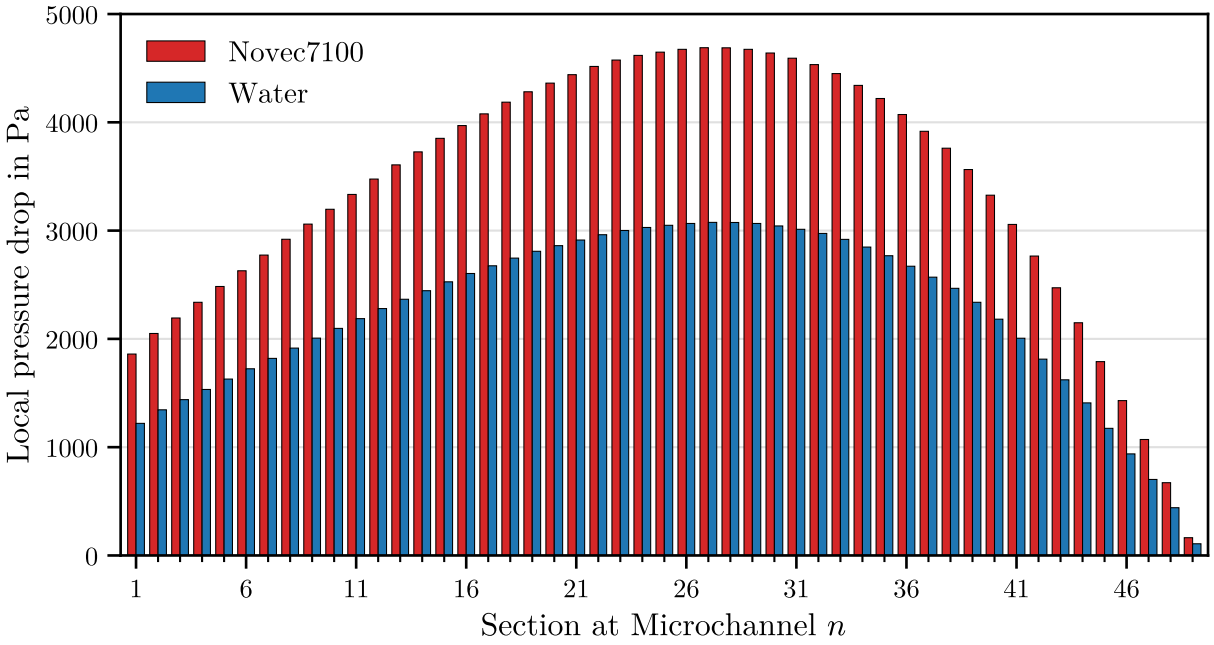


Figure 27: Local pressure drop at each microchannel entry induced by the branch ($\dot{V} = 10\,\mathrm{mL/min}$) for Novec7100 (red) and Water (blue).

4.2 Thermal Model

In this section an approach to model the thermal behaviour of the investigated microchannel layout is described. The model can be used to calculate the temperature rise of the coolant along the microchannels.

4.2.1 Model Assumptions and System Boundaries

In this subsection the simplifications and assumptions underlying the analytical model are described. The model only considers the microchannels, while the inlet and outlet manifolds are neglected. Furthermore, the microchannel heat sink is treated as a single solid body and is not modeled as two bonded wafers. Thermal contact resistances are therefore not taken into account. In addition, thermal interaction between the microchannels is neglected. Each microchannel is treated as thermally independent. All heat transferred into the solid is assumed to be uniformly distributed over the microchannel surfaces and is entirely removed by the coolant through forced convection. Heat exchanges due to natural convection or radiation to the environment are not considered. A sketch of the model is shown in figure 28.

To evaluate whether the heat transfer is influenced by thermal boundary layer development, the thermal entrance length was calculated using equation (18). For a volumetric flow rate of $\dot{V} = 10\,\mathrm{mL/min}$, the thermal entrance length is:

$$L_{\mathrm{e,t}} = 4.39\,\mathrm{mm} \tag{34}$$

For $\dot{V} = 30\,\mathrm{mL/min}$, the thermal entrance length is:

$$L_{\mathrm{e,t}} = 13.19\,\mathrm{mm} \tag{35}$$

The Reynolds numbers for the respective flow rates were taken from table 1. Using the properties of Novec7100 at 25 °C (according to the manufacturer's data sheet [1]), the Prandtl number is determined with equation (19), resulting in:

$$Pr = 9.82 \tag{36}$$

The hydraulic diameter of the microchannels $D_{\mathrm{h}} = 0.1\,\mathrm{mm}$ is used to calculate the thermal entrance length. The calculated thermal entrance length remains smaller than the total channel length for both investigated flow rates. At $\dot{V} = 10\,\mathrm{mL/min}$, the entrance region accounts for approximately 15 % of the channel length, while at $\dot{V} = 30\,\mathrm{mL/min}$ it extends to about 44 %.

Consequently, a significant length of the channel is thermally fully developed, particularly at lower volumetric flow rates. For a first-order analytical modelling approach,

the assumption of a fully developed thermal boundary layer is therefore adopted. The influence of the entrance region on the heat transfer is expected to be limited.

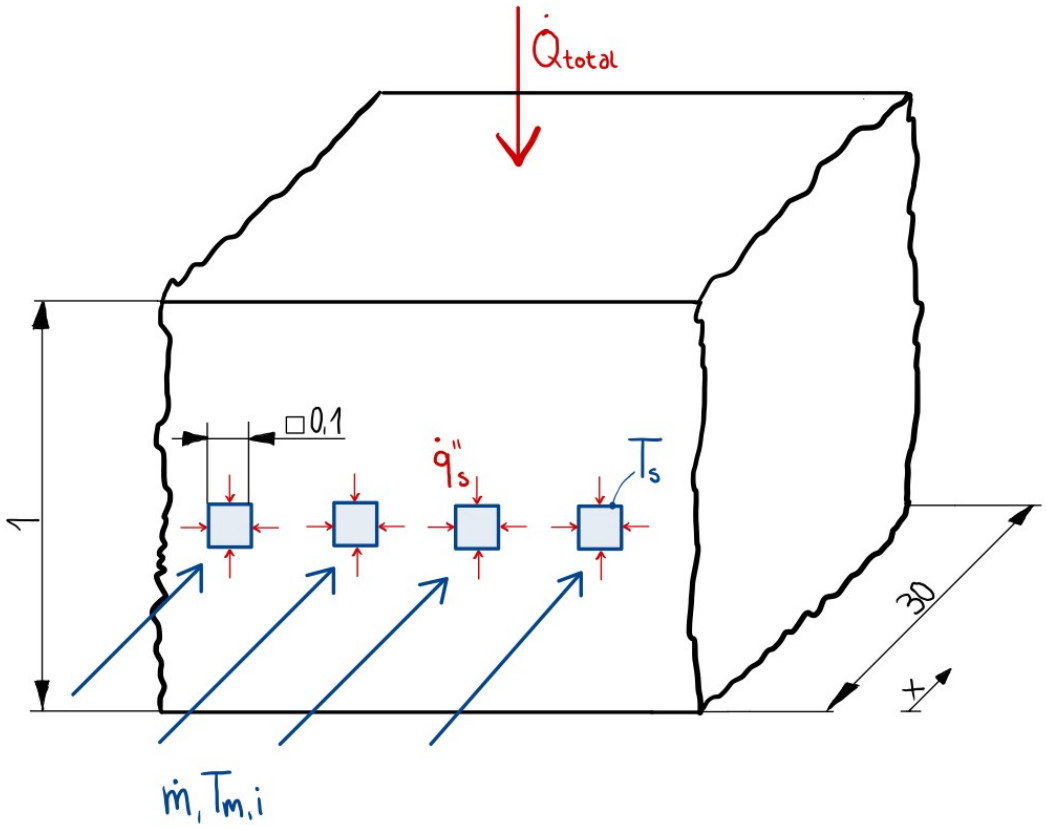


Figure 28: Schematic of the simplified system for analytical modelling, showing the heat input, microchannel entry conditions and thermal boundary conditions.

4.2.2 Analysis of Temperature Rise in a Microchannel

In this subsection, the fundamental equations of heat transfer are applied to the previously described model. Due to the assumption that the heat entering the wafer is uniformly distributed over the surfaces of all N microchannels, the relationship is given by:

$$\dot{Q}_{\text{total}} = N\dot{Q}_s \tag{37}$$

where $\dot{Q}_s$ denotes the heat rate per individual microchannel. Rearranging yields:

$$\dot{Q}_s = \frac{\dot{Q}_{\text{total}}}{N} \tag{38}$$

Based on equation (10), the heat flux at the microchannel walls is defined as the heat rate divided by the heat transfer area of a single channel:

$$\dot{q}''_s = \frac{\dot{Q}_s}{P_{\text{w}} \cdot L} \tag{39}$$

where P_w is the wetted perimeter and L the channel length. Substituting $\dot{Q}_s$ results in:

$$\dot{q}_s'' = \frac{\dot{Q}_{\text{total}}}{N \cdot P_{\text{w}} \cdot L} \tag{40}$$

To determine the rise of the coolant temperature, the first law of thermodynamics is applied to a differential control volume of length dx, which represents the fraction of a single microchannel, yields:

$$\dot{m}_{\text{c}} \cdot c_{\text{p}} \cdot dT_{\text{m}} = \dot{q}_s'' \cdot P_{\text{w}} \cdot dx \tag{41}$$

The energy balance describes the relationship between the increase in fluid enthalpy on the left-hand side and the heat transferred to the fluid through the microchannel wall on the right-hand side. Rearranging gives:

$$\frac{dT_{\text{m}}}{dx} = \frac{\dot{q}_s'' \cdot P_{\text{w}}}{\dot{m}_{\text{c}} \cdot c_{\text{p}}} \tag{42}$$

Integrating from $x = 0$ to x results in:

$$T_{\text{m}}(x) = T_{\text{m,i}} + \frac{\dot{q}_s'' \cdot P_{\text{w}}}{\dot{m}_{\text{c}} \cdot c_{\text{p}}} \cdot x \tag{43}$$

This expression describes the linear increase of the mass-weighted mean fluid temperature by calculating the temperature at the axial coordinate x along the microchannel with the initial temperature $T_{\text{m,i}}$. The wall temperature can be described, using the convective heat transfer coefficient α:

$$\alpha = \frac{Nu \cdot k}{D_{\text{h}}} = 2476.1\,\text{W}/(\text{m}^2\,\text{K}) \tag{44}$$

The Nusselt number for a microchannel heated from four sides with an aspect ratio of 1 is taken from Table 3.3 in [31], yielding $Nu = 3.599$. With $k = 0.0688\,\text{W}/(\text{m}\,\text{K})$, the thermal conductivity of Novec7100 and $D_{\text{h}} = 1 \times 10^{-4}\,\text{m}$, the convective heat transfer coefficient follows accordingly. The equation to determine the wall temperature of a microchannel at length x is then given by:

$$T_{\text{s}}(x) = T_{\text{m}}(x) + \frac{\dot{q}_s''}{\alpha} \tag{45}$$

In the following, equation (43) and equation (45) are used to determine, exemplarily, the rise in temperature in the fluid and on the microchannel wall and thereby to describe the effect of each parameter on the result. The total heat load, which is used as reference, is given by [23], which represents the dissipation power of an existing particle detector, $\dot{Q}_{\text{total}} = 2.5\,\text{W}$. Dividing this through the total number of microchannels $N = 49$, the wetted perimeter $P_{\text{w}} = 4 \times 10^{-4}\,\text{m}$ and the channel length of $L = 0.03\,\text{m}$, which are all

geometric properties from the given design, resulting in:

$$\dot{q}_s'' = \frac{\dot{Q}_{\text{total}}}{N \cdot P_{\text{w}} \cdot L} = 4251.7\,\text{W/m}^2 \tag{46}$$

$T_{\text{m,i}}$ denotes the temperature of the fluid when entering the microchannel and $\dot{m}_{\text{c}}$ describes the mass flow of coolant going through the microchannel. These are the key parameters for the temperature rise because they are not constant values determined by fluid properties, such as the specific heat capacity $c_{\text{p}} = 1170\,\text{J/(kg K)}$ for Novec7100 at 25 °C or geometric boundary conditions, such as the wetted perimeter and the length ($x = L$) of a microchannel.

For an initial estimate, the fluid temperature at the begin of the microchannel is assumed to be $T_{\text{m,i}} = 298.15\,\text{K}$. The mass flow rate per microchannel ($\dot{m}_{\text{c}}$) is obtained by assuming a homogenous distribution of the total volumetric flow $\dot{V} = 10\,\text{mL/min}$ among all microchannels and using the density $\rho = 1520\,\text{kg/m}^3$ of Novec7100 at 25 °C, resulting in $\dot{m}_{\text{c}} = 5.16 \times 10^{-6}\,\text{kg/s}$. The mean temperature of the fluid at the end of the microchannel is:

$$T_{\text{m}}(L) = 306.6\,\text{K} \tag{47}$$

Accordingly, the temperature difference along the microchannel is:

$$\Delta T = T_{\text{m}}(L) - T_{\text{m}}(0) = 8.45\,\text{K} \tag{48}$$

The temperature difference between the wall temperature and the mean fluid temperature is defined as:

$$\Delta T_{\text{s-m}}(x) = T_{\text{s}}(x) - T_{\text{m}}(x) \tag{49}$$

Using equation (44) and equation (45), the wall temperature at the channel outlet becomes:

$$T_{\text{s}}(L) = 308.31\,\text{K} \tag{50}$$

Since the analytical solution predicts a constant offset between wall and mean fluid temperature along the microchannel, the temperature difference evaluates to:

$$\Delta T_{\text{s-m}} = T_{\text{s}} - T_{\text{m}} = 1.72\,\text{K} \tag{51}$$

The overall temperature rise along the microchannel (equation (48)) is compared to the difference between the wall and the fluid (equation (51)) to assess its relative magnitude. The wall-to-fluid temperature difference is significantly smaller than the overall temperature increase.

The temperature difference between the microchannel wall and the wafer surface ($\Delta T_{\text{wafer-s}}$) can be determined from a one-dimensional conduction model using equa-

tion (15):

$$\Delta T_{\mathrm{wafer-s}} = T_{\mathrm{wafer}} - T_{\mathrm{s}} = \frac{\dot{q}''_s L}{k} = 0.011\,\mathrm{K} \tag{52}$$

Here, L denotes the distance between the microchannel wall in the silicon wafer and the wafer surface ($L = 0.4 \times 10^{-3}\,\mathrm{m}$), and k is the thermal conductivity of silicon ($k = 148\,\mathrm{W/(m\,K)}$). As this temperature difference is negligible, the microchannel wall temperature is assumed to represent the wafer surface temperature with sufficient accuracy.

4.2.3 Effect of Non-Uniform Inlet Temperature on Temperature Distribution

To investigate the thermal behaviour to variations in the inlet conditions $\dot{m}_{\mathrm{c}}$ and $T_{\mathrm{m,i}}$, the analytical model above was used to determine the axial temperature profile along each microchannel. The temperature values are determined in 1 mm-steps along the microchannel length and visualised in a colour map (see figure 29).

Based on the previously defined assumption uniform mass flow distribution is considered, resulting in $\dot{m}_{\mathrm{c}} = 5.16 \times 10^{-6}\,\mathrm{kg/s}$ for each microchannel. Due to the geometric configuration of the inlet manifold, a non-uniform inlet temperature distribution is expected. As coolant is continuously extracted into the microchannels along the manifold, the remaining mass flow in the manifold decreases. Consequently, the temperature rise to the end is expected to increase. To represent this behaviour qualitatively, an inlet temperature profile with a stronger temperature increase towards the end of the manifold is assumed. This behaviour is described using the following quadratic function:

$$T_{\mathrm{m,i}}(n) = T_0 + \Delta T_{\mathrm{manifold}} \left(\frac{n-1}{N-1} \right)^2 \tag{53}$$

where n denotes the channel number and N the total number of microchannels. To maintain an average inlet temperature of approximately 298.15 K across all channels, the parameters $T_0 = 297.5\,\mathrm{K}$ and $\Delta T_{\mathrm{manifold}} = 2\,\mathrm{K}$ were selected. The resulting inlet temperature for each microchannel is also shown in figure 29. Figure 29 shows an increase of T_{s} in x-direction but also with increasing channel index. The highest temperature occurs at the outlet of the last microchannel ($x = L$, $n = N$). Since the axial temperature rise is identical for all channels, the rise in the temperature along the manifold is solely caused by the prescribed inlet temperature $T_{\mathrm{m,i}}(n)$. Consequently, a homogeneous mass flow distribution does not necessarily minimise the surface temperature spread. Increasing the coolant mass flow in the latter channels at the manifold reduces the axial temperature rise and can therefore compensate the higher inlet temperature toward the end of the manifold.

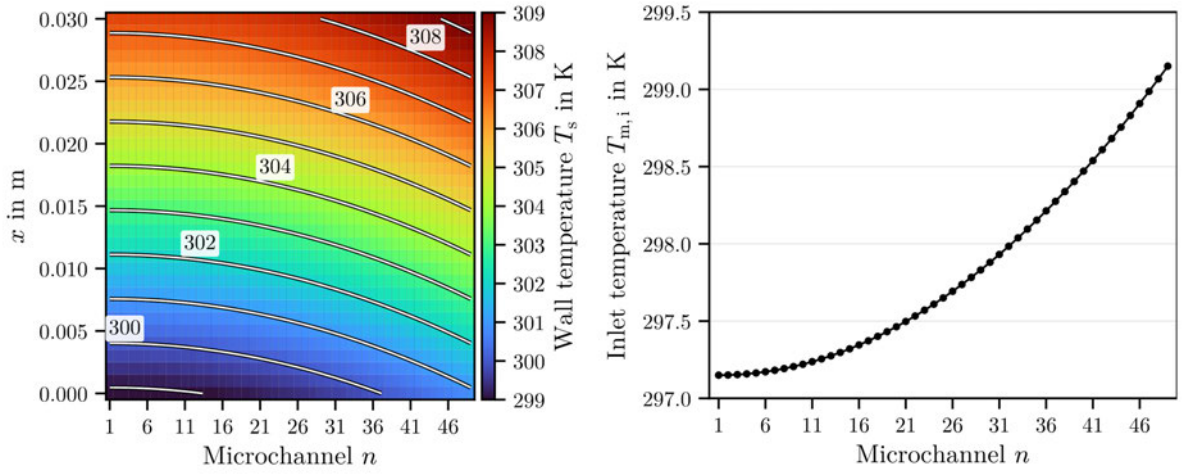


Figure 29: Colour map of the wall temperature T_s along the microchannels and its fluid inlet temperature $T_{\mathrm{m,i}}$ for theoretical conditions (homogeneous mass flow and steadily increasing $T_{\mathrm{m,i}}$).

5 CFD Simulation

In addition to the analytical modelling, numerical simulations are carried out with Ansys Fluent 2023 R2. The simulations provide a more detailed understanding of the flow and heat transfer behaviour within the investigated microchannel system.

The first part of this chapter focuses on fluid flow simulations, investigating pressure drop, vortex formation in the microchannel entry regions and flow distribution through the microchannels. The second part shows thermal simulations to investigate the temperature behaviour of the coolant through the microchannels and on the wafer surface.

All simulations are performed under steady-state conditions, consistent with the assumptions made in the analytical model.

5.1 Flow Simulation

In the following section, the flow simulation model and the corresponding numerical setup is described. The objective is to obtain physically consistent and reproducible results with stable and converged solution values. First, the fundamental CFD model is presented. It is then slightly modified for specific simulations, as described below.

5.1.1 Geometry

First, the fluid domain is derived from the microchannel fabrication layout (see figure 13). Based on this layout, a three-dimensional CAD model is created in Siemens NX and subsequently exported as a .STEP file. The geometry is then imported into *SpaceClaim*, the geometry tool of Ansys. Here, the fluid volume is divided into distinct parts: the inlet, inlet manifold, microchannel entries, microchannels and microchannel exits, outlet manifold and outlet. In figure 30 the principle is illustrated, using the first five microchannels at the inlet manifold as an example. This forms the basis for adapting the mesh sizes locally. To enable a conforming mesh through all individual parts, the *Share Topology* option is set to *Share*. The meshing strategy is described in the following subsection.

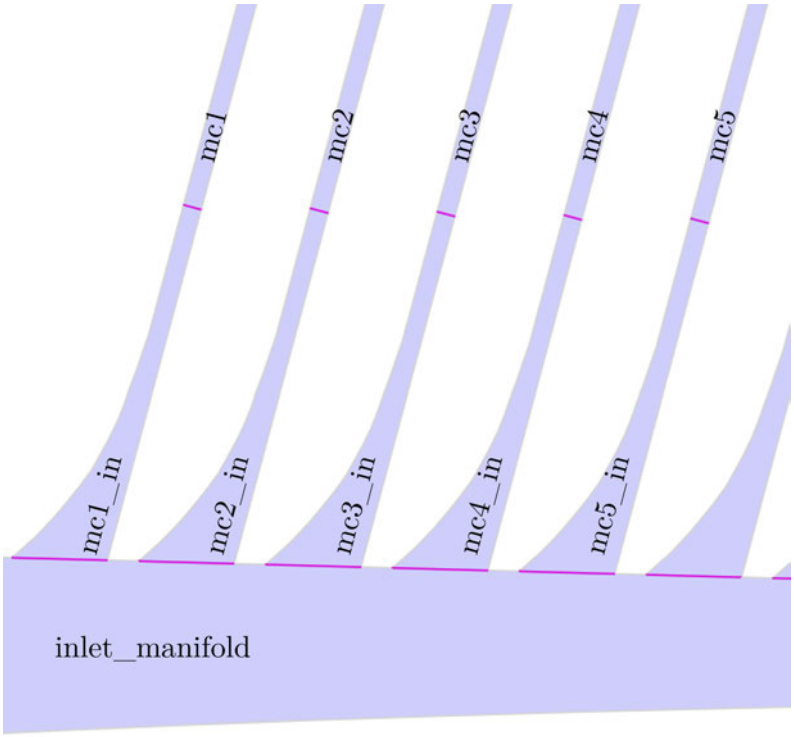


Figure 30: Subdivided CFD fluid domain at the inlet manifold showing the first five microchannels.

5.1.2 Mesh Generation

The primary objective of the meshing is to obtain a physically reliable CFD model with stable and convergent solution quantities, while ensuring that the simulation remains within the limits of the available computational resources. The applied meshing method is *MultiZone* with *Hexa/Prism* as *Mapped/Swept* type. *MultiZone* meshing automatically generates a pure hexahedral mesh where possible and fills the more complex regions with unstructured elements [3]. Numerical accuracy is higher when hexahedral control volumes are used instead of tetrahedral ones. In addition, the accuracy is further improved when grid lines follow the streamlines of the flow, which can be achieved using hexahedral meshes [22]. The microchannels are resolved with a structured mesh which is aligned to the predominant flow direction. In the inlet and outlet regions of the microchannels as well as in the manifolds, prismatic elements are combined with hexahedral elements to accommodate geometric transitions. Overall, the *MultiZone* meshing approach provides an effective compromise between numerical accuracy and geometric flexibility for the present complex geometry.

Local mesh refinement is realised using body sizing controls. The element size in the manifolds is set to 0.05 mm. In the inlet and outlet regions of the microchannels, a finer element size of 0.01 mm is applied. This sizing also defines the mesh resolution along the entire length of the microchannels, resulting in ten elements across the width and height of each microchannel. The element size of the inlet and outlet of the sample is

set to 0.01 mm. The global mesh size is set to 0.5 mm, this defines the distance between the nodes along the microchannel.

In total, 5 143 283 Nodes and 4 434 500 Elements are generated. The resulting mesh and most relevant regions are shown in figure 31 and figure 32. The mesh quality metrics are presented in table 2.

Table 2: Mesh quality metrics.

Quality criterion	Worst value
Maximum aspect ratio	51.5
Minimum orthogonal quality	0.26
Maximum skewness	0.89

The relatively high aspect ratio and skewness values are a consequence of the elongated control volumes along the microchannels with a height and width of 0.01 mm and a length of 0.5 mm. Provided that conservation of mass ($\dot{m}_{\text{in}} = \dot{m}_{\text{out}}$) is fulfilled and the solution has a stable convergence behaviour for residuals, mass flow and pressure drop, the quality metrics are in an acceptable range.

Due to meshing conflicts based on the complex geometry, the integration of inflation layers was not feasible with *MultiZone* meshing. Therefore, a flow-aligned mesh was preferred over an unstructured mesh with inflation layers, as it provides a more accurate representation of the dominant streamwise gradients in the microchannels, despite the fact that inflation layers would further enhance the near-wall resolution. Moreover, no stable simulation could be achieved using an unstructured mesh with inflation layers. Therefore, for the present geometry, a flow-aligned hexahedral mesh provides a more robust and accurate solution than an unstructured mesh with inflation layers. A further subdivision of the microchannels is not feasible due to limitations in the available computational resources. The next finer possible mesh size that allows an integer number of elements across the channel dimensions is 0.006 25 mm, resulting in 16 elements per width and height. This refinement increases the total number of elements to approximately 17 000 000 elements, which exceeds the available computational resources.

Since a laminar flow model is applied, no wall functions are used and the near-wall region is directly resolved with the applied mesh. The dimensionless wall distance y^+ is therefore used as an indicator of the near-wall mesh resolution. As a benchmark the y^+ value is determined exemplarily for a volumetric flow rate of $\dot{V} = 10\,\text{mL/min}$. For fully developed laminar flow in a square channel, the friction factor λ is given by [5]:

$$\lambda = \frac{57}{Re} = 1.49 \tag{54}$$

The corresponding Reynolds numbers are shown in table 1. Based on this, the wall shear stress is calculated as:

$$\tau_{\text{w}} = \frac{1}{2}\lambda\rho u^2 = 86.15\,\text{kg}/(\text{m}\,\text{s}^2) \tag{55}$$

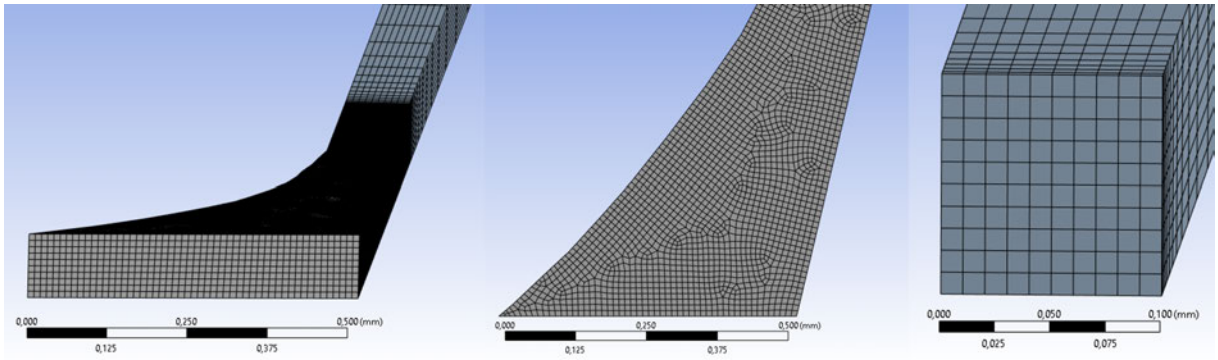


Figure 31: Generated mesh of the microchannels and the microchannel entries.

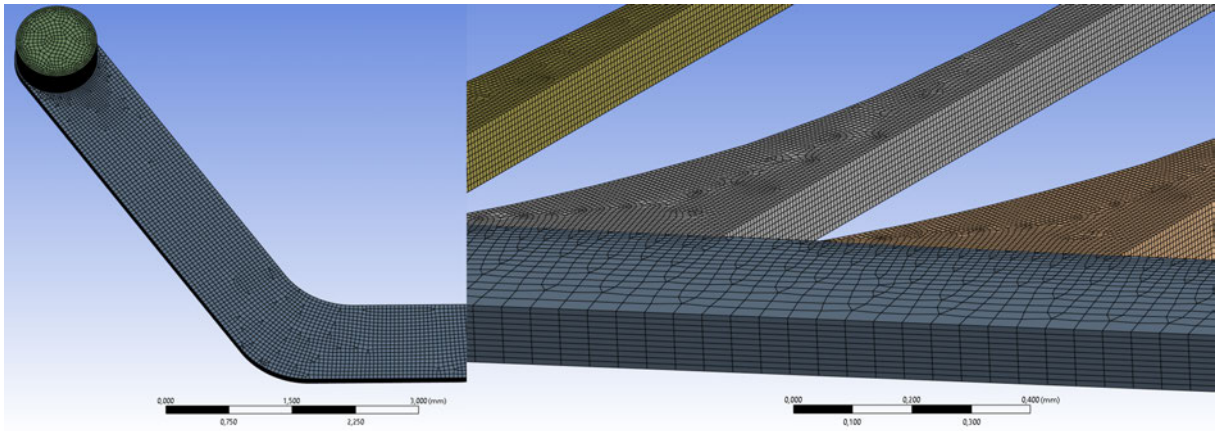


Figure 32: Generated mesh at the inlet and along the inlet manifold.

The resulting friction velocity (u_τ) follows as:

$$u_\tau = \sqrt{\frac{\tau_w}{\rho}} = 0.29\,\mathrm{m/s} \tag{56}$$

which is then used to evaluate the dimensionless wall distance:

$$y^+ = \frac{y u_\tau \rho}{\mu} = 3.29 \tag{57}$$

with $\rho = 997.05\,\mathrm{kg/m^3}$ and $\mu = 8.9 \times 10^{-4}\,\mathrm{kg/(m\,s)}$, the density and dynamic viscosity of water [48]. The mean velocity in a microchannel, $u = 0.34\,\mathrm{m/s}$, resulting from the imposed volumetric flow rate (see chapter 4). $y = 1 \times 10^{-5}\,\mathrm{m}$ represents the first cell height at the microchannel wall.

After the same procedure the y^+ values for water and Novec7100 for different flow rates are calculated and illustrated in table 3. The y^+ values increase with increasing volumetric flow rate for both fluids, as expected due to the increasing wall shear stress. For Novec7100, the values are consistently higher than for water because of the different fluid properties. Overall, the values remain within an acceptable range, indicating a sufficiently fine mesh resolution of the near-wall region [22].

Table 3: y^+ in the microchannels for water and Novec7100 at different volumetric flow rates.

Volumetric flow rate [mL/min]	y^+_{water}	$y^+_{\mathrm{Novec7100}}$
5	2.33	3.57
10	3.29	5.05
20	4.66	7.14
30	5.70	8.74

5.1.3 Numerical Setup

In this subsection, the numerical setup and selected solver settings are described. Double precision is selected. Because a constant volumetric flow rate is set at the pump and no time dependent changes are expected, a steady solver is chosen. Based on the analytical model (see section 4.1), laminar flow is assumed to be the governing flow regime in the sample, hence the laminar viscous model is selected. Consequently, the Navier-Stokes equation is solved without any additional terms for turbulence [2]. The fluid properties are set for either water or Novec7100. The values used are named in the corresponding results. As boundary conditions a mass flow inlet and a pressure outlet (Gauge Pressure = 0 Pa) are used. The mass flow at the inlet has to be calculated with the continuity equation (see equation (2)) for each individual volumetric flow rate and coolant. At every wall *No Slip* conditions occur. The pressure-velocity coupling is realised using the

SIMPLE algorithm. Spatial discretisation is performed using second-order schemes for pressure and momentum in order to reduce numerical diffusion and improve solution accuracy. All remaining parameters are kept as their default settings. Before starting the calculation a standard initialisation computed on the inlet is performed. A maximum of 500 iterations is specified, which was found to be sufficient to achieve stable convergence in most cases.

5.1.4 Convergence and Solution Stability

In figure 33 the plot of the residuals over the iterations for the simulation of water at $\dot{V} = 10\,\mathrm{mL/min}$ is shown. The residuals are decreasing linearly with an effective reduction of several orders of magnitude without oscillations. This behaviour is characteristic of a numerically stable and well-converged solution. In addition, other monitored values such as the pressure drop values or the outlet mass flow are evaluated to verify true convergence. The pressure drop between inlet and outlet (see figure 34) reaches a stable plateau after approximately 50 iterations, confirming that the solution values do not change significantly with further iterations. Moreover, the monitored outlet mass flow is compared with the prescribed inlet mass flow, to check for conservation of mass. For a volumetric flow rate of $\dot{V} = 10\,\mathrm{mL/min}$ with the density of water at 20 °C, $\rho = 998.21\,\mathrm{kg/m^3}$ [48], the mass flow at the inlet is given by:

$$\dot{m} = \dot{V} \cdot \rho = 1.66 \times 10^{-4}\,\mathrm{kg/s}\,. \tag{58}$$

The monitored mass flow at the outlet is $\dot{m} = 1.66 \times 10^{-4}\,\mathrm{kg/s}$. Thereby, it can be confirmed that the conservation of mass is fulfilled.

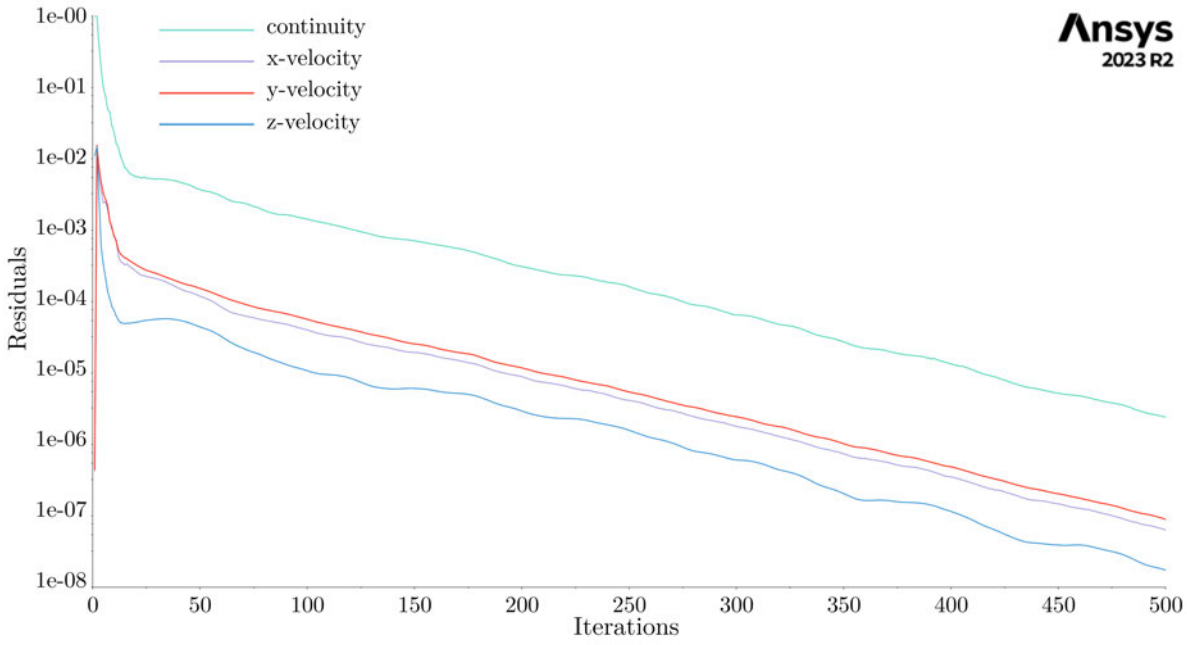


Figure 33: Convergence history of residuals for water at $\dot{V} = 10\,\mathrm{mL/min}$.

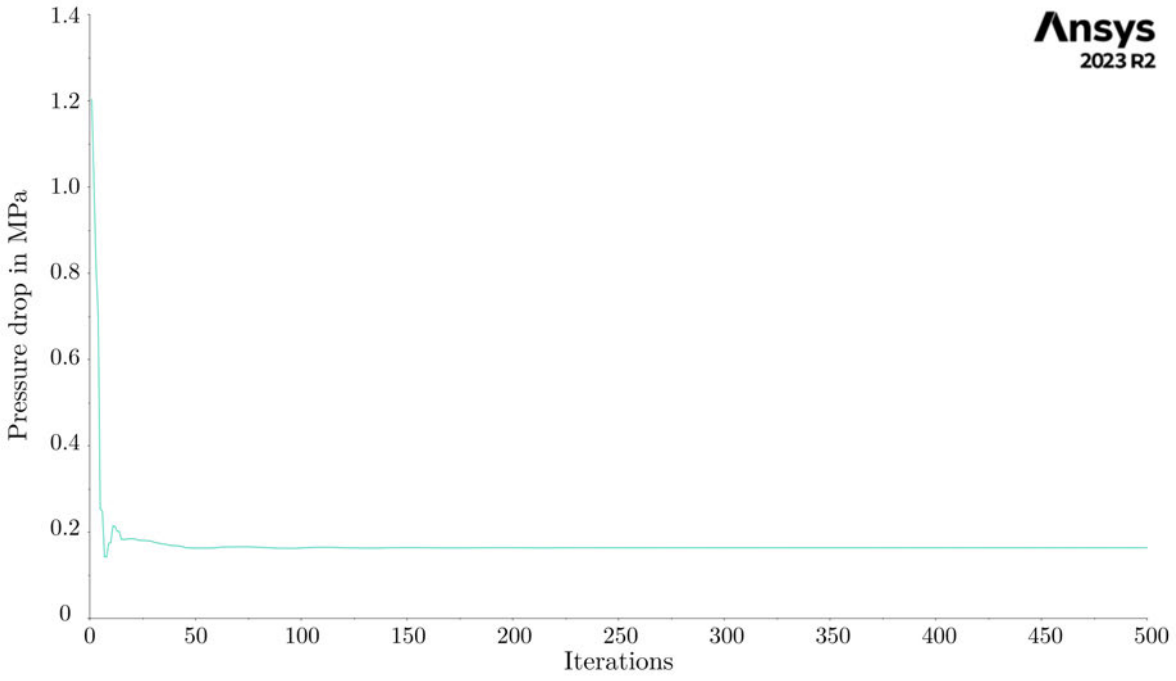


Figure 34: Convergence of the pressure drop for water at $\dot{V} = 10\,\mathrm{mL/min}$.

5.1.5 Simulation Results

This subsection will present the results of the simulation for the investigation of the total pressure drop and the flow behaviour based on streamlines. Furthermore, effects of the mesh size on the results will be evaluated here.

The total pressure drop of the system, measured by the pressure difference between the inlet surface and the outlet surface, is simulated for the volumetric flow rates from $\dot{V} = 5\,\mathrm{mL/min}$ to $\dot{V} = 30\,\mathrm{mL/min}$. Besides, the described mesh settings in section 5.1.2, two other mesh settings with larger element sizes in the microchannel inlets are simulated. The different size settings and the resulting total number of elements are listed in table 4. The simulated results for these different mesh sizes are illustrated in figure 35. In general, the pressure drop is steadily increasing. As the mesh becomes finer, the calculated pressure loss increases across the entire range of volumetric flow. Mesh 1 results in a lower pressure drop than mesh 2 and mesh 3. The curves of mesh 2 and mesh 3 are overlapping in the diagram. An evaluation of the exact values shows deviations smaller than 2 %. This indicates that the results for the presented mesh in section 5.1.2 are mesh-independent.

Table 4: Overview of the investigated meshes.

Mesh	Element size (MC inlet) [mm]	Total number of elements
Mesh 1	0.0250	420 798
Mesh 2	0.0125	2 438 262
Mesh 3	0.0100	4 434 500

In figure 36, the analytically calculated and numerically simulated pressure drop is shown for Novec7100 and water. The pressure drop increases for all curves as the volumetric flow rate increases. While the analytically calculated curves exhibit a strictly linear behaviour, the simulated results show slight deviations from linearity. Furthermore, the simulated values are consistently higher than the analytical values. Both effects can be attributed to the simplifications of the analytical model, which does not account for local pressure losses at the microchannel inlets and outlets. Moreover, the pressure drop of water is consistently higher than that of Novec7100, which is in agreement with the higher dynamic viscosity of water. Despite the simplifications in the analytical model, the qualitative trends are in good agreement with the numerical results, especially for lower flow rates. At higher flow rates the deviations increase, indicating that local pressure losses become increasingly dominant. In summary, the comparison demonstrates that local pressure losses play a significant role in the investigated geometry and must be considered for an accurate prediction of the total pressure drop.

Due to the fact, that computational limits were reached by a mesh size in all microchannel inlets of 0.01 mm, in the following the mesh size was only decreased for selected microchannels, where the biggest velocity differences in the manifold exist (see

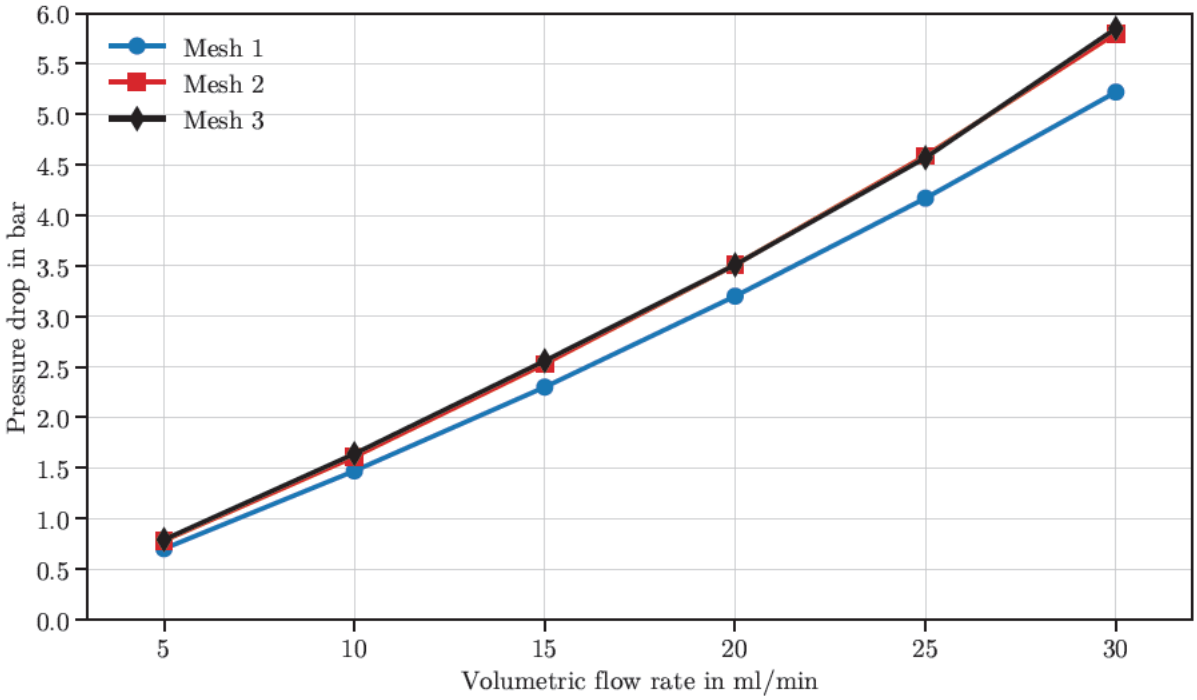


Figure 35: CFD results of the pressure drop as a function of volumetric flow rate for different meshes (water).

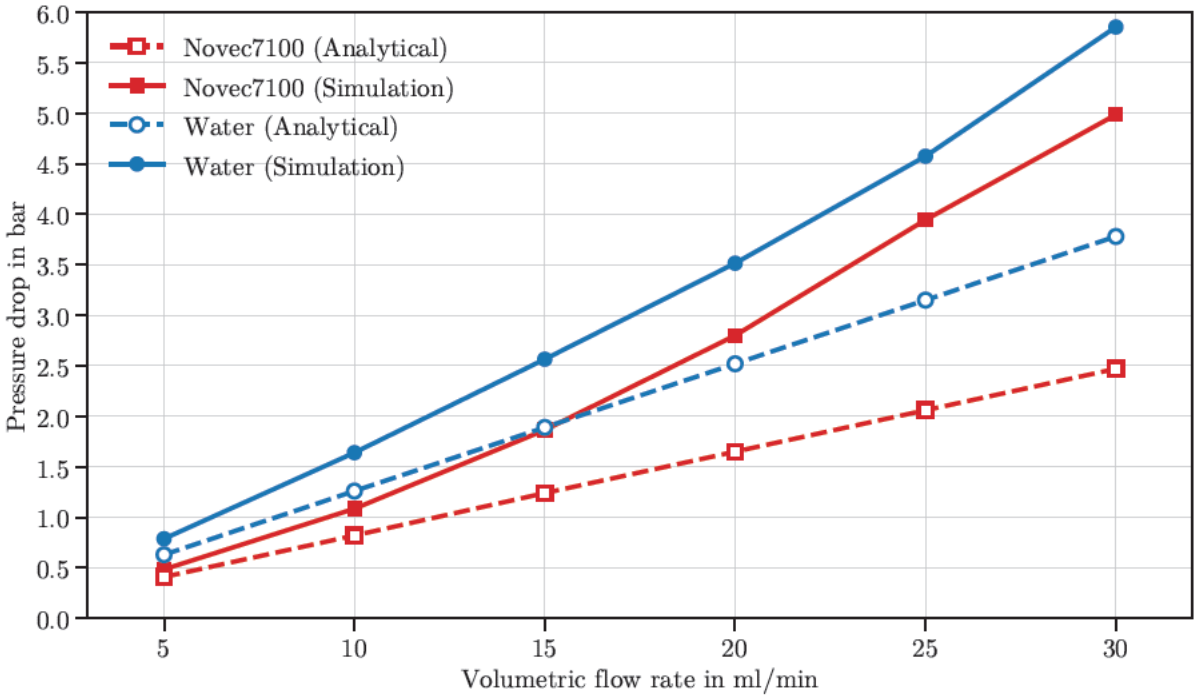


Figure 36: Pressure drop as a function of the volumetric flow rate for water and Novec7100, comparing analytical calculations and CFD results.

section 4.1). The mesh size was decreased in two steps to 0.005 mm and 0.003 mm. These settings are used to observe the streamlines at entry of the microchannels. The main objectives of this investigation are to analyse the variation of vortex intensity along the manifold, to assess the influence of the volumetric flow rate on vortex formation, and to determine the critical flow rate at which vortices first occur.

The results of this simulation for a flow rate of $\dot{V} = 5\,\mathrm{mL/min}$ are shown in figure 37. It is observable that not in every entry region a vortex occurs. The finest mesh shows vortices in microchannels 1, 2 and 28, whereas the roughest mesh only shows a vortex in microchannel 28. Furthermore, the size of the vortex is in the simulation with the highest resolution, the biggest. Therefore, the dependence of the mesh resolution on the representation of vortices in the microchannel entrance region can be shown. With a finer mesh, smaller and more complex flow structures can be resolved, leading to a more detailed representation of the local vortex formation. Moreover, it is recognisable that the appearance of the vortex differs depending on its position along the manifold.

Further simulations of the streamlines for different volumetric flow rates will be presented in section 6.3.2 in comparison with the experimental results of the fluorescence measurements.

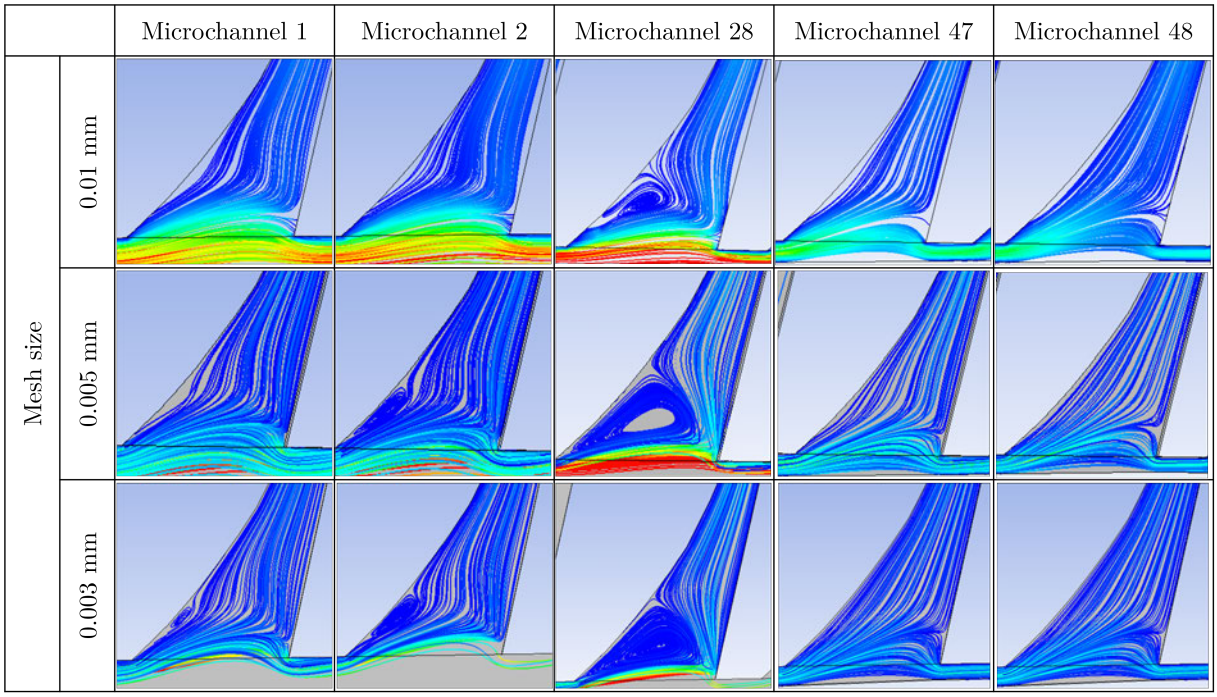


Figure 37: Influence of the mesh resolution on the streamlines at selected microchannel entries for water at $\dot{V} = 5\,\mathrm{mL/min}$.

Based on the previous results and the visible differences in the flow, the flow distribution through the microchannels is examined next. Therefore, the volumetric flow rate passing each microchannel is monitored in the simulation for water at a prescribed volumetric flow rate of $\dot{V} = 10\,\mathrm{mL/min}$. The results are illustrated in figure 38. Contrary to the assumption of homogeneous flow employed in the analytical calculation based on [23],

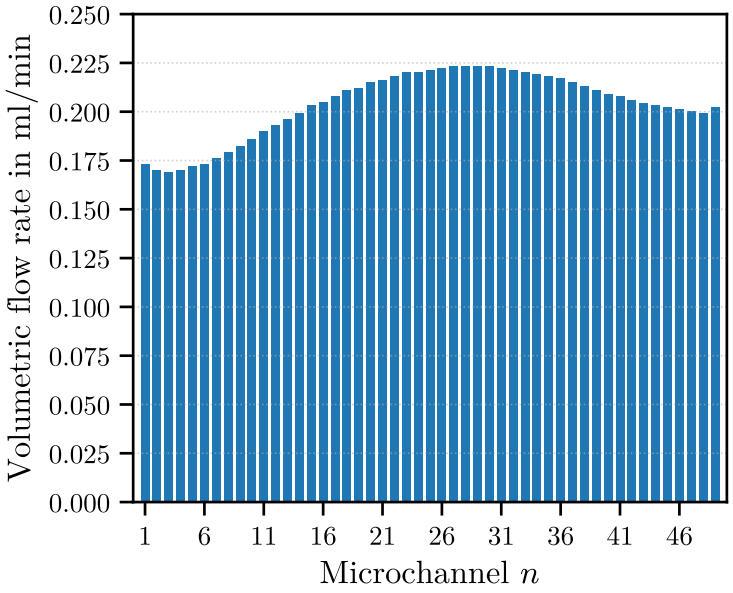


Figure 38: Distribution of volumetric flow through single microchannels for water at $\dot{V} = 10\,\mathrm{mL/min}$.

the simulation reveals significant differences in the volumetric flow distribution among the microchannels. The largest volumetric flow rates occur in the microchannels located in the middle of the layout, where the highest flow velocities in the manifold are observed and the biggest vortices occur. In contrast, the smallest volumetric flow rates are found in the first microchannels. Towards the rear of the layout, the volumetric flow rate decreases again but remains slightly higher than in the initial microchannels.

To quantify the observed maldistribution, a statistical evaluation of the flow distribution is performed using common statistical measures. The mean volumetric flow rate for the microchannels is calculated with:

$$\bar{\dot{V}} = \frac{1}{N} \sum_{i=1}^{N} \dot{V}_i = 0.204\,\mathrm{mL/min} \tag{59}$$

Multiplying the mean value by the number of channels gives the total volumetric flow rate, $\dot{V} = 9.996\,\mathrm{mL/min}$. The prescribed volumetric flow rate is achieved with a small deviation due to rounding errors. The Maldistribution Factor is defined as:

$$\mathrm{Maldistribution\,Factor} = \frac{\dot{V}_{\mathrm{max}} - \dot{V}_{\mathrm{min}}}{\bar{\dot{V}}} \cdot 100\,\% = 26\,\% \tag{60}$$

The result indicates that the microchannel with the highest volumetric flow receives 26 % more flow than the microchannel with the lowest volumetric flow rate. Small Maldistribution Factors are indicating a better flow distribution. It is also a common value in research on flow distribution in manifolds to quantify this characteristic [33].

5.2 Thermal Simulation

This section presents the extension of the fluidic simulation model to enable the investigation of the thermal behaviour of the system. In addition, the convergence behaviour and solution stability are evaluated. Finally, the simulation results are presented and discussed.

5.2.1 Extension of the Flow Model to Thermal Simulation

The thermal simulation is based on the fluid domain presented in section 5.1. The general geometric setup and the mesh settings of the fluid domain remain unchanged compared to the fluidic simulation. For the thermal simulation the wafer with the embedded microchannels and the wafer which is sealing the microchannel structure are added as solid domains. The resulting assembly with three domains is shown in figure 39.

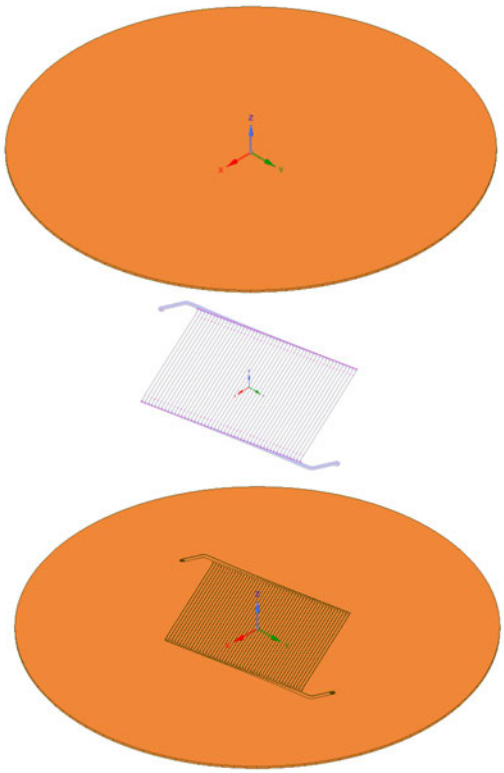


Figure 39: Exploded view of the domains used for the thermal simulation.

The mesh for both wafers was set by defining a body size of 0.2 mm. Due to computational limitations, it is not feasible to create a conformal mesh between the fluid and solid domains. Therefore, predefined contact regions between the domains are introduced to establish mesh interfaces, which allow the thermal coupling and heat transfer across all domains. In addition, several named selections are defined to apply the thermal boundary conditions. These include the inlet and outlet surfaces of the fluid domain and the bottom surface of the wafer where the experimental heat load is applied. All other

walls are defined as adiabatic. The thermal boundary conditions and the corresponding input parameters are shown in table 5.

Table 5: Thermal boundary conditions used in the simulations.

Named Selection	Boundary Condition	Input Parameters
Inlet	Mass flow inlet	$\dot{m}$ [kg/s], T_{in} [K]
Outlet	Pressure outlet	Default
Wafer surface (bottom)	Heat flux	$\dot{q}''$ [W/m^2]

To simulate the convective heat transfer between the solid and fluid, the energy equation is activated in the solver setup. As viscous model, the laminar flow option is retained. Furthermore, temperature-dependent fluid properties are implemented. For this purpose, experimental data for HFE-7100 (commercial name Novec7100) reported by [36] are used. The measured property values are implemented in the material definition using piecewise linear interpolation based on determined values at different temperatures. The temperature-dependent properties include density, dynamic viscosity, specific heat capacity, and thermal conductivity. The thermophysical properties of the solid materials are taken from literature and assumed to be constant throughout the simulation (table 6).

Table 6: Thermophysical properties of the solid materials used in the simulations [13, 17].

Material	ρ [kg/m^3]	c_{p} [J/(kg K)]	k [W/(m K)]
Silicon	2329	700	148
Pyrex	2230	753	1.13

5.2.2 Convergence and Solution Stability

In this subsection the convergence and solution stability for several values are evaluated. Figure 40 shows the progression of the residuals. The residuals decrease rapidly during the first iterations and reach a stable level after approximately 500 iterations. The x-, y-, and z-velocity residuals (blue, red, purple) reach a plateau at 10^{-6}, the energy residual (orange) drops to approximately 10^{-10} and the continuity residual (green) stabilizes around 10^{-5}. Therefore, the solution can be considered as numerically converged.

In figure 41 the development of the fluid temperature at the outlet is monitored. After around 500 iterations it reaches a stable value at slightly less than 294 K, which is used in the following evaluation of the energy conservation.

To evaluate the energy consistency of the simulation, the prescribed heater power ($\dot{Q}_{\text{total}} = 2.50\,\text{W}$) was compared with the heat transported by the fluid calculated from the

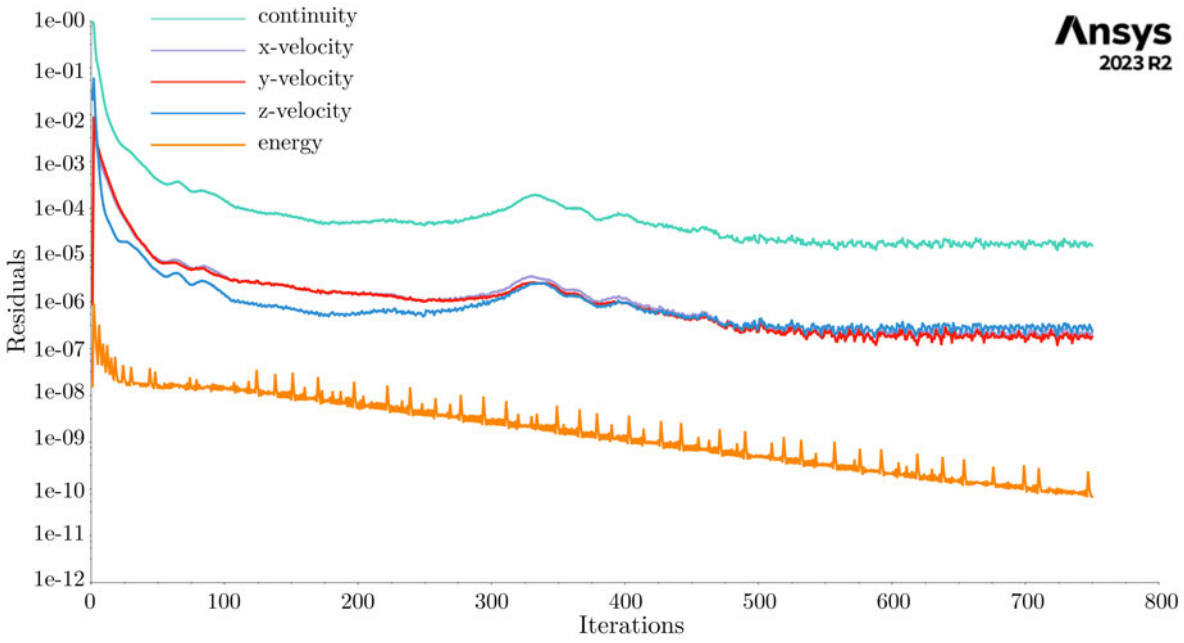


Figure 40: Convergence history of residuals for the thermal simulation at $\dot{V} = 10\,\mathrm{mL/min}$ and $T_{\mathrm{in}} = 285.15\,\mathrm{K}$.

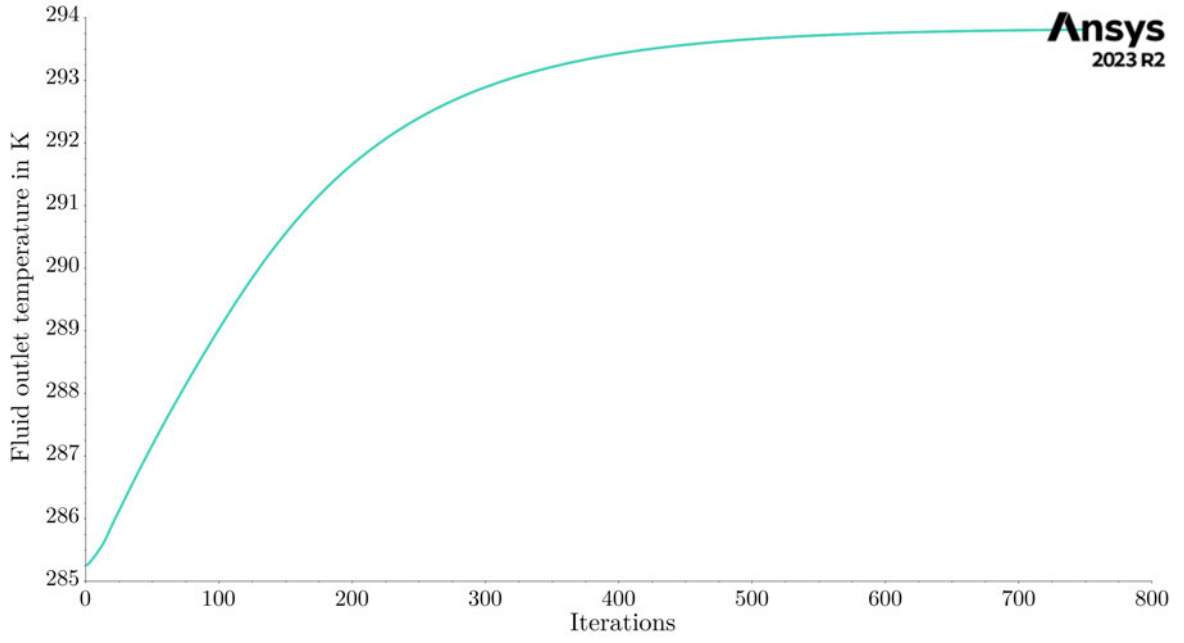


Figure 41: Convergence of the fluid outlet temperature for the thermal simulation at $\dot{V} = 10\,\mathrm{mL/min}$ and $T_{\mathrm{in}} = 285.15\,\mathrm{K}$.

mass flow rate and the temperature increase between inlet and outlet (see equation (14)), resulting in:

$$\dot{Q}_{\text{fluid}} = \dot{m} c_{\text{p}} (T_{\text{out}} - T_{\text{in}}) = 2.55\,\text{W} \tag{61}$$

The calculation is based on a mass flow rate of $\dot{m} = 2.53 \times 10^{-4}\,\text{kg/s}$, a specific heat capacity $c_{\text{p}}(T = 290\,\text{K}) = 1165\,\text{J/(kg K)}$, an outlet temperature of $T_{\text{out}} = 293.81\,\text{K}$, and an inlet temperature of $T_{\text{in}} = 285.15\,\text{K}$. A comparison of $\dot{Q}_{\text{total}}$ and $\dot{Q}_{\text{fluid}}$ shows a deviation of 2 %. This indicates that conservation of energy is sufficiently fulfilled. The fluid properties shown in section 5.1.4 deliver also converged solutions for the thermal simulation.

5.2.3 Simulation Results

In this subsection the results of the CFD simulation with a focus on the wall temperature in the microchannels are presented and compared with the results of the analytical model. The surface temperature distribution of the wafer is discussed together with the IR measurement results in a later section.

The boundary conditions for the presented results are based on the experiments shown later. In these experiments, fluid temperatures of approximately $T_{\text{in}} = 285.15\,\text{K}$ for $\dot{V} = 10\,\text{mL/min}$ and $T_{\text{in}} = 278.15\,\text{K}$ for $\dot{V} = 30\,\text{mL/min}$ were measured at the flowmeter upstream of the microchannel sample. To enable a comparison between the analytical model and the CFD simulation, the mass flow through each channel ($\dot{m}_{\text{c}}$) and the fluid temperature were extracted from the simulation. The fluid temperature was measured as a mass-weighted-average across the cross-section of the microchannels at a position 2 mm downstream of the channel entry, to avoid an influence of the observed vortices on the temperature value (see figure 45). Based on these values, the inlet temperature at $x = 0$ was determined by using equation (43). The obtained inlet temperature was used as initial temperature ($T_{\text{m,i}}$) to calculate the wall temperature development along each microchannel using equation (45). In figure 42, the values used as input for the analytical calculation are shown for each microchannel. As already seen in the fluidic simulation it is observable that there is no homogeneous mass flow through the microchannels. Contrary to the consideration made in section 4.2.3 that the temperature along the manifold, here represented by $T_{\text{m,i}}$, increases continuously, the simulation results show a different behaviour. The temperature first decreases. A deeper investigation on this unexpected behaviour will be presented after discussing the results of the temperature distribution.

The colour maps obtained from the analytical model are compared with the contour plots from the CFD simulation, both showing the wall temperature T_{s} of the microchannel wall closest to the wafer top surface. For $\dot{V} = 10\,\text{mL/min}$ (see figure 43), both methods show a good qualitative agreement regarding the temperature distribution and the shape of the isotherms. For $\dot{V} = 30\,\text{mL/min}$ (see figure 44), deviations between the analytical

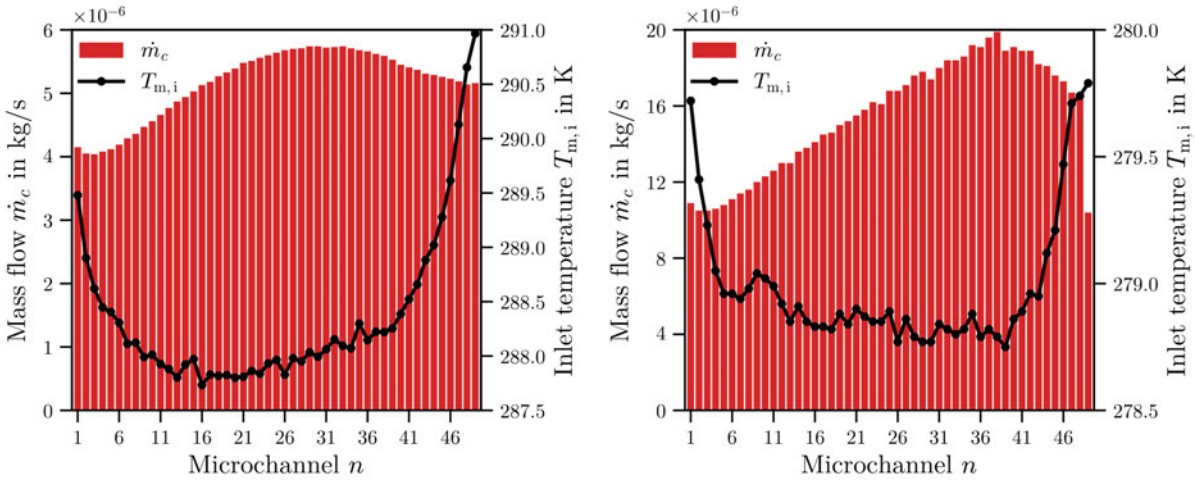


Figure 42: Comparison of inlet conditions for Novec7100 at $\dot{V} = 10\,\mathrm{mL/min}$ with $T_{\mathrm{in}} = 285.15\,\mathrm{K}$ (left) and $\dot{V} = 30\,\mathrm{mL/min}$ with $T_{\mathrm{in}} = 278.15\,\mathrm{K}$ (right).

approach and the CFD simulation are more pronounced. The mass flow distribution (see figure 42) is clearly reflected in the profile of the isotherms of the analytical model. In contrast, the simulation results exhibit a more uniform temperature distribution. One possible explanation is the heat transfer between adjacent microchannels, which is captured in the simulation but neglected in the analytical model, leading to a smoothing of temperature gradients across neighbouring microchannels.

Overall, the results indicate that the analytical model captures the main qualitative trends, particularly at lower flow rates. It shows the impact of $\dot{m}_{\mathrm{c}}$ and $T_{\mathrm{m,i}}$ on the thermal behaviour. Based on this, the analytical model can be used for a fast pre-estimation of a combination of these two parameters to obtain a homogeneous temperature distribution. Nevertheless, the analytical model overestimates the temperature increase along the microchannels. The deviations can be attributed to the simplifying assumptions of the analytical model, which, among other things neglects the interaction between neighbouring channels as well as heat conduction with the surrounding solid.

The unexpected behaviour of $T_{\mathrm{m,i}}$ can be explained by analysing the contour plots of the fluid velocity and temperature, shown in figure 45. The bend in the inlet manifold causes pronounced local flow effects. In the inner region downstream the bend, the fluid velocity decreases significantly, leading to a local temperature rise. This behaviour affects the inlet conditions of the downstream microchannels and explains why the inlet temperature of the first microchannels is higher. The influence of this effect with increasing volumetric flow rates is illustrated by comparing the inlet conditions at the microchannel entries for $\dot{V} = 10\,\mathrm{mL/min}$ and $\dot{V} = 30\,\mathrm{mL/min}$ in figure 42. It is observed that the initial temperature $T_{\mathrm{m,i}}$ decreases for $\dot{V} = 30\,\mathrm{mL/min}$ until microchannel 41 before increasing rapidly. For $\dot{V} = 10\,\mathrm{mL/min}$, $T_{\mathrm{m,i}}$ decreases until microchannel 16, after which it first increases slowly and then more rapidly. Moreover, a shift of the maximum mass flow values to the microchannels located at end of the manifold is evident.

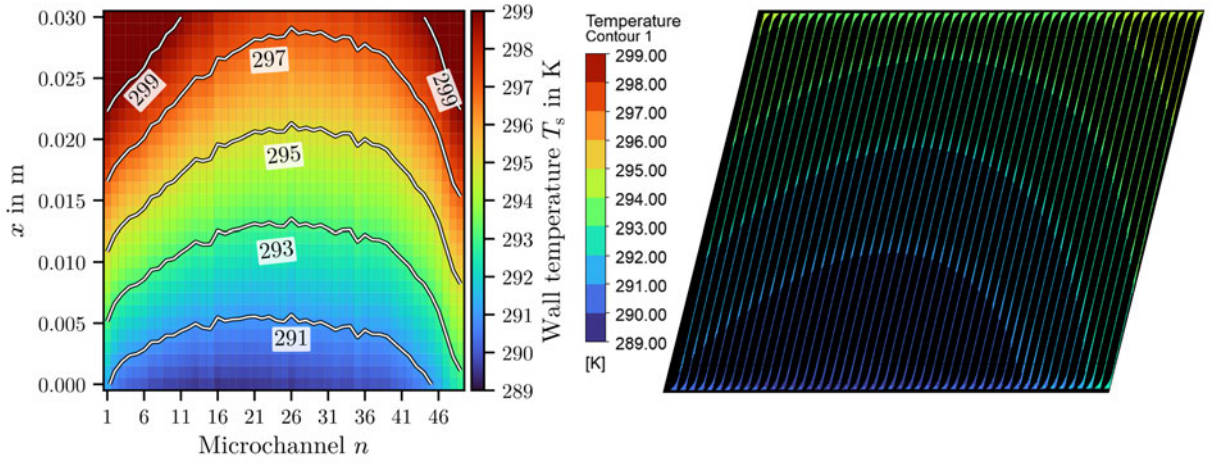


Figure 43: Comparison of the wall temperature T_s predicted by the analytical model (left) and obtained from the CFD simulation (right) at $\dot{V} = 10\,\mathrm{mL/min}$ with $T_{in} = 285.15\,\mathrm{K}$.

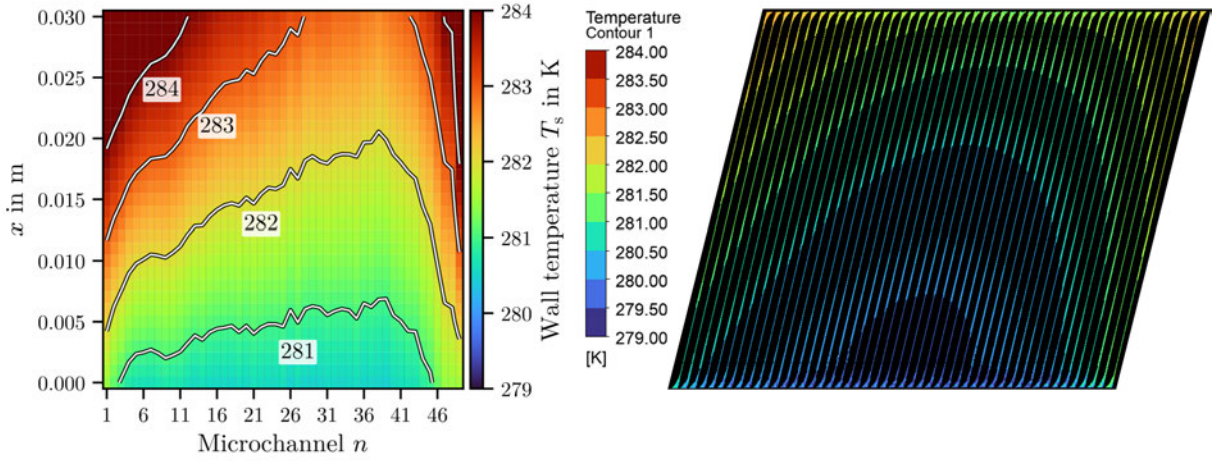


Figure 44: Comparison of the wall temperature T_s predicted by the analytical model (left) and obtained from the CFD simulation (right) at $\dot{V} = 30\,\mathrm{mL/min}$ with $T_{in} = 278.15\,\mathrm{K}$.

While the contour plots are shown only for $\dot{V} = 10\,\mathrm{mL/min}$ in figure 45, the same flow effects are observable for $\dot{V} = 30\,\mathrm{mL/min}$, where the affected region extends further downstream.

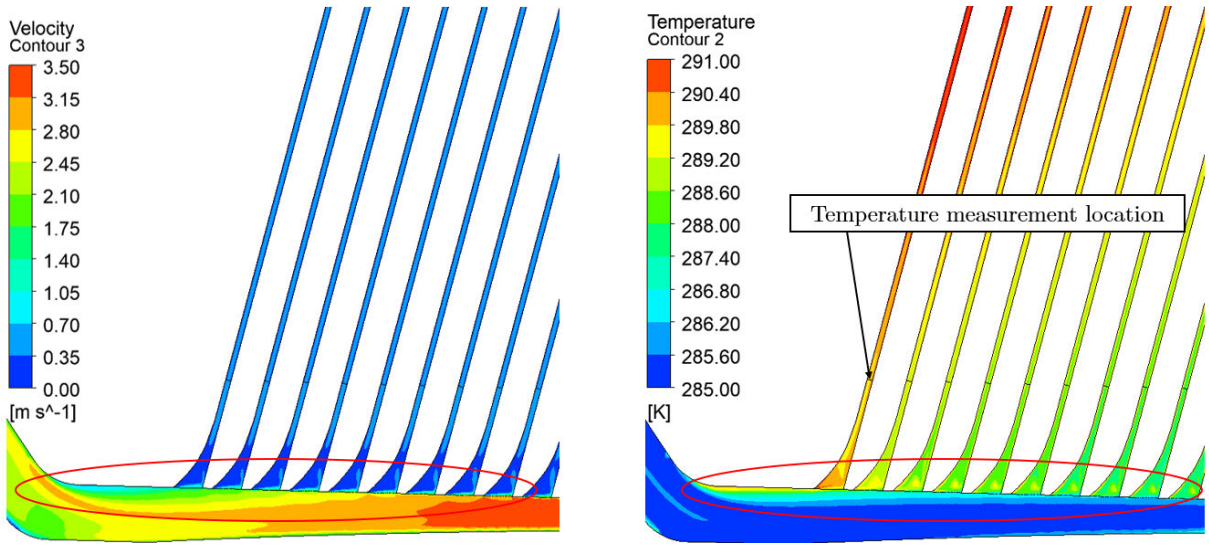


Figure 45: Contour plots for fluid velocity and temperature in the manifold at $\dot{V} = 10\,\mathrm{mL/min}$ with $T_{\mathrm{in}} = 285.15\,\mathrm{K}$, local flow effects in the manifold marked in red.

6 Experimentation

This chapter presents the experimental investigations carried out in this work. It begins with the necessary recommissioning steps, including the bonding of the NanoPorts and the setup of the measurement system architecture. First, the results from fluid-dynamic investigations are presented. Subsequently, the thermal investigations are outlined.

All experiments were conducted using the same anodically bonded microchannel sample consisting of a Pyrex cover and a silicon wafer. The investigated sample is purely for testing purposes and does not fulfil any functional application. The results are compared with simulation data to validate the CFD model and assess its potential for future applications in design optimisation. The objective of this chapter is to evaluate the experimental results, characterise the investigated microchannel sample, and assess the agreement with CFD predictions.

6.1 Recommissioning of the Experimental Setup

Since the experimental setup had not been used for an extended time, several hardware and software components were either missing, outdated, or no longer fully compatible. For example, the connection between the computer and the measurement devices had to be re-established. Furthermore, an alternative bonding method had to be found and validated, as the previously used adhesive rings are no longer available. This section outlines the steps required to recommission the setup and ensure stable, convenient and reliable measurements.

6.1.1 Measurement System Architecture

In section 2.2, the measurement devices used in the experimental setup were introduced. This section focuses on the connection of these devices with the computer. The data acquisition architecture was designed and implemented to ensure an efficient transfer and processing of measurement data. In figure 46 the schematic structure of the data flow from the measurement devices to the computer is visualised.

The output signal of the pressure transducer is a voltage from 0 V to 5 V, depending on the pressure in the system. The correlation between voltage and pressure is linear. The signal is fed into the analog input of an Arduino Uno [4]. Inside the Arduino, an Analog-Digital-Converter (ADC) converts the analog voltage signal into a 10 bit digital

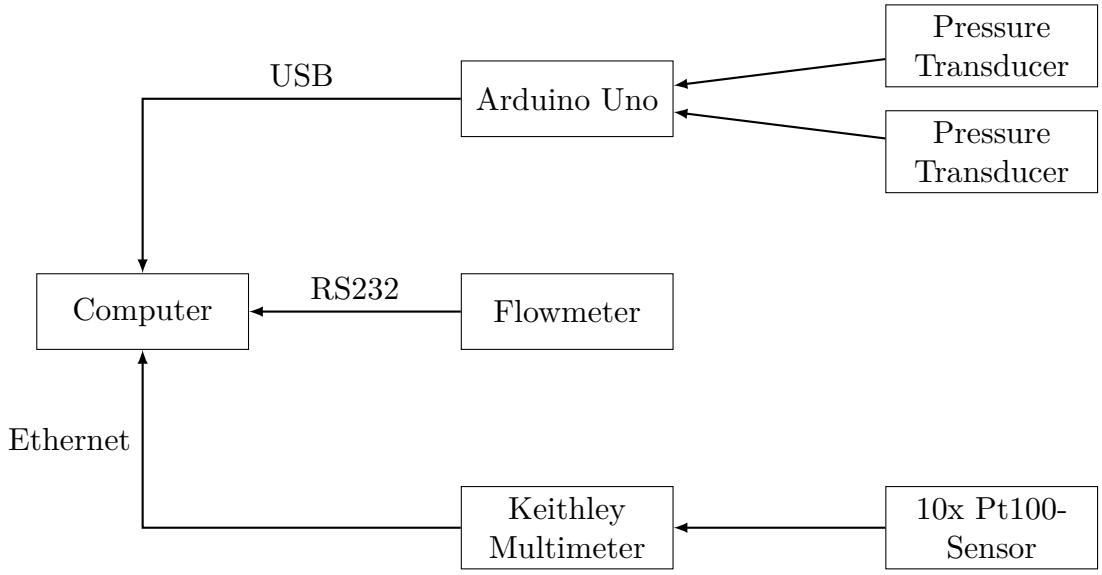


Figure 46: Experimental measurement system architecture.

value (ADC-Value). Thus, a voltage of 0 V corresponds to a digital value of 0 and 5 V corresponds to 1023. The relationship between the ADC-Value and voltage is given by:

$$U = \text{ADC-Value} \cdot \frac{5\,\text{V}}{1023} \tag{62}$$

The voltage is then calculated in the code of the Arduino and finally converted to the pressure value using the equation:

$$p = U \cdot \frac{100\,\text{bar}}{5\,\text{V}} \tag{63}$$

The script used for the pressure measurements is shown in section A.1.

The flowmeter is connected to the computer via an RS232-to-USB adapter. In addition, the software FlowDDE from Bronkhorst is necessary to establish the communication interface between Windows and the flowmeter [8]. Live tracking of the coolant properties can be performed by using FlowPlot or FlowView after the communication is set up between the computer and the flowmeter in FlowDDE [9, 10]. In order to store and process the measurement data afterwards a Python script was developed, which records and stores the measurement data (Volumetric Flow Rate, Density, Temperature) with a timestamp in a .CSV file (see section A.2).

To measure the surface temperature on the samples, ten 4-wired Pt100 sensors are used to minimise lead resistance effects. The cables from the Pt100s are soldered to a 50-pin D-Sub connector which is connected to a 50-wire ribbon cable. The sensor cables have to be connected to two paired channels on the multiplexer module (Keithley 7700 [32]), corresponding to the four-wire measurement configuration. After inserting the multiplexer module to the Keithley 2701 multimeter [42], it is possible to switch

through the channels and see the measured voltage for each sensor on the display of the multimeter.

The Pt100 changes its resistance in relation to the temperature. At 0 °C the nominal resistance is 100 Ω. The resistance increases with a rising temperature. This relationship can be described with the following equation [18]:

$$R_t = 100\,\Omega(1 + 3.9083 \times 10^{-3}/°\mathrm{C} \cdot t - 5.775 \times 10^{-7}/°\mathrm{C}^2 \cdot t^2) \tag{64}$$

Since the resistance is measured, the equation must be rearranged to obtain the temperature:

$$t = \frac{-A + \sqrt{A^2 - 4B\left(1 - \frac{R_t}{100\,\Omega}\right)}}{2B} \tag{65}$$

with $A = 3.9083 \times 10^{-3}/°\mathrm{C}$ and $B = -5.775 \times 10^{-7}/°\mathrm{C}^2$. This equation is implemented in a Python script. The script enables the communication via Ethernet between computer and multimeter to acquire the resistance measurement values on the computer. These values are then converted into temperature data and saved in a .CSV file for further analysis. In addition, a live plot is generated to monitor when thermal equilibrium is reached. The script is shown in section A.3.

6.1.2 NanoPort Bonding

Due to the discontinuation of the previously used adhesive rings for the NanoPorts, an alternative bonding solution was required. According to the manufacturer, *Loctite Glass Glue* is recommended, with a specified failure pressure of 7 bar [27]. However, both simulations and preliminary considerations indicated that significantly higher pressures can occur in the investigated system, particularly at high volumetric flow rates. For reliable operation at flow rates up to 50 mL/min, a bonding strength corresponding to approximately 20 bar is required. Therefore, several alternative adhesives were evaluated with regard to their pressure resistance and suitability for the present application.

The bonding strength was examined by attaching a NanoPort to a silicon wafer using the respective adhesive. The bonded sample was integrated into the coolant circuit. The NanoPort attached with the adhesive under investigation served as the coolant inlet and was therefore directly exposed to the system pressure. The second NanoPort, acting as the outlet, was mounted using the original adhesive ring and was not part of the evaluation. The volumetric flow rate was subsequently increased until failure of the tested bond occurred. In addition to the maximum sustainable pressure, handling properties and failure characteristics were considered.

To ensure accurate positioning of the NanoPort relative to the inlet at the wafer, a bonding tool was designed and manufactured (see figure 47). The tool enables optical alignment of the NanoPort with the inlet opening on the wafer surface prior to bonding. After alignment and applying adhesive on the NanoPort, the NanoPort is pressed onto

the wafer by tightening a knurled screw, which applies a controlled vertical contact force during adhesive curing.

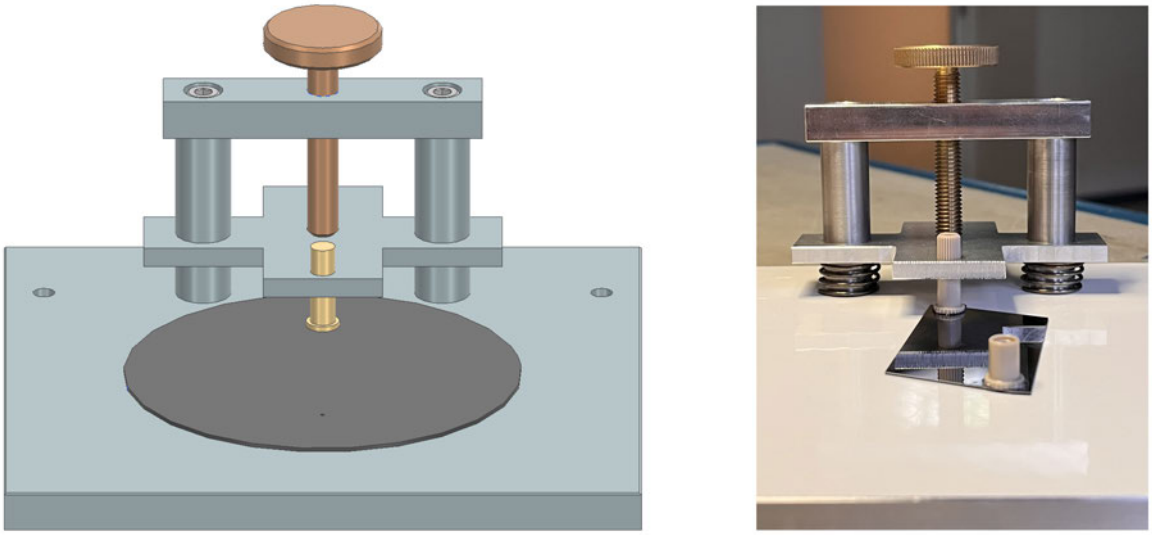


Figure 47: Bonding tool shown as CAD design (left) and actual assembly (right).

The first tested adhesive is *Loctite Glass Glue*, as recommended by the manufacturer of the NanoPorts. According to the data sheet, the adhesive exhibits a tensile strength of $1.5\,\mathrm{N/mm^2}$ to $2.5\,\mathrm{N/mm^2}$ [34]. The low viscosity combined with the fast curing rate of the adhesive results in limited handling time and increased difficulty during processing. Experimentally, the bonded NanoPort withstood a volumetric flow rate of 45 mL/min, corresponding to a pressure of approximately 12 bar. Inspection of the detached interface revealed almost no adhesive on the NanoPort (see figure 48), indicating adhesion failure at the interface between adhesive and PEEK surface. Hence, the effective bonding strength was limited by adhesion rather than by the strength of the adhesive.

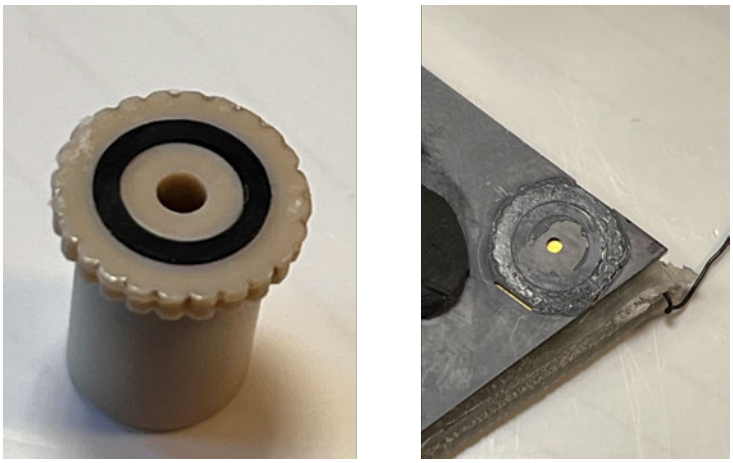


Figure 48: Detached NanoPort with *Loctite Glas Glue* at the wafer surface.

In a previous study [37], a two-component epoxy adhesive was used for bonding the NanoPorts to a silicon surface. The specified bonding strength for aluminium is

17 N/mm^2, although this value is not transferable to the present material combination. This adhesive exhibits higher viscosity and a longer handling time [45], which reduces the likelihood of processing errors. The test showed that the two-component adhesive withstands a volumetric flow rate of 30 mL/min and 8 bar. As no adhesive residues were observed on the wafer surface (see figure 49), the detachment can be classified as an adhesion failure at the interface between the silicon wafer and the adhesive.

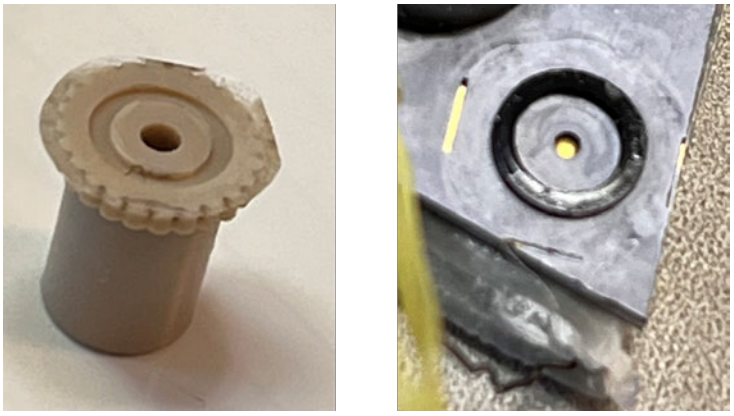


Figure 49: Detached NanoPort with 2-component epoxy adhesive at the NanoPort.

Following consultation with adhesive manufacturers, a silane-modified polymer adhesive (*UHU Max Repair Power*) was selected for further evaluation. The specified bonding strength is 8 N/mm^2 and the material is suitable for plastics and glass, which makes it compatible with the PEEK NanoPort and the silicon wafer. The viscosity and handling time are comparable to those of the 2-component epoxy adhesive, which facilitates easy application [44]. In the conducted tests, the bonded NanoPort withstood a volumetric flow rate of 50 mL/min, corresponding to a pressure of 17 bar, without detachment. No failure occurred within the investigated operating range. Further increase of the volumetric flow rate was not pursued, as higher pressures would risk mechanical damage to the silicon wafer. Therefore, this adhesive fulfills the pressure requirements and was selected for all subsequent experiments.

In later experiments, leakage at the adhesive interface was occasionally observed at pressures of approximately 8 bar. By applying a second adhesive layer, all experiments could be conducted as planned without further failure. The wafer used in the experiment has a polished surface, which may have contributed to reduced adhesion strength. This shows, further investigation is required to ensure a reliable and durable connection between the wafer and the NanoPort.

6.2 Flow: Pressure Drop Measurements

Initially, the pressure drop was measured without an integrated sample in the coolant circuit in order to determine the hydraulic resistance of the connecting pipes. The results showed that their contribution to the overall pressure drop is negligible.

The experimentally measured pressure drop and the corresponding simulation results for Novec7100 and water are shown in figure 50. For both fluids, the pressure drop was measured for volumetric flow rates in the range from $\dot{V} = 5\,\mathrm{mL/min}$ to $30\,\mathrm{mL/min}$. The values for water were only measured up to $20\,\mathrm{mL/min}$, because the measurements were performed while the fluorescence measurements.

At identical volumetric flow rates, water exhibits a higher pressure drop than Novec7100. This behaviour is observed in the experimental measurements and the simulation results. Overall, the simulation reproduces the trend of the experimental data well. For water, the simulated pressure drop is slightly higher than the experimentally measured values. In contrast, for Novec7100 the simulation underpredicts the pressure drop at higher volumetric flow rates. The deviation becomes more pronounced with increasing flow rate. Nevertheless, for the investigated volumetric flow rate range, the deviations remain relatively small and the simulation captures the general behaviour of the pressure drop with increasing flow rate. Comparing the experimental pressure values for Novec7100 with those shown in the previous work (see figure 5), it can be observed that the measured pressure drops are of the same order of magnitude. This indicates that the hydrodynamic performance has not improved despite the design modifications. Achieving comparable pressure drops with a reduced microchannel length suggests a deterioration in hydrodynamic performance, as similar pressure losses occur over a shorter flow path.

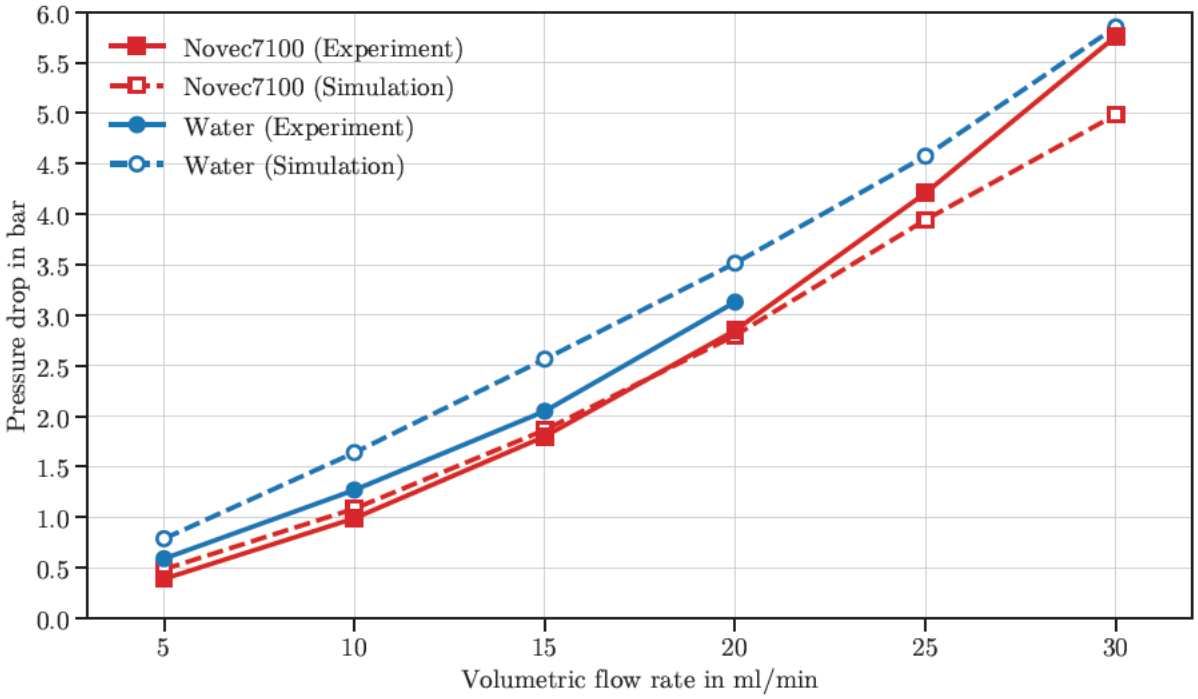


Figure 50: Comparison of experimentally measured and simulated pressure drop as a function of volumetric flow rate for water and Novec7100.

6.3 Flow: Fluorescence Measurements

The fluorescence measurements were performed in the Nano-Opto-Fluidics Laboratory at the HARBOR institute of the University of Hamburg, who are focusing on studying single (bio)molecules with lab-on-a-chip devices, which also includes flow through nano and microchannels [21].

These measurements are employed as a qualitative flow visualisation technique to validate the CFD-predicted flow structures. Two main objectives are investigated using fluorescence measurements. First, the confirmation of the simulation results that the formation of vortices changes with the position in the manifold. Secondly, the observation about how the design optimisation of the new prototype layout has changed the fluid behaviour.

6.3.1 Experimental Setup

For the fluorescence measurements a reduced test setup, just containing the coolant fluid circuit of the whole setup, was set up in the Nano-Opto-Fluidics Laboratory. In figure 51 the coolant circuit in front of the fluorescence microscope in the laboratory is shown. Furthermore, a mounting bracket was designed which fixes the sample at the microscope table, which is also imaged in figure 51. The bracket aligns the x- and y-axis of the

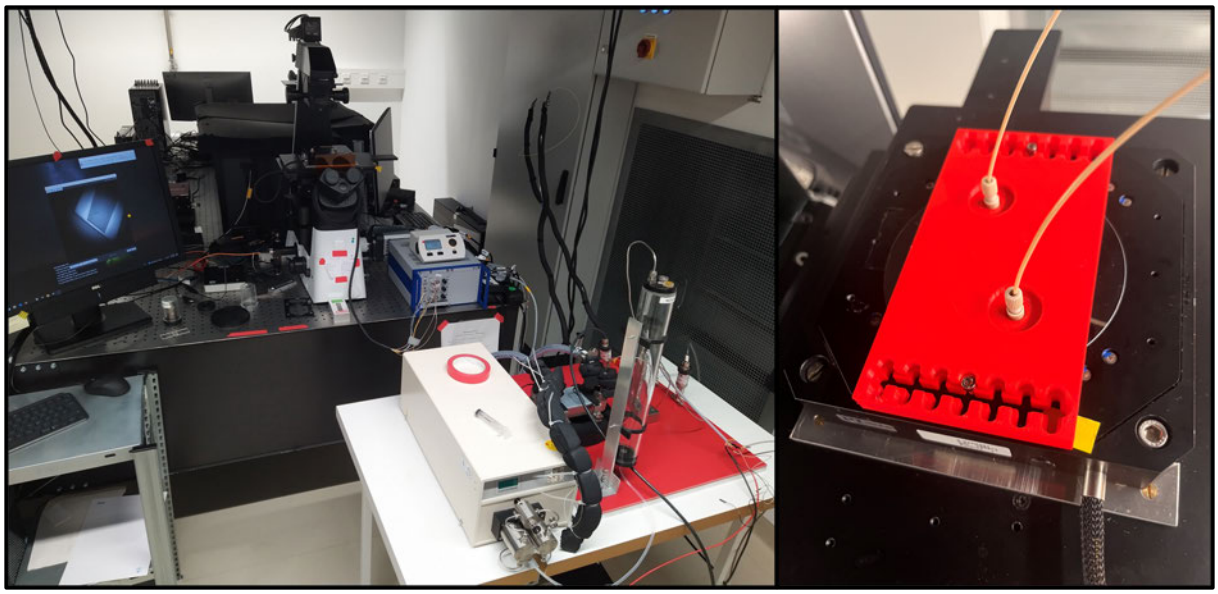


Figure 51: Test setup for the fluorescence measurements in the nanofluidics laboratory.

sample with the axis of the microscope, so that the entries of the microchannels are accurately positioned in the recordings. It also facilitates the positioning of the sample so that every microchannel inlet can be recorded, despite a small range of motion of the microscope table. The experiments are conducted using water, because the fluorescence tracer beads are only soluble in water and Novec7100 is immiscible with water, making its usage in this test series infeasible. The used microscope is a Nikon Eclipse Ti-2 confocal

microscope. In the experiment, the volumetric flow rate was increased in several steps up to $\dot{V} = 20\,\mathrm{mL/min}$. At higher flow rates the particles were so fast, that the microscope is not able to capture them probably, so that on the images no clear streamlines are recognisable. The flow behaviour is investigated in the same chosen microchannel inlets as in the simulation were (see section 5.1), where the highest differences due to different velocities in the manifold are expected.

6.3.2 Results

The experimental results, together with the corresponding CFD simulations, for all investigated volumetric flow rates are presented in figure 52 - figure 58. At $\dot{V} = 2\,\mathrm{mL/min}$, no formation of vortices is observable in any of the investigated microchannel entries. When the volumetric flow rate is increased to $\dot{V} = 3\,\mathrm{mL/min}$, the first vortex appears at the entry of microchannel 28. At $\dot{V} = 10\,\mathrm{mL/min}$, vortices are present at the entry of every microchannel. These observations demonstrate a clear dependence of vortex formation on the volumetric flow rate. With an increasing flow rate, the number of microchannels exhibiting vortex formation and the size of the vortices increase.

At higher volumetric flow rates, an additional experimental phenomenon is observed. Bubbles form at several microchannel entries, where they remain trapped and influence the flow (see figure 57 - Microchannel 48). The underlying mechanism is not further investigated in this work.

Furthermore, the experiments confirm that vortex formation is strongly dependent on the position along the inlet manifold. So, the first vortex occurs in the central region of the manifold, whereas at the beginning and the end of the manifold no vortex formation is observed. The observed behaviour originates from the velocity profile along the inlet manifold (see equation (33) and figure 23). Locally increased velocities enhance adverse pressure gradients at the microchannel entry region, promoting vortex formation. This separation mechanism subsequently leads to increased local pressure losses (see figure 27).

The comparison between CFD simulation and experimental results shows good qualitative agreement. The simulation slightly underestimates vortex formation. This is most notable in Microchannel 47 - Microchannel 49. The deviations are likely related to accumulated numerical errors near the downstream end of the manifold. But, the overall flow behaviour regarding the onset location and growth of vortices are well captured. In summary, the fluorescence measurements validate that the CFD model reliably reproduces the qualitative flow behaviour in the microchannel prototype, particularly with respect to flow rate dependence, onset location and vortex growth.

These results indicate that a direct comparison with the findings of the preceding work (section 2.3.2) is not feasible. The exact position of the observed microchannel entrance within the manifold is not specified in the previous study. As demonstrated above, the flow behaviour at the microchannel entrance is strongly position-dependent, which significantly influences vortex formation. In comparison to the experimental observations,

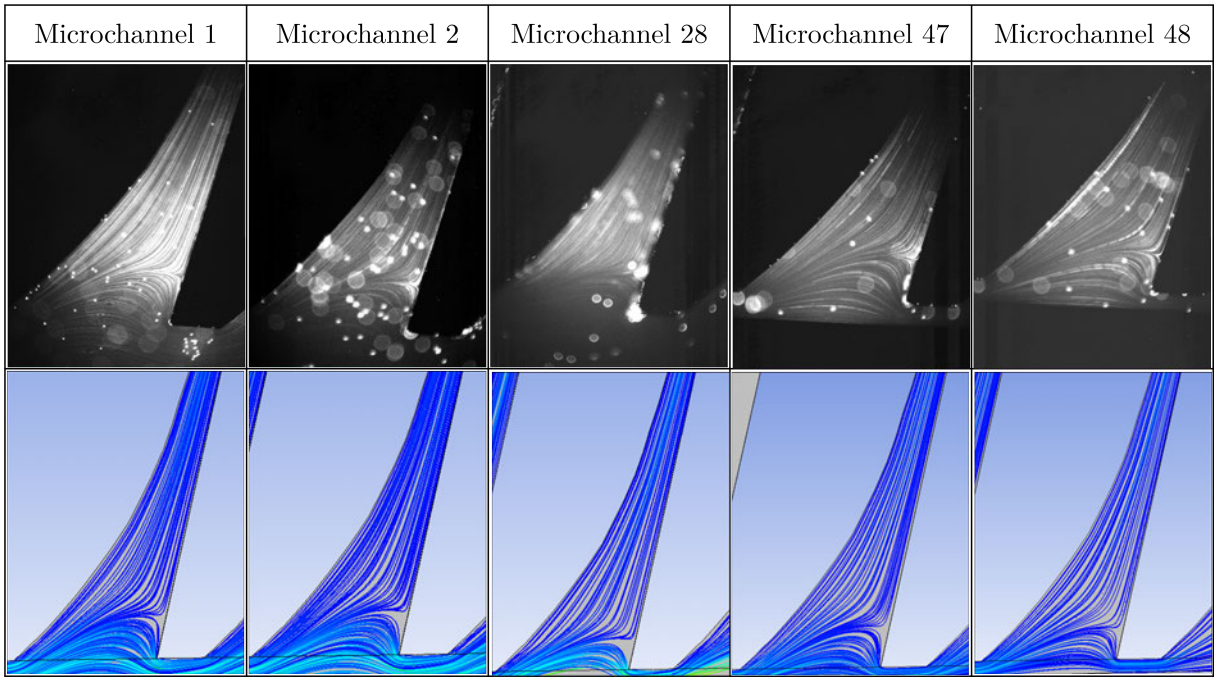


Figure 52: Comparison of fluorescence measurements and CFD results at selected microchannel entries for $\dot{V} = 2\,\mathrm{mL/min}$.

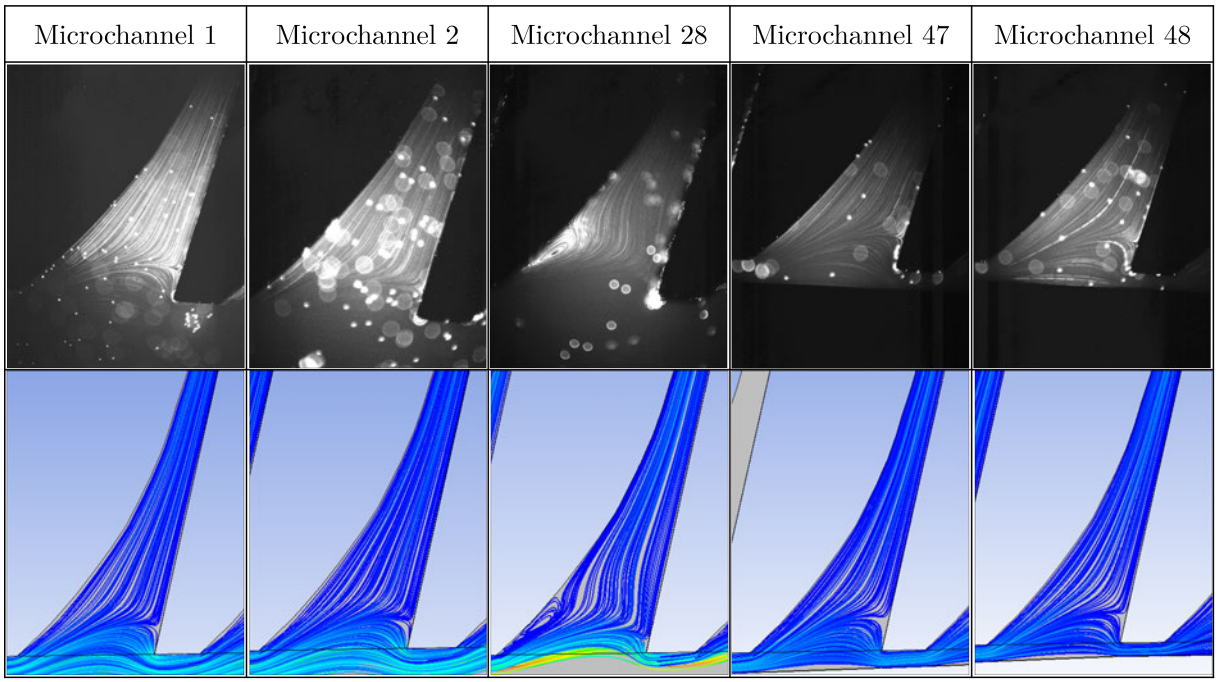


Figure 53: Comparison of fluorescence measurements and CFD results at selected microchannel entries for $\dot{V} = 3\,\mathrm{mL/min}$.

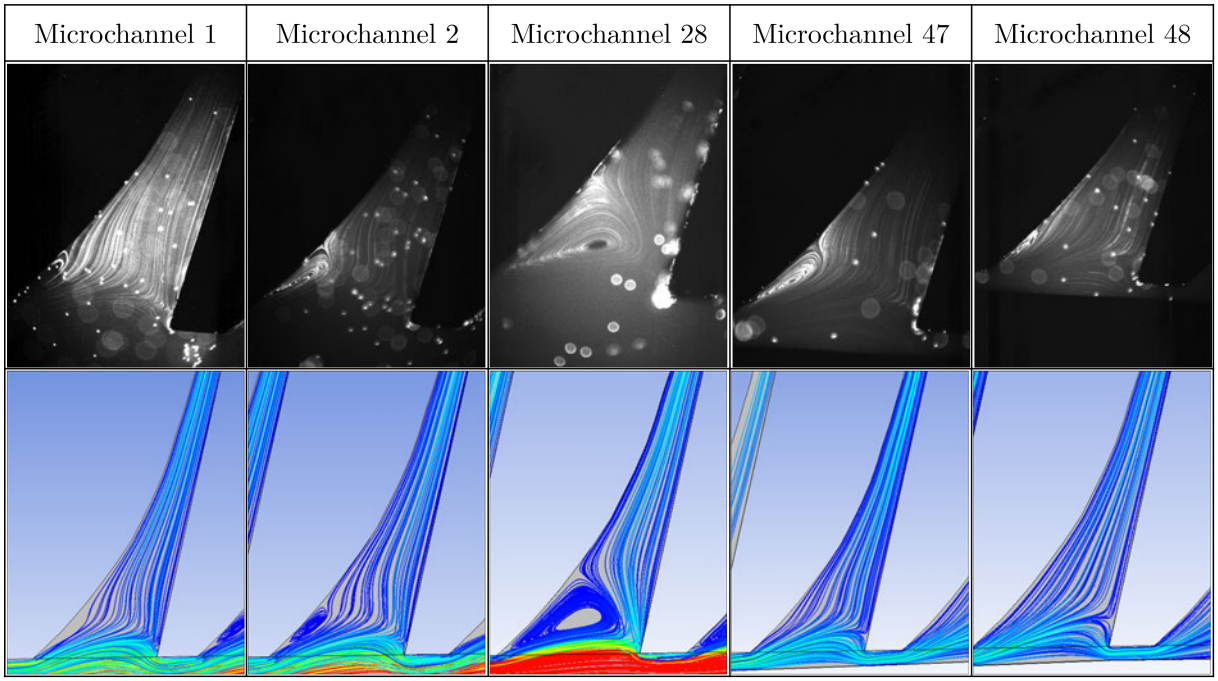


Figure 54: Comparison of fluorescence measurements and CFD results at selected microchannel entries for $\dot{V} = 5\,\mathrm{mL/min}$.

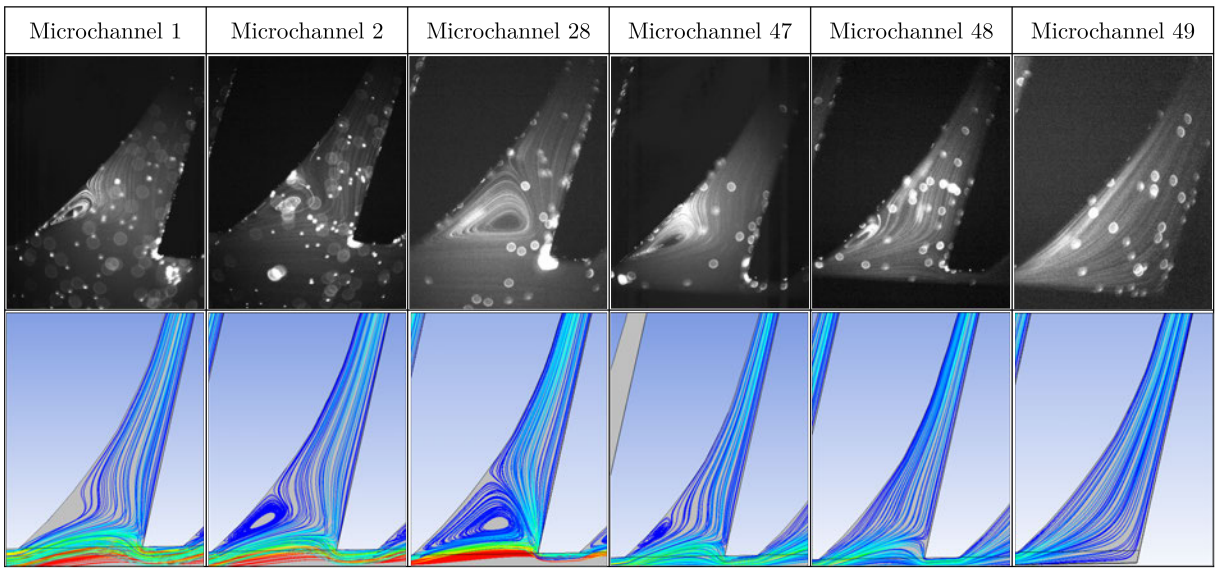


Figure 55: Comparison of fluorescence measurements and CFD results at selected microchannel entries for $\dot{V} = 6\,\mathrm{mL/min}$.

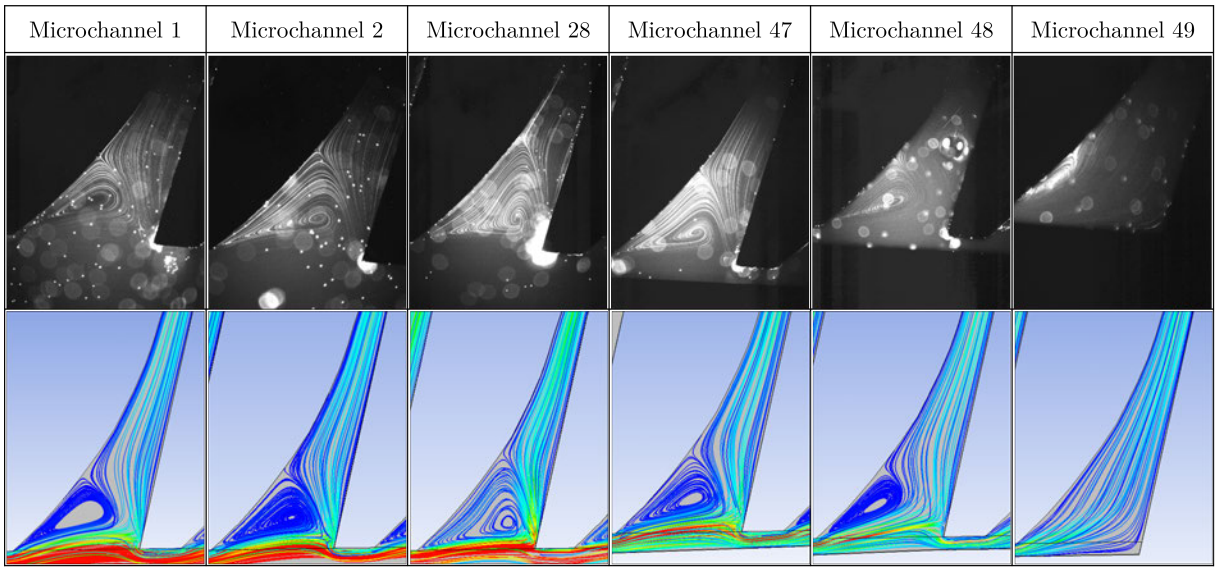


Figure 56: Comparison of fluorescence measurements and CFD results at selected microchannel entries for $\dot{V} = 10\,\mathrm{mL/min}$.

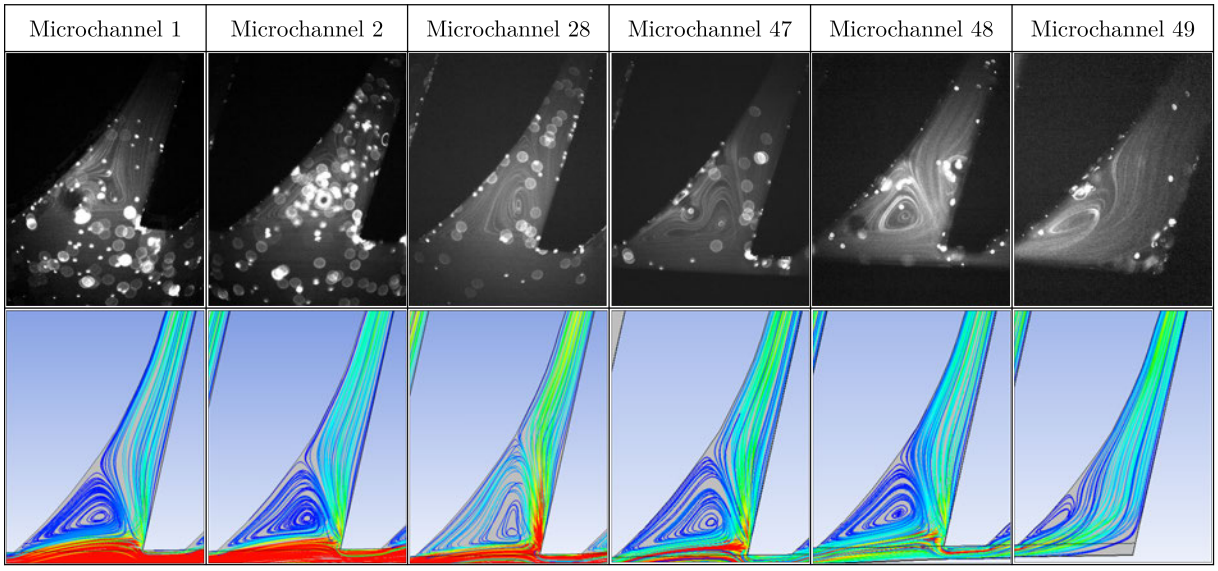


Figure 57: Comparison of fluorescence measurements and CFD results at selected microchannel entries for $\dot{V} = 15\,\mathrm{mL/min}$.

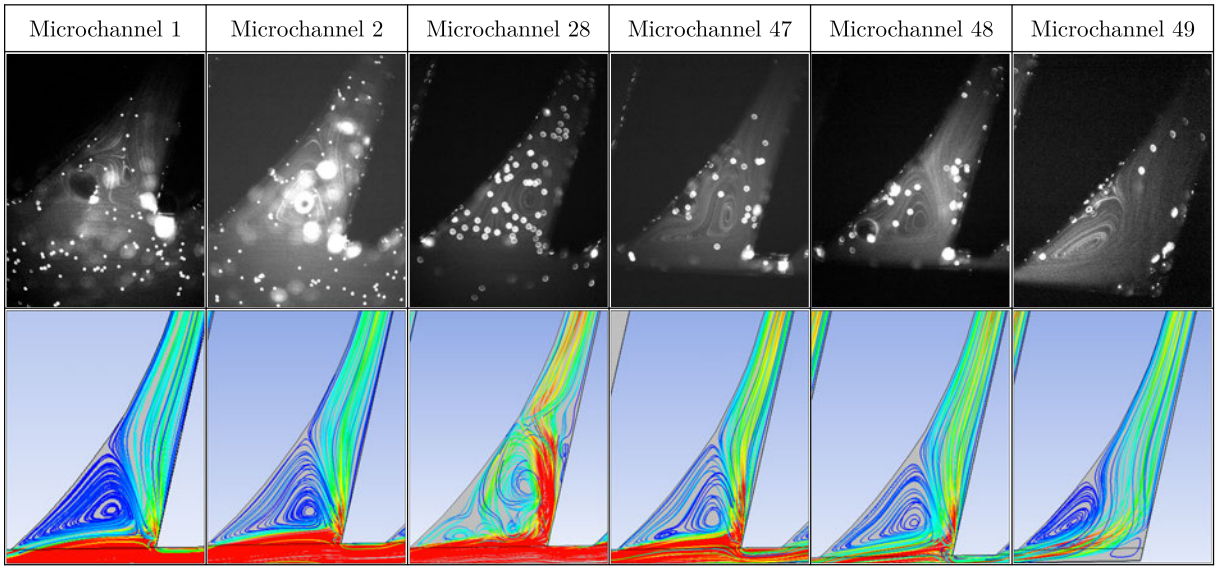


Figure 58: Comparison of fluorescence measurements and CFD results at selected microchannel entries for $\dot{V} = 20\,\mathrm{mL/min}$.

the simulation model developed in this work provides a more precise representation of the flow behaviour, especially at small volumetric flow rates.

In addition to the microchannel entry regions, further locations were investigated, including the central section of microchannel 1 and the outlet regions of microchannel 1 and microchannel 28. The experimental results and the corresponding simulations for these regions are shown in figure 59. All images were acquired at a volumetric flow rate of $\dot{V} = 20\,\mathrm{mL/min}$. Fully developed laminar flow is observable in the experiment and the simulation in the middle of microchannel 1. Likewise, at the microchannel outlet regions of microchannel 1 and microchannel 28, no formation of vortices is visible and the simulation results are in good agreement with the experimental results. Based on these findings, it can be concluded that no unexpected flow behaviour occurs in regions outside the microchannel entry areas under the investigated operating conditions.

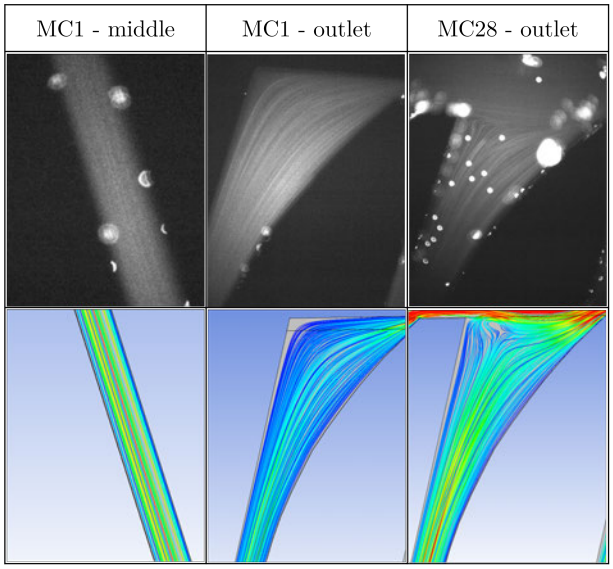


Figure 59: Comparison of fluorescence measurements and CFD results for $\dot{V} = 20\,\mathrm{mL/min}$ at other significant regions.

6.4 Thermal: Infrared Temperature Measurements

In this section, the measurements obtained with the Infrared (IR) camera are presented. First, the experimental setup is described and findings influencing the measurement results are discussed. Subsequently, the measurement results are compared with contour plots from the CFD Simulation in order to investigate the qualitative thermal behaviour across the wafer surface.

The main principle behind IR measurements is that every body with a temperature above 0 K emits thermal radiation. The emitted radiative energy can be described by the Stefan–Boltzmann law:

$$E = \varepsilon \sigma T_\mathrm{s}^4 \tag{66}$$

where E is the emitted radiative energy, ε the surface emissivity (material-dependent), σ the Stefan-Boltzmann constant, and T_s the surface temperature of the investigated object. IR cameras detect the emitted radiation and convert it into temperature values. The measured signal is influenced by several parameters such as the emissivity, reflected ambient radiation and the observation angle relative to the surface normal. In the present experimental setup these parameters are not determined explicitly. In the following investigations the measurement conditions and camera settings were kept constant, to enable a qualitative comparison between different measurements [5, 28].

6.4.1 Experimental Setup

The IR camera used in this experiment was a VarioCam HD manufactured by Infratec [30]. The recorded images were processed using the software Irbis 3 [29]. The camera was positioned on a tripod in front of the sample at a slight angle relative to the normal of the

wafer surface. The wafer was positioned in a fixture surrounded by insulating material (see figure 60). The relative positioning between the camera and the wafer was kept constant throughout all experiments to avoid any influence on the measurement results. The setup was covered with a fabric to block emissive radiation from the surroundings.

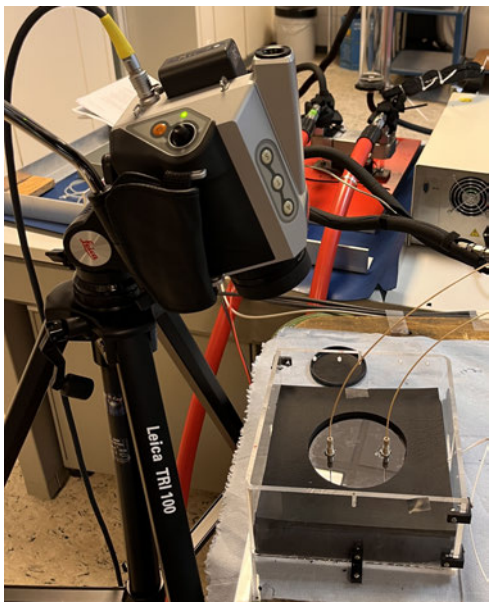


Figure 60: Experimental setup for IR measurements with the camera positioned above the wafer.

During the infrared measurements, it was observed that at a lower temperature range reflections of the thermal radiation emitted by the NanoPort connectors and the coolant pipe increasingly can be seen on the wafer surface. As a consequence the temperature of the NanoPorts was partially reflected and appeared in the IR images, leading to a distortion of the qualitative temperature distribution.

A comparison with the measurement results and the captured temperature ranges in the thesis of Nils Flaschel indicates that those experiments were likely conducted without active cooling of the coolant. Consequently, the IR measurements in the present study were conducted without additional cooling of the coolant, resulting in approximately constant cooling temperature $T_{\text{in}} = 18\,°\text{C}$ measured with the flowmeter for all investigated volumetric flow rates.

6.4.2 Results

In figure 61, figure 62 and figure 63 the images obtained from the IR measurements are compared with temperature contour plots from the simulation using boundary conditions adapted to the experimental measurements. In the IR images, the microchannel layout was added afterwards to provide better orientation. For each volumetric flow rate, an identical colour scale was used for both the simulation results and the IR measurements to enable a direct comparison.

A significant temperature distribution around the microchannel layout in the sample is visible. In general, cooler regions are observed near the inlet side, while higher temperatures occur towards the outlet region. At higher volumetric flow rates, the peak of the isothermal regions becomes more pronounced and shifts towards the right side of the microchannel layout. This behaviour is captured by both the simulation and the IR measurements and indicates the influence of irregular inlet conditions at the microchannel entries induced by the geometry features of the inlet manifold, as presented in section 5.2.3.

Overall, the contour plots and IR images show a comparable global temperature distribution. The main temperature gradients and the location of characteristic warm and cold regions are reproduced consistently. Moreover, it can be shown that estimated flow effects are shown in the temperature distribution and therefore thermal characteristics of the system. However, local deviations occur, especially in areas affected by different materials as the NanoPort connectors or the surrounding adhesive, which leads to locally varying emissivity values and affects the IR measurement.

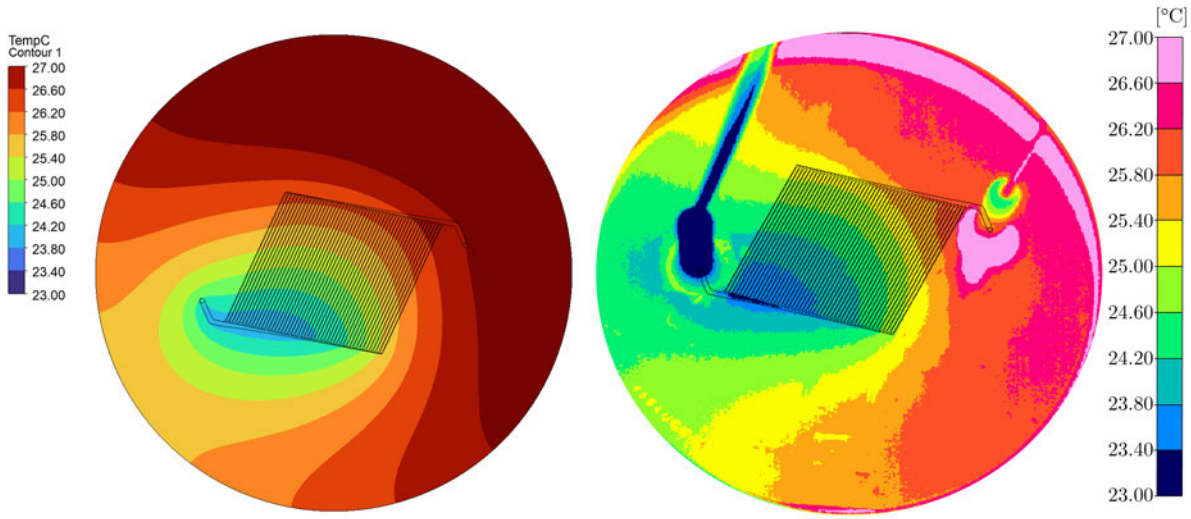


Figure 61: Comparison of temperature contours from CFD simulation (left) and IR measurements (right) at $\dot{V} = 10\,\mathrm{mL/min}$ with $T_{\mathrm{in}} = 18\,^{\circ}\mathrm{C}$.

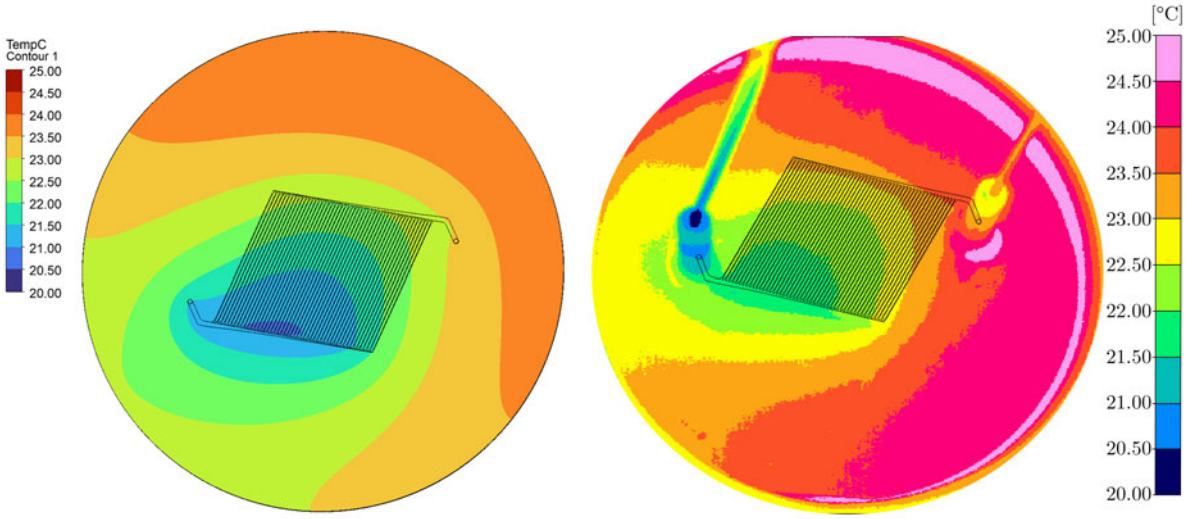


Figure 62: Comparison of temperature contours from CFD simulation (left) and IR measurements (right) at $\dot{V} = 20\,\mathrm{mL/min}$ with $T_{\mathrm{in}} = 18\,^{\circ}\mathrm{C}$.

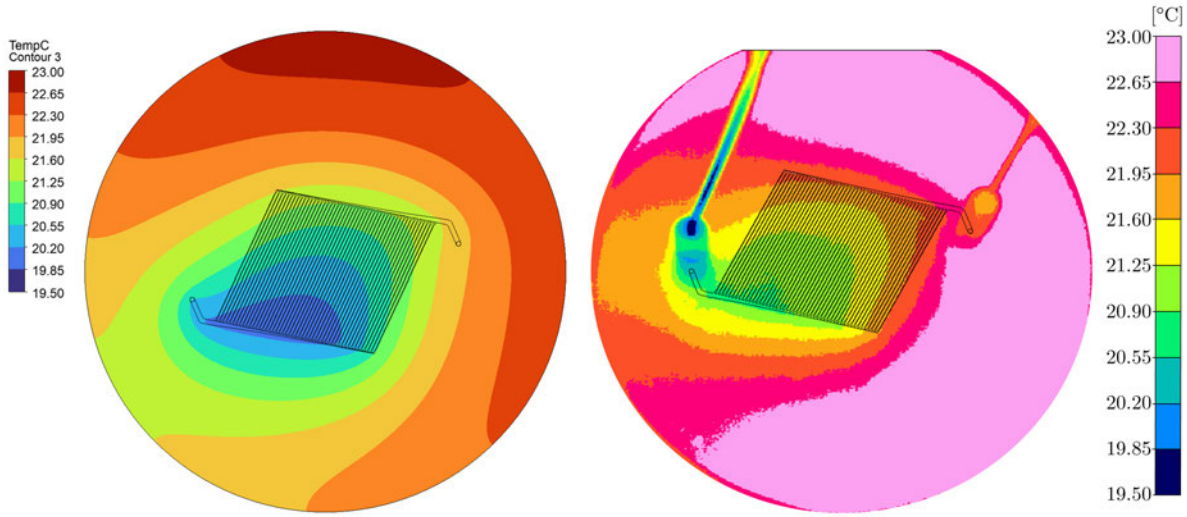


Figure 63: Comparison of temperature contours from CFD simulation (left) and IR measurements (right) at $\dot{V} = 30\,\mathrm{mL/min}$ with $T_{\mathrm{in}} = 18\,^{\circ}\mathrm{C}$.

6.5 Thermal: Pt100 Temperature Measurements

As previously observed, the flow distribution along the inlet manifold changes significantly. To investigate whether these variations in flow behaviour also influence the thermal characteristics of the system, additional measurements were conducted using surface-mounted Pt100 temperature sensors.

6.5.1 Experimental Setup

In comparison to the IR measurements, the chiller was active at a set temperature of $T_{\text{chiller}} = -5\,°\text{C}$ in the following experiments. Thus, the coolant in the primary circuit was cooled down. The defined thermal load was induced by the heating mat attached to the backside of the wafer with $\dot{Q} = 2.5\,\text{W}$. For the temperature measurements, nine Pt100 sensors were attached to the wafer surface across the microchannel layout. The sensors were positioned in order to capture the temperature distribution across the whole microchannel layout and to determine the temperature gradient between the inlet and outlet manifold in different regions. The exact positioning of the sensors is shown in figure 64.

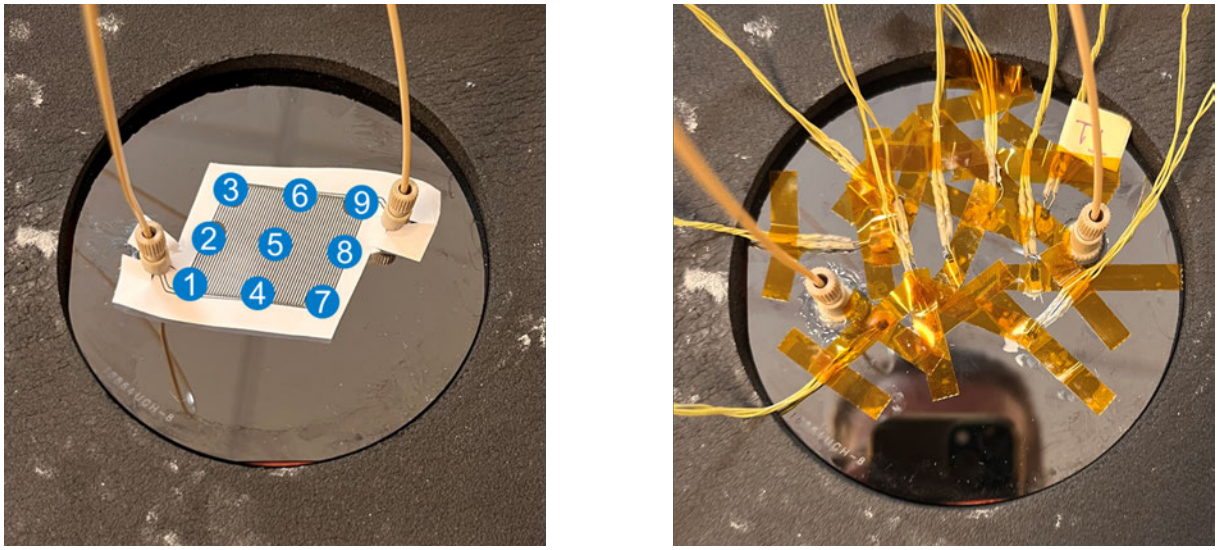


Figure 64: Positioning of the Pt100 sensors on the wafer surface.

The experimental procedure was carried out as follows:

1. Wait until the set chiller temperature T_{chiller} is reached
2. Start Pt100 temperature measurement
3. Switch on the heating mat
4. Start the pump with the set volumetric flow rate
5. Wait until steady-state condition is reached

The measured temperatures were recorded continuously and added to a live plot every 10 seconds. This allowed the steady-state condition to be identified visually during the experiment. Exemplarily, the recorded live plot for the experiment with a set volumetric flow rate of $\dot{V} = 30\,\mathrm{mL/min}$ is shown in figure 65.

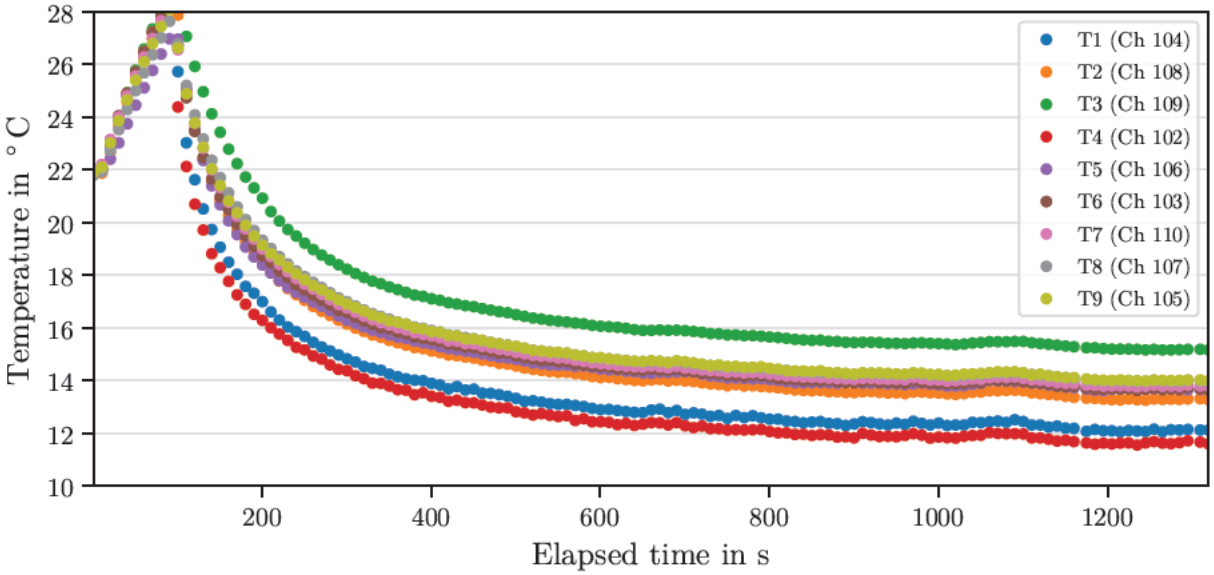


Figure 65: Measured temperature as a function of time at $\dot{V} = 30\,\mathrm{mL/min}$, used to determine the thermal steady-state.

6.5.2 Results

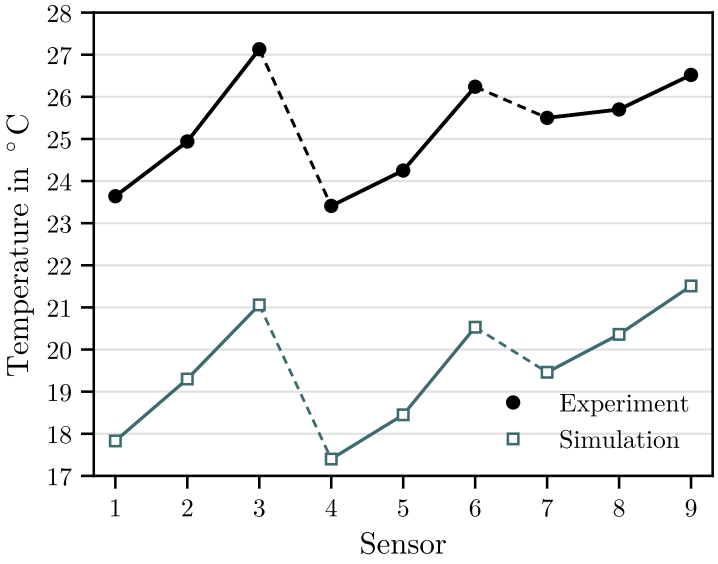
The following figures present the measurement results obtained with the Pt100 sensors in comparison with the results from the CFD simulation for volumetric flow rates of $\dot{V} = 10\,\mathrm{mL/min}$, $\dot{V} = 20\,\mathrm{mL/min}$ and $\dot{V} = 30\,\mathrm{mL/min}$. The simulation values were extracted at wafer surface positions corresponding to the experimental sensor locations.

Overall, the general behaviour as well as the calculated temperature difference show good agreement between simulation and experiment. However, a constant offset between experiment and simulation is visible for all investigated flow rates. At $\dot{V} = 10\,\mathrm{mL/min}$ the measured temperatures are approximately 6 °C higher than the simulated values. With increasing volumetric flow rate this offset decreases to approximately 5 °C for $\dot{V} = 20\,\mathrm{mL/min}$ and 4 °C for $\dot{V} = 30\,\mathrm{mL/min}$. The origin of the observed temperature offset will be analysed in the following section.

Along each sensor line, which is aligned with the flow direction of the microchannels, a clear increase in temperature can be observed. This behaviour is consistent for all investigated flow rates. The largest temperature gradient occurs between sensors 1 and 3, whereas the smallest gradient is observed between sensors 7 and 9. The maximum temperature is consistently measured at sensor 3, while the minimum temperature occurs at sensor 4. Consequently, the largest temperature difference across the microchannel layout is observed between the two positions.

To interpret this result, the measured temperatures can be compared with the simulated inlet temperature distribution of the microchannels shown in figure 42. Sensors 1, 4 and 7 correspond approximately to the inlet regions of different microchannel sections. A similar qualitative behaviour can be observed, the inlet temperature decreases along the first microchannels until a certain position, after which it increases rapidly towards the microchannels located at the end of the manifold. Furthermore, the reduced temperature gradient between sensors 7 and 9 indicates an increased mass flow towards the end of the manifold. This behaviour is consistent with the mass flow distribution predicted by the CFD simulation and shown in figure 42.

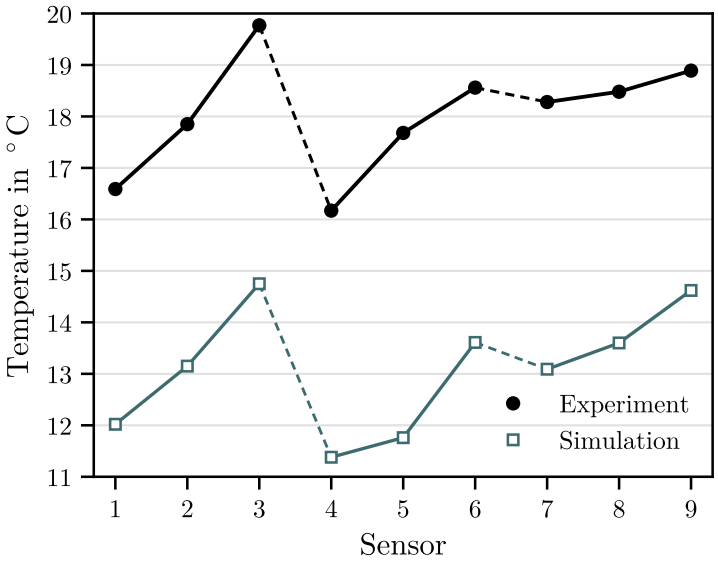
These observations indicate that the temperature distribution on the wafer surface is strongly influenced by the local inlet conditions of the microchannels, which are determined by the flow distribution governed by the manifold geometry and the local flow effects induced by the bend in the inlet manifold. Overall, the results demonstrate that the thermal behaviour of the microchannel layout is strongly influenced by the flow distribution resulting from the manifold geometry.



Temperature gradients ΔT

	Exp.	**Sim.**
$1 \rightarrow 3$	3.49	3.24
$4 \rightarrow 6$	2.83	3.12
$7 \rightarrow 9$	1.02	2.05
$1 \rightarrow 9$	2.88	3.69
Min $\rightarrow$ Max	3.72	4.11

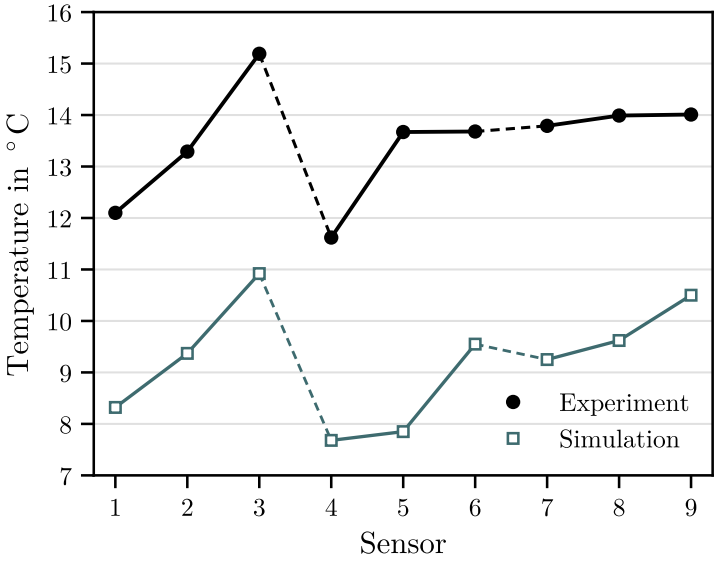
Figure 66: Comparison of measured and simulated temperature at sensor locations for $\dot{V} = 10\,\mathrm{mL/min}$ with $T_{\mathrm{in}} = 12\,^{\circ}\mathrm{C}$.



Temperature gradients ΔT

	Exp.	**Sim.**
$1 \rightarrow 3$	3.18	2.73
$4 \rightarrow 6$	2.40	2.24
$7 \rightarrow 9$	0.61	1.52
$1 \rightarrow 9$	2.31	2.60
Min $\rightarrow$ Max	3.61	3.37

Figure 67: Comparison of measured and simulated temperature at sensor locations for $\dot{V} = 20\,\mathrm{mL/min}$ with $T_{\mathrm{in}} = 8\,°\mathrm{C}$.

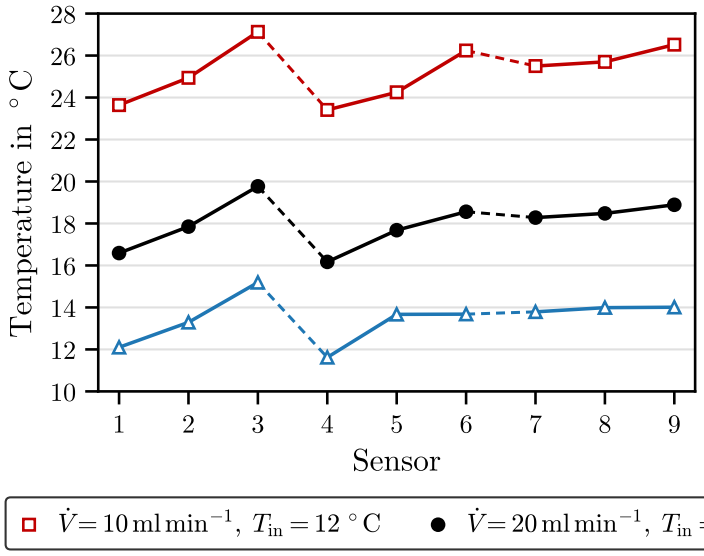


Temperature gradients ΔT

	Exp.	**Sim.**
$1 \rightarrow 3$	3.09	2.60
$4 \rightarrow 6$	2.05	1.87
$7 \rightarrow 9$	0.21	1.25
$1 \rightarrow 9$	1.91	2.18
Min $\rightarrow$ Max	3.57	3.24

Figure 68: Comparison of measured and simulated temperature at sensor locations for $\dot{V} = 30\,\mathrm{mL/min}$ with $T_{\mathrm{in}} = 5\,°\mathrm{C}$.

In figure 69 the experimental measurements for all volumetric flow rates are illustrated. The representation further supports the previously described observations. Moreover, it demonstrates that the overall temperature range on the wafer surface decreases significantly with increasing volumetric flow rate, while the temperature gradients along the sensor lines decrease only slightly.



Temperature gradients ΔT

	□	●	△
$1 \rightarrow 3$	3.49	3.18	3.09
$4 \rightarrow 6$	2.83	2.40	2.05
$7 \rightarrow 9$	1.02	0.61	0.21
$1 \rightarrow 9$	2.88	2.31	1.91
Min $\rightarrow$ Max	3.72	3.61	3.57

□ $\dot{V} = 10\,\mathrm{ml\,min^{-1}}$, $T_{\mathrm{in}} = 12\,^{\circ}\mathrm{C}$ ● $\dot{V} = 20\,\mathrm{ml\,min^{-1}}$, $T_{\mathrm{in}} = 8\,^{\circ}\mathrm{C}$ △ $\dot{V} = 30\,\mathrm{ml\,min^{-1}}$, $T_{\mathrm{in}} = 5\,^{\circ}\mathrm{C}$

Figure 69: Measured temperature at sensor locations for different volumetric flow rates.

6.6 Evaluation of Thermal Measurement Accuracy

The comparison between simulation and experimental Pt100 measurements shows a systematic offset. One hypothesis is that the temperatures obtained from the Pt100 sensors do not necessarily correspond to the surface temperature extracted from the simulation.

Surface temperature measurements with contact sensors are influenced by several thermal resistances between the measured object, the sensor and the surrounding environment [6]. In figure 70, effects that may lead to deviations between the measured sensor temperature and the actual surface temperature are shown. The illustration shows the heat flux from the measured object to the environment. In the present experimental setup, the object temperature is below ambient for $\dot{V} = 20\,\mathrm{mL/min}$ and $\dot{V} = 30\,\mathrm{mL/min}$, resulting in heat transfer from the surroundings to the object.

To investigate the influence of these effects, the accuracy of the applied measurement methods is first evaluated by means of a reference experiment. Subsequently, the influence of the inlet temperature definition used as boundary condition in the CFD simulation is analysed.

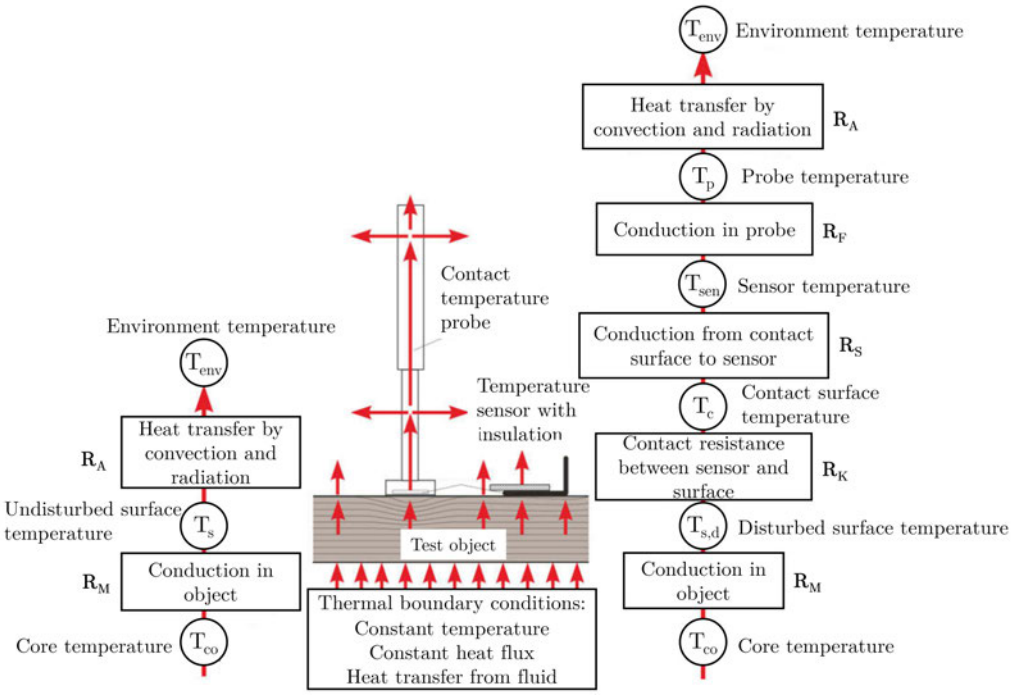


Figure 70: Schematic representation of the factors influencing the undisturbed surface temperature (left) and the surface temperature disturbed by a contact temperature probe or a permanently mounted, flat temperature sensor (right) based on [6].

6.6.1 Reference Experiment for Temperature Measurement Accuracy

To evaluate the accuracy of the temperature measurement methods, a reference measurement was conducted. Therefore, an aluminium plate was cooled down in a refrigerator. After removing the plate from the refrigerator, three Pt100 sensors were attached to the surface with thermal paste and Kapton tape. Additionally, emissivity tape with a defined emissivity of $\varepsilon = 0.95$ was placed on the surface for the infrared measurements [43]. As a reference thermometer a *Greisinger GMH 3200 Series* equipped with a surface temperature probe was used [25]. During the experiment, the plate gradually warmed up due to the heat transfer from the surrounding environment ($T_{\mathrm{env}} = 21\,^{\circ}\mathrm{C}$). The surface temperature was measured at the same time using the Pt100 sensors, the thermometer and the infrared camera focused on the emissivity tape. The measured temperature evolution is shown in figure 71. The recorded temperature difference between the three Pt100 sensors was throughout the whole experiment not larger than 0.1 °C. In the diagram the averaged value of the three sensors is shown. The reference measurement shows a good agreement between the IR camera and the contact thermometer, while the Pt100 sensors exhibit a temperature-dependent deviation. This observation suggests that the Pt100 sensors do not necessarily measure the exact surface temperature under the given experimental conditions. At the same time, the close agreement between the IR camera and the contact thermometer indicates that the use of emissivity tape enables reliable infrared surface temperature measurements for the investigated setup.

The exact reasons for the deviation of the Pt100 sensors cannot be determined further within the scope of this study. Possible influences include the thermal coupling of the sensors to the surface as well as heat exchange between the sensor and the surrounding environment. While the deviations observed for the Pt100 sensors may contribute to the overall discrepancy between simulation and experiment, the magnitude of the measured offset suggests that additional effects may be present. One possible influence is the definition of the inlet temperature used in the CFD model, which is analysed in the following section.

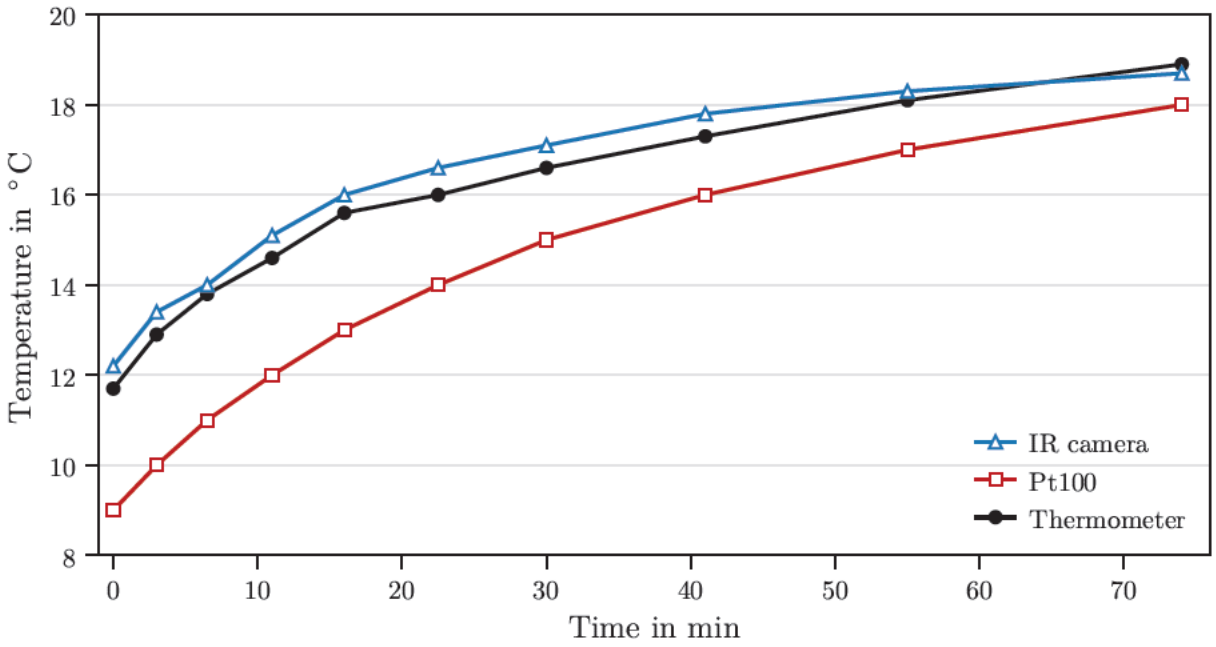


Figure 71: Reference measurement comparing Pt100 sensor, contact thermometer and IR camera during warm-up of a cooled aluminium plate.

6.6.2 Influence of Inlet Temperature Definition

Another possible source of deviation between simulation and experiment is the definition of the inlet temperature T_{in}. In the experiment, the fluid temperature was measured upstream of the sample and directly used as inlet temperature boundary condition in the simulation. Between the flowmeter and the actual sample inlet, the coolant passes through approximately 1 m of 1/8 inch stainless steel tubing and an additional 0.3 m of 1/16 inch PEEK tubing. Here, a temperature increase due to heat transfer from the environment is likely. To estimate the magnitude of this effect, the temperature difference between the flowmeter and the sample inlet is calculated using the thermal resistance (R_{th}). The heat flow from the environment to the fluid is approximated by:

$$\dot{Q} = \frac{T_{\text{env}} - T_{\text{flowmeter}}}{R_{\text{th}}} \tag{67}$$

where R_{th} represents the total thermal resistance between the environment and the fluid. It consists of the external convective resistance, the conductive resistance of the tube wall and the internal convective resistance:

$$R_{\mathrm{th}} = \frac{1}{\alpha_{\mathrm{o}} A_{\mathrm{o}}} + \frac{\ln\left(\frac{r_{\mathrm{o}}}{r_{\mathrm{i}}}\right)}{k_{\mathrm{w}} 2\pi L} + \frac{1}{\alpha_{\mathrm{i}} A_{\mathrm{i}}} = 13.1\,\mathrm{K/W} \tag{68}$$

Based on the geometric parameters ($A_{\mathrm{o}} = 9.97 \times 10^{-3}\,\mathrm{m}^2$, $A_{\mathrm{i}} = 5.58 \times 10^{-3}\,\mathrm{m}^2$ [41], $L = 1\,\mathrm{m}$) and the thermal conductivity of the pipe $k_{\mathrm{w}} = 15\,\mathrm{W/(m\,K)}$ (the PEEK tubing is neglected), the total thermal resistance is $R_{\mathrm{th}} = 13.1\,\mathrm{K/W}$.

The external heat transfer coefficient is estimated using a simplified equation for natural convection including radiative effects at a pipe in ambient air ($T_{\mathrm{env}} = 21\,^{\circ}\mathrm{C}$) [48]:

$$\alpha_{\mathrm{o}} = 8\,\mathrm{W/(m^2\,K)} + 0.04\,\mathrm{W/(m^2\,K^2)} \cdot \Delta T \approx 8.5\,\mathrm{W/(m^2\,K)} \tag{69}$$

Due to the weak dependence on the temperature difference, only minor variations are obtained for the investigated cases. Therefore, an average value of $\alpha_{\mathrm{o}} = 8.5\,\mathrm{W/(m^2\,K)}$ is used.

For the internal convection, a Nusselt number of $Nu = 3.66$ is used, corresponding to laminar fully developed flow in a circular tube [5]. Using the properties of Novec7100 [1], this results in an internal heat transfer coefficient of $\alpha_{\mathrm{i}} = 141.86\,\mathrm{W/(m^2\,K)}$.

Using the measured fluid temperatures at the flowmeter, the resulting heat transfer rates can be determined with equation (67):

$$\dot{Q}\,(\dot{V} = 10\,\mathrm{mL/min} \rightarrow T_{\mathrm{flowmeter}} = 12\,^{\circ}\mathrm{C}) = 0.7\,\mathrm{W} \tag{70}$$

$$\dot{Q}\,(\dot{V} = 30\,\mathrm{mL/min} \rightarrow T_{\mathrm{flowmeter}} = 5\,^{\circ}\mathrm{C}) = 1.2\,\mathrm{W} \tag{71}$$

The resulting temperature increase of the fluid between the flowmeter and the sample inlet can then be estimated by:

$$\Delta T = \frac{\dot{Q}}{\dot{m} c_{\mathrm{p}}} \tag{72}$$

This results in:

$$\Delta T(\dot{V} = 10\,\mathrm{mL/min} \rightarrow T_{\mathrm{flowmeter}} = 12\,^{\circ}\mathrm{C}) = 2.3\,^{\circ}\mathrm{C} \tag{73}$$

$$\Delta T(\dot{V} = 30\,\mathrm{mL/min} \rightarrow T_{\mathrm{flowmeter}} = 5\,^{\circ}\mathrm{C}) = 1.4\,^{\circ}\mathrm{C} \tag{74}$$

Although this calculation represents only a rough estimate, it indicates that the actual coolant inlet temperature at the sample is higher than the temperature measured at the flowmeter. The heat input from the environment increases with increasing temperature difference between the fluid and the surroundings. Nevertheless, the resulting temperature rise of the coolant decreases with increasing volumetric flow rate due to the higher mass

flow. This behaviour is consistent with the observed offset between experiment and simulation and therefore provides a plausible explanation for the decreasing temperature difference at higher volumetric flow rates.

7 Conclusion

The aim of this work was to restore the capability to experimentally investigate the fluid-dynamic and thermal behaviour of microchannel prototypes by recommissioning and extending an existing test setup. This facilitated the characterisation of a previously uncharacterised microchannel layout. In addition, a combined theoretical and numerical approach was developed to analyse and interpret the observed fluid-dynamic and heat transfer behaviour.

The recommissioned test setup enabled stable and reproducible measurements, while analytical models and CFD simulations were validated against experimental data to evaluate their accuracy. These combined approaches provided consistent insights and were used to guide targeted extensions of the measurements. For example, this work introduced a position-dependent investigation of vortex formation, providing evidence of flow non-uniformities.

The key findings of this work can be summarised as follows. The analytical model captures the main qualitative trends of the system behaviour, including the velocity distribution along the manifold, contributions to the pressure drop, and the influence of initial conditions at the microchannels on heat transfer. However, additional effects such as location-dependent vortex formation can only be resolved by CFD simulations and are subsequently confirmed by fluorescence measurements, indicating locally varying flow behaviour across the microchannel layout. This non-uniform flow behaviour leads to a pronounced flow maldistribution between the microchannels, which significantly affects the thermal behaviour. Higher mass flow rates within individual microchannels reduce local temperature gradients, a trend that is consistently observed in both simulations and experiments. Finally, the inlet manifold geometry, particularly the bend, is a key factor influencing local flow structures and thereby the thermal behaviour of the system.

Overall, the results of this work demonstrate that a reliable combined analytical, numerical simulation and experimental approach for the investigation of microchannel cooling prototypes has been established. Consequently, the presented framework enables a systematic analysis of design parameters and their impact on flow and heat transfer behaviour. Future work can build upon this foundation by further refining the models, improving measurement accuracy and systematically investigating design variations to optimise the performance and facilitate integration in detector applications. The developed framework, key findings, and future perspectives are summarised in figure 72.

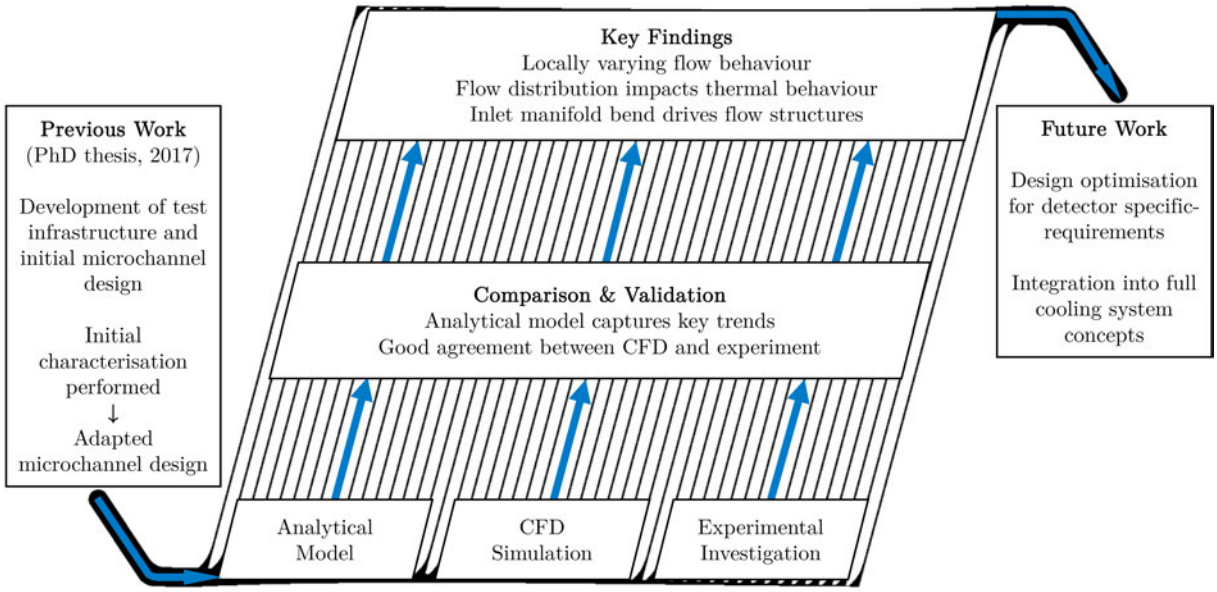


Figure 72: Overview of the methodology, key findings and future work.

Bibliography

[1] 3M: *3M™ Novec™ High-Tech Flüssigkeit 7100*. 2009. URL: https://multimedia.3m.com/mws/media/1998180/3m-novec-7100-engineered-fluid.pdf (visited on 14-10-2025).

[2] ANSYS, Inc.: *Fluent Theory Guide*. Canonsburg, 2021. URL: https://dl.cfdexperts.net/cfd_resources/Ansys_Documentation/Fluent/Ansys_Fluent_Theory_Guide.pdf (visited on 27-12-2025).

[3] ANSYS, Inc.: *Meshing User's Guide*. Canonsburg, 2025. URL: https://ansyshelp.ansys.com/public/Views/Secured/corp/v251/en/pdf/ANSYS_Meshing_Users_Guide.pdf (visited on 26-12-2025).

[4] Arduino: *UNO R3 | Arduino Documentation*. URL: https://docs.arduino.cc/hardware/uno-rev3/ (visited on 31-10-2025).

[5] Bergman, T. L.; Lavine, A. S.: *Fundamentals of Heat and Mass Transfer*. 8th ed. Hoboken, NJ: John Wiley & Sons, 2017.

[6] Bernhard, F.: *Handbuch der Technischen Temperaturmessung*. 2nd ed. Berlin, Heidelberg: Springer, 2014. URL: https://link.springer.com/10.1007/978-3-642-24506-0 (visited on 9-3-2026).

[7] Böswirth, L.; Bschorer, S.: *Technische Strömungslehre: Lehr- Und Übungsbuch*. 9th ed. Wiesbaden: Vieweg+Teubner Verlag, 2012.

[8] Bronkhorst: *FlowDDE Software*. URL: https://www.bronkhorst.com/de/produkte/software/flowdde/ (visited on 31-10-2025).

[9] Bronkhorst: *FlowPlot Software*. URL: https://www.bronkhorst.com/de/produkte/software/flowplot/ (visited on 31-10-2025).

[10] Bronkhorst: *FlowView Software*. URL: https://www.bronkhorst.com/de/produkte/software/flowview/ (visited on 31-10-2025).

[11] Bronkhorst High-Tech B.V.: *Mini CORI-FLOW M14*. URL: https://products.bronkhorst.com/media/cawjunvf/3157-m14-de-datasheet.pdf (visited on 15-10-2025).

[12] Bruns, H.: *Theoretical Microfluidics*. Denmark: Technical University of Denmark, 2006. URL: https://homes.nano.aau.dk/lg/Lab-on-Chip2008_files/HenrikBruus_Microfluidics%20lectures.pdf (visited on 14-10-2025).

[13] EL-CAT Inc.: *Properties of Silicon and Silicon Wafer*. URL: https://www.el-cat.com/silicon-properties.htm (visited on 24-2-2026).

[14] Catherine Bolgar: *AI Chips Are Getting Hotter. A Microfluidics Breakthrough Goes Straight to the Silicon to Cool up to Three Times Better.* URL: https://news.microsoft.com/source/features/innovation/microfluidics-liquid-cooling-ai-chips/ (visited on 17-3-2026).

[15] CERN: *HiLumi LHC*. URL: https://home.cern/science/accelerators/hilumi-lhc (visited on 16-3-2026).

[16] CERN: *The Future Circular Collider*. URL: https://home.cern/science/accelerators/future-circular-collider (visited on 16-3-2026).

[17] Corning Glass Works: *Pyrex*. New York, 1987. URL: https://glassfab.com/wp-content/uploads/2015/08/Corning-Pyrex.pdf.

[18] *DIN EN IEC 60751:2023-06, Industrielle Platin-Widerstandsthermometer Und Platin-Temperatursensoren (IEC 60751:2022); Deutsche Fassung EN IEC 60751:2022*. 2023.

[19] ECOM spol. s r.o.: *IOTA 50, 100, 300 Preparative Pumps*. URL: https://www.ecomsro.com/iota-300-preparative-pump-1-300-ml-min-7-5mpa (visited on 13-10-2025).

[20] Edelstahl-Wärmetauscher: *EWT-BE4-10*. URL: https://www.edelstahl-waermetauscher.de/pic/Plattenwaermetauscher%20EWT-BE4-10.pdf (visited on 15-10-2025).

[21] Fernandez-Cuesta, I.: *Nano-Opto-Fluidics Lab*. URL: https://www.physik.uni-hamburg.de/en/inf/jg-fernandez-cuesta.html (visited on 29-12-2025).

[22] Ferziger, J. H.; Perić, M.; Street, R. L.: *Computational Methods for Fluid Dynamics*. Vol. 4. Berlin, Heidelberg: Springer, 2020.

[23] Flaschel, N.: *Micro-Channel Cooling for Silicon Detectors*. Hamburg University, 2017. URL: https://bib-pubdb1.desy.de/record/396403/files/Flaschel-thesis.pdf (visited on 1-10-2025).

[24] Gargiulo, C. et al.: *Proposal for DRD8 Mechanics & Cooling of Future Vertex and Tracking Systems*. URL: https://cernbox.cern.ch/pdf-viewer/public/fJ64iTqktDFCnVt/DRD8_proposal_updated_2Dec2024.pdf (visited on 16-3-2026).

[25] GHM GROUP: *GMH 32 Serie - Präzisionssekundenthermometer Für Thermoelemente*. URL: https://www.greisinger.de/files/upload/de/produkte/sheet/GMH32xx_d_datenblatt.pdf (visited on 15-3-2026).

[26] Idelchik, I. E.: *Handbook of Hydraulic Resistance*. 3rd ed. Moscow: begell house, 2001.

[27] IDEX Health & Science: *NanoPort Assemblies*. URL: https://www.idex-hs.com/resources/resources-detail/nanoport-assemblies (visited on 7-11-2025).

[28] InfraTec GmbH: *Infrared Thermography Theory - Physical Basics*. URL: https://www.infratec.eu/thermography/service-support/glossary/theory/ (visited on 6-3-2026).

[29] InfraTec GmbH: *Leistungsfähige Thermografie-Software von InfraTec*. URL: https://www.infratec.de/thermografie/thermografie-software/#vorteile (visited on 10-3-2026).

[30] InfraTec GmbH: *VarioCAM High Definition*. URL: https://media.infratec.eu/infratec-variocam-hd-b-de-mail.pdf (visited on 10-3-2026).

[31] Kandlikar, S. et al.: *Heat Transfer and Fluid Flow in Minichannels and Microchannels*. Oxford: Elsevier, 2005.

[32] Keithley: *7700 20-Channel, Differential Multiplexer Module*. 2018. URL: https://download.tek.com/datasheet/7700_DAQ_Card_Datasheet.pdf (visited on 31-10-2025).

[33] Kumaraguruparan, G. et al.: *A Numerical and Experimental Investigation of Flow Maldistribution in a Micro-Channel Heat Sink*. In: *International Communications in Heat and Mass Transfer* 38.10 (2011), pp. 1349–1353. URL: https://www.sciencedirect.com/science/article/pii/S0735193311001990 (visited on 26-1-2026).

[34] Loctite: *Loctite Superkleber Glaskleber*. URL: https://datasheets.tdx.henkel.com/LOCTITE-SUPERKLEBER-Glass-de_AT.pdf.

[35] Oertel, H., ed.: *Prandtl - Führer Durch Die Strömungslehre: Grundlagen Und Phänomene*. 15th ed. Wiesbaden: Springer Fachmedien, 2022.

[36] Rausch, M. H. et al.: *Density, Surface Tension, and Kinematic Viscosity of Hydrofluoroethers HFE-7000, HFE-7100, HFE-7200, HFE-7300, and HFE-7500.* In: *Journal of Chemical & Engineering Data* 60.12 (2015), pp. 3759–3765. URL: https://pubs.acs.org/doi/10.1021/acs.jced.5b00691 (visited on 21-1-2026).

[37] Stadler, S.: *Proof of Concept for Single-phase SOI-based Microchannel Cooling of Large Semiconductor Detectors by Fabricating and Verifying Equivalent Test Structures.* Munich University of Applied Sciences, May 23, 2022. URL: https://www.researchgate.net/publication/362388183_Proof_of_Concept_for_Single-phase_SOI-based_Microchannel_Cooling_of_Large_Semiconductor_Detectors_by_Fabricating_and_Verifying_Equivalent_Test_Structures (visited on 24-11-2025).

[38] Swagelok: *Filter.* URL: https://www.swagelok.com/downloads/webcatalogs/de/ms-01-92.pdf (visited on 15-10-2025).

[39] Swagelok: *Industrielle Druckmesswandler Standard-Industrie (Modell S).* URL: https://www.swagelok.com/downloads/webcatalogs/de/MS-02-225.PDF (visited on 15-10-2025).

[40] Swagelok: *Regulier- Und Absperrventile.* URL: https://www.swagelok.com/downloads/webcatalogs/de/ms-01-164.pdf (visited on 15-10-2025).

[41] Swagelok: *Rohrdaten.* URL: https://www.swagelok.com/downloads/webcatalogs/de/ms-01-107.pdf (visited on 16-3-2026).

[42] Tektronix: *Keithley 2700 Multimeter/Data Acquisition/Switch Systems.* URL: https://www.tek.com/en/products/keithley/data-acquisition-daq-systems/2700-multimeter-data-acquisition-switch-system (visited on 31-10-2025).

[43] Testo SE & Co. KGaA: *Klebeband z.B. Für Blanke Oberflächen - Für Messungen an Reflektierenden Oberflächen.* URL: https://www.testo.com/de-DE/klebeband-z-b-fuer-blanke-oberflaechen/p/0554-0051 (visited on 15-3-2026).

[44] UHU GmbH: *Max Repair Power.* URL: https://www.uhu.com/getmedia/aa7d9a62-d26b-498e-9179-a1d52dce771f/Print%20PDF.pdf (visited on 11-11-2025).

[45] UHU GmbH: *Plus Schnellfest.* URL: https://www.uhu.com/getmedia/2790d412-ce5a-437b-b878-bc821ab8e9b0/Print%20PDF.pdf (visited on 10-11-2025).

[46] Ullán, M. et al.: *Development of Silicon Interposers with Embedded Microchannels and Metal Re-Distribution Layer for the Integration of Hybrid Detector Systems.* In: *Nuclear Instruments and Methods in Physics Research Section A: Accelerators, Spectrometers, Detectors and Associated Equipment* 1065 (2024). URL: https://www.sciencedirect.com/science/article/pii/S0168900224004169 (visited on 21-10-2025).

[47] Van Erp, R. et al.: *Co-Designing Electronics with Microfluidics for More Sustainable Cooling.* In: *Nature* 585 (2020), pp. 211–216. URL: https://www.nature.com/articles/s41586-020-2666-1 (visited on 17-3-2026).

[48] VDI-Gesellschaft Verfahrenstechnik und Chemieingenieurwesen: *VDI Wärmeatlas.* 10th ed. Berlin, Heidelberg: Springer, 2006.

[49] White, F.: *Fluid Mechanics.* 7th ed. New York: McGraw-Hill, 2009.

[50] Will, D.; Gebhardt, N.: *Hydraulik: Grundlagen, Komponenten, Systeme.* 6th ed. Berlin, Heidelberg: Springer, 2014.

[51] Yakubu, A. U. et al.: *A Comprehensive Review of Primary Cooling Techniques and Thermal Management Strategies for Polymer Electrolyte Membrane Fuel Cells PEMFC.* In: *Heliyon* 10.19 (2024). URL: https://www.cell.com/heliyon/abstract/S2405-8440(24)14587-2 (visited on 20-3-2026).

Appendix

A Measurement System Scripts

The measurement system scripts were developed by the author. AI-based tools were used to assist with implementation and optimization.

A.1 Arduino Script for Pressure Transducer Readout

```
// Arduino Pressure Measurement for Two Transducers
// Transducer A: A0, Transducer B: A5
// 0-5V output corresponds to 0-100 bar

const int transducerA_pin = A0;
const int transducerB_pin = A5;

const float max_voltage = 5.0;
const float max_pressure = 100.0; // bar
const int adc_resolution = 1023; // 10-bit ADC

void setup() {
  Serial.begin(9600);
}

void loop() {
  // Read analog values
  int rawA = analogRead(transducerA_pin);
  int rawB = analogRead(transducerB_pin);

  // Convert to voltage
  float voltageA = rawA * (max_voltage / adc_resolution);
  float voltageB = (rawB * max_voltage) / adc_resolution;

  // Convert voltage to pressure -(05V = -0100 bar)
  float pressureA = (voltageA / 5.0) * 100.0;
  float pressureB = (voltageB / 5.0) * 100.0;

  // Print voltages and pressures
  Serial.print("Transducer A: ");
  Serial.print(voltageA, 3);
  Serial.print(" V, pressure: ");
  Serial.print(pressureA, 2);
  Serial.print(" bar\t");
```

```
35
36    Serial.print("Transducer B: ");
37    Serial.print(voltageB, 3);
38    Serial.print(" V, pressure: ");
39    Serial.print(pressureB, 2);
40    Serial.println(" bar");
41
42    delay(1000); // Wait 1 second
43  }
```

A.2 Python Script for Flowmeter Readout

```
1  import win32ui
2  import dde
3  import time
4  import csv
5  import os
6  from datetime import datetime, timezone, timedelta
7
8  # ------------------------------------------------------------
9  # Output directory for storing measurement data
10 # Path generalized for appendix presentation
11 # ------------------------------------------------------------
12 OUTPUT_FOLDER = "flowmeter_measurements"
13
14 if __name__ == "__main__":
15     # ------------------------------------------------------------
16     # Prepare output file for continuous data logging
17     # ------------------------------------------------------------
18     os.makedirs(OUTPUT_FOLDER, exist_ok=True)
19     cet = timezone(timedelta(hours=1))
20     timestamp_str = datetime.now(cet).strftime("%Y-%m-%d_%H-%M-%S")
21     csv_filename = f"flowmeter_measurements_{timestamp_str}.csv"
22     csv_path = os.path.join(OUTPUT_FOLDER, csv_filename)
23
24     headers = [
25         "Timestamp",
26         "ElapsedTime [s]",
27         "Flow rate [ml/min]",
28         "Temperature [°C]",
29         "Density [kg/m³]"
30     ]
31     start_time = time.time()
32
33     with open(csv_path, mode="w", newline="") as csvfile:
34         writer = csv.writer(csvfile)
35         writer.writerow(headers)
```

```
36
37
38
39
40          # ------------------------------------------------
41          # Create DDE client for communication with the
42          # flowmeter software interface
43          # ------------------------------------------------
44          server = dde.CreateServer()
45          server.Create("FlowDDEClient")
46          conversation = dde.CreateConversation(server)
47
48          try:
49              # Connect to the flowmeter data channel
50              conversation.ConnectTo("FlowDDE", "C(1)")
51
52              print(f"Starting measurements. Data are saved to {csv_path}")
53
54              while True:
55                  # ------------------------------------------------
56                  # Read raw flowmeter values from the DDE interface
57                  # P(8): raw flow signal
58                  # P(142): fluid temperature
59                  # P(270): fluid density
60                  # ------------------------------------------------
61                  flow_rate_raw =
                        float(conversation.Request("P(8)").replace(",", "."))
62                  temperature_raw =
                        float(conversation.Request("P(142)").replace(",", "."))
63                  density_kg_m3 =
                        float(conversation.Request("P(270)").replace(",", "."))
64
65                  # ------------------------------------------------
66                  # Convert raw flow signal to volumetric flow rate
67                  # using the device-specific scaling factor
68                  # ------------------------------------------------
69                  flow_ml_min = (flow_rate_raw / 32000) * 43.86
70
71                  # ------------------------------------------------
72                  # Convert raw temperture signal from percent to
73                  # degree Celsius (100 % = 100 °C)
74                  # ------------------------------------------------
75                  temperature_c = temperature_raw
76
77                  # ------------------------------------------------
78                  # Store current measurement values with timestamp
79                  # ------------------------------------------------
80                  now = datetime.now(cet)
```

```
                elapsed = time.time() - start_time

                row = [
                    now.strftime("%Y-%m-%d %H:%M:%S"),
                    f"{elapsed:.1f}",
                    f"{flow_ml_min:.2f}",
                    f"{temperature_c:.2f}",
                    f"{density_kg_m3:.2f}"
                ]
                writer.writerow(row)
                csvfile.flush()

                # Print current values for live monitoring
                print(f"Flow rate: {flow_ml_min:.2f} ml/min")
                print(f"Temperature: {temperature_c:.2f} °C")
                print(f"Density: {density_kg_m3:.2f} kg/m³")
                print("---")

                # Wait until next measurement cycle
                time.sleep(10)

        except KeyboardInterrupt:
            print("\nMeasurement stopped by user.")

        except Exception as e:
            print(f"Error communicating with FlowDDE: {e}")

        finally:
            # Properly shut down DDE server connection
            server.Shutdown()
```

A.3 Python Script for Pt100 Sensor Readout

```
import socket
import math
import re
from typing import Optional
import time
import tkinter as tk
from tkinter import ttk
import csv
import os
from datetime import datetime, timezone, timedelta
import matplotlib.pyplot as plt


```

```
15
16 # ------------------------------------------------------------
17 # Instrument configuration
18 # Keithley 2701 used for four-wire resistance measurements
19 # ------------------------------------------------------------
20 KEITHLEY_IP = "<IP_ADDRESS>"
21 KEITHLEY_PORT = 1394
22
23
24 # ------------------------------------------------------------
25 # Communication class for the Keithley 2701 via TCP/IP
26 # ------------------------------------------------------------
27 class Keithley2701:
28     def __init__(self, ip, port=1394, timeout=5):
29         self.ip = ip
30         self.port = port
31         self.timeout = timeout
32         self.sock: Optional[socket.socket] = None
33
34     def connect(self):
35         # Establish connection to the measurement device
36         self.sock = socket.create_connection((self.ip, self.port),
               timeout=self.timeout)
37
38     def disconnect(self):
39         # Close the connection after the measurement
40         if self.sock:
41             self.sock.close()
42             self.sock = None
43
44     def send_command(self, command):
45         # Send SCPI command to the instrument
46         if not self.sock:
47             raise RuntimeError("Not connected to instrument.")
48         self.sock.sendall((command + "\n").encode())
49
50     def query(self, command, buffer_size=1024):
51         # Send command and return instrument response
52         self.send_command(command)
53         assert self.sock is not None
54         return self.sock.recv(buffer_size).decode().strip()
55
56 # ------------------------------------------------------------
57 # Conversion of measured resistance to temperature
58 # using the Callendar-Van-Dusen equation
59 # ------------------------------------------------------------
60 class PT100Sensor:
61     def __init__(self, R0=100.0):
```

```
        self.R0 = R0
        self.A = 3.9083e-3
        self.B = -5.775e-7

    def resistance_to_temperature(self, Rt):
        discriminant = self.A**2 - 4 * self.B * (1 - Rt / self.R0)

        # Return NaN if the resistance value is outside the valid range
        if discriminant < 0:
            return float("nan")

        return (-self.A + math.sqrt(discriminant)) / (2 * self.B)

# ------------------------------------------------------------
# Channel assignment
# Mapping of Keithley channels to specific sensors
# ------------------------------------------------------------
ordered_channel_sensor = [
    (101, "T0"),
    (104, "T1"),
    (108, "T2"),
    (109, "T3"),
    (102, "T4"),
    (106, "T5"),
    (103, "T6"),
    (110, "T7"),
    (107, "T8"),
    (105, "T9"),
]

all_channels = [ch for ch, _ in ordered_channel_sensor]
channel_to_sensor = {ch: name for ch, name in ordered_channel_sensor}

# ------------------------------------------------------------
# GUI for selecting the sensors to be monitored
# ------------------------------------------------------------
def select_sensors_gui(all_channels):
    selected = []

    def on_start():
        for idx, var in enumerate(vars_):
            if var.get():
                selected.append(all_channels[idx])
        root.destroy()

    root = tk.Tk()
    root.title("Select Sensors to Measure")

```

```
    vars_ = []
    for idx, ch in enumerate(all_channels):
        var = tk.BooleanVar()
        sensor_label = channel_to_sensor.get(ch, f"{ch}")
        chk = ttk.Checkbutton(
            root,
            text=f"Sensor {sensor_label} (Ch {ch})",
            variable=var
        )
        chk.grid(row=idx, column=0, sticky="w")
        vars_.append(var)

    start_btn = ttk.Button(root, text="Start Measurement",
        command=on_start)
    start_btn.grid(row=len(all_channels), column=0, pady=10)

    root.mainloop()
    return selected

# ------------------------------------------------------------
# Output directory for storing measurement data
# Path generalized for appendix presentation
# ------------------------------------------------------------
OUTPUT_FOLDER = "pt100_measurements"

if __name__ == "__main__":
    # Select channels to be measured
    selected_channels = select_sensors_gui(all_channels)

    if not selected_channels:
        print("No sensors selected. Exiting.")
        exit(0)

    keithley = Keithley2701(KEITHLEY_IP, KEITHLEY_PORT)
    pt100 = PT100Sensor()

    # ------------------------------------------------------------
    # Prepare CSV file for data logging
    # ------------------------------------------------------------
    os.makedirs(OUTPUT_FOLDER, exist_ok=True)
    cet = timezone(timedelta(hours=1))
    timestamp_str = datetime.now(cet).strftime("%Y-%m-%d_%H-%M-%S")
    csv_filename = f"pt100_measurements_{timestamp_str}.csv"
    csv_path = os.path.join(OUTPUT_FOLDER, csv_filename)

    sensor_headers = [f"{name} [°C]" for _, name in ordered_channel_sensor]
    headers = ["Timestamp", "ElapsedTime [s]"] + sensor_headers
    start_time = time.time()
```

```
157
158     # ------------------------------------------------------
159     # Live plot setup
160     # The live visualization was used to identify when a
161     # thermal steady state was reached
162     # ------------------------------------------------------
163     plt.ion()
164     fig, ax = plt.subplots(figsize=(10, 6))
165     lines = {}
166     time_data = []
167     temp_data = {ch: [] for ch in selected_channels}
168
169     for ch in selected_channels:
170         label = channel_to_sensor.get(ch, str(ch))
171         (line,) = ax.plot([], [], linestyle="None", marker="o",
                label=f"{label} (Ch {ch})")
172         lines[ch] = line
173
174     ax.set_xlabel("Elapsed Time [s]")
175     ax.set_ylabel("Temperature [°C]")
176     ax.set_title("Live Pt100 Sensor Temperatures")
177     ax.legend()
178     plt.tight_layout()
179
180     # ------------------------------------------------------
181     # Start measurement loop
182     # ------------------------------------------------------
183     with open(csv_path, mode="w", newline="") as csvfile:
184         writer = csv.writer(csvfile)
185         writer.writerow(headers)
186
187         try:
188             keithley.connect()
189
190             # Configure instrument for four-wire resistance measurement
191             keithley.send_command(":SYST:BEEP:STAT OFF")
192             keithley.send_command(":SENS:FUNC 'FRES'")
193             keithley.send_command(":INIT:CONT OFF")
194
195             print(f"Press Ctrl+C to stop measurement. Data are saved to
                    {csv_path}")
196
197             MEASUREMENT_INTERVAL = 10  # s
198
199             while True:
200                 loop_start = time.time()
201
202                 row = []
```

```
203                 now = datetime.now(cet)
204                 elapsed_total = time.time() - start_time
205
206                 row.append(now.strftime("%Y-%m-%d %H:%M:%S"))
207                 row.append(f"{elapsed_total:.1f}")
208
209                 temp_dict = {}
210
211                 # ------------------------------------------------
212                 # Sequentially switch through selected channels,
213                 # read resistance, and convert it to temperature
214                 # ------------------------------------------------
215                 for ch in selected_channels:
216                     try:
217                         keithley.send_command(":ROUT:OPEN:ALL")
218                         keithley.send_command(f":ROUT:CLOS (@{ch})")
219
220                         response = keithley.query(":READ?")
221
222                         # Extract resistance value from scientific notation
223                         match =
                                re.search(r'([+-]?[0-9]*\.?[0-9]+[Ee][+-]?[0-9]+)',
                                response)
224
225                         if match:
226                             resistance = float(match.group(1))
227                             temperature =
                                    pt100.resistance_to_temperature(resistance)
228                             temp_dict[ch] = temperature
229
230                             sensor_label = channel_to_sensor.get(ch,
                                f"{ch}")
231                             print(
232                                 f"Sensor {sensor_label} (Ch {ch}): "
233                                 f"{resistance:.3f} Ohm | Temp:
                                        {temperature:.2f} °C"
234                             )
235                         else:
236                             temp_dict[ch] = "NA"
237
238                     except Exception:
239                         temp_dict[ch] = "NA"
240
241                 # ------------------------------------------------
242                 # Store current values in CSV file
243                 # All defined sensor positions are written in a
244                 # fixed order to ensure consistent data structure
245                 # ------------------------------------------------
```

```
246                 for ch, name in ordered_channel_sensor:
247                     if ch in temp_dict:
248                         val = temp_dict[ch]
249                         row.append(f"{val:.2f}" if isinstance(val, float)
                                else val)
250                     else:
251                         row.append("NA")
252
253                 writer.writerow(row)
254                 csvfile.flush()
255
256                 # ------------------------------------------------
257                 # Update live plot
258                 # ------------------------------------------------
259                 time_data.append(elapsed_total)
260
261                 for ch in selected_channels:
262                     val = temp_dict.get(ch, float("nan"))
263                     if isinstance(val, float):
264                         temp_data[ch].append(val)
265                     else:
266                         temp_data[ch].append(float("nan"))
267
268                     lines[ch].set_data(time_data, temp_data[ch])
269
270                 if len(time_data) > 0:
271                     ax.set_xlim(max(0, time_data[0]), max(10,
                            time_data[-1]))
272
273                     all_temps = [
274                         v for ch in selected_channels
275                         for v in temp_data[ch]
276                         if not math.isnan(v)
277                     ]
278
279                     if all_temps:
280                         min_temp = min(all_temps)
281                         max_temp = max(all_temps)
282
283                         if min_temp == max_temp:
284                             ax.set_ylim(min_temp - 1, max_temp + 1)
285                         else:
286                             ax.set_ylim(min_temp - 0.5, max_temp + 0.5)
287
288                     ax.relim()
289                     ax.autoscale_view()
290                     fig.canvas.draw_idle()
291                     fig.canvas.flush_events()
```

```
292
293                 # Keep approximately constant sampling interval
294                 elapsed_loop = time.time() - loop_start
295                 sleep_time = MEASUREMENT_INTERVAL - elapsed_loop
296                 if sleep_time > 0:
297                     time.sleep(sleep_time)
298
299         except KeyboardInterrupt:
300             print("\nMeasurement stopped by user.")
301
302         finally:
303             keithley.disconnect()
```

Erklärung zur selbstständigen Bearbeitung einer Abschlussarbeit

Gemäß der Allgemeinen Prüfungs- und Studienordnung ist zusammen mit der Abschlussarbeit eine schriftliche Erklärung abzugeben, in der der Studierende bestätigt, dass die Abschlussarbeit „– bei einer Gruppenarbeit die entsprechend gekennzeichneten Teile der Arbeit [(§ 18 Abs. 1 APSO-TI-BM bzw. § 21 Abs. 1 APSO-INGI)] – ohne fremde Hilfe selbständig verfasst und nur die angegebenen Quellen und Hilfsmittel benutzt wurden. Wörtlich oder dem Sinn nach aus anderen Werken entnommene Stellen sind unter Angabe der Quellen kenntlich zu machen."

Quelle: § 16 Abs. 5 APSO-TI-BM bzw. § 15 Abs. 6 APSO-INGI

Dieses Blatt, mit der folgenden Erklärung, ist nach Fertigstellung der Abschlussarbeit durch den Studierenden auszufüllen und jeweils mit Originalunterschrift als letztes Blatt in das Prüfungsexemplar der Abschlussarbeit einzubinden.
Eine unrichtig abgegebene Erklärung kann -auch nachträglich- zur Ungültigkeit des Studienabschlusses führen.

Erklärung zur selbstständigen Bearbeitung der Arbeit

Hiermit versichere ich,

Name: Ahlers

Vorname: Felix

dass ich die vorliegende Masterarbeit bzw. bei einer Gruppenarbeit die entsprechend gekennzeichneten Teile der Arbeit – mit dem Thema:

Investigation of Microchannel Cooling for Silicon Detectors for HEP and PS Applications

ohne fremde Hilfe selbständig verfasst und nur die angegebenen Quellen und Hilfsmittel benutzt habe. Wörtlich oder dem Sinn nach aus anderen Werken entnommene Stellen sind unter Angabe der Quellen kenntlich gemacht.

- die folgende Aussage ist bei Gruppenarbeiten auszufüllen und entfällt bei Einzelarbeiten -

Die Kennzeichnung der von mir erstellten und verantworteten Teile der -bitte auswählen- ist erfolgt durch:



Hamburg
Ort

Datum